Metal Nanocluster Arrays as Model System for Catalysts

Geordnete Metallnanopartikel als

Modellsystem für Katalysatoren

Der Naturwissenschaftlichen Fakultät

der Friedrich-Alexander-Universität Erlangen-Nürnberg

zur Erlangung des Doktorgrades Dr. rer. nat.

vorgelegt von

FABIAN DÜLL

aus Gunzenhausen

Als Dissertation genehmigt von der Naturwissenschaftlichen Fakultät der Friedrich-Alexander-Universität Erlangen-Nürnberg.

„Wir müssen oft neu anfangen, aber nur selten von vorne."

Ernst Ferstl

Kurzfassung

Heterogene Katalyse ist das Rückgrat der Chemieindustrie. Um diese Prozesse im Detail zu verstehen und bessere Katalysatoren sowie Methoden zur Verhinderung oder Reduzierung ihrer Deaktivierung zu entwickeln, ist die Erforschung hochkontrollierbarer Modellsysteme notwendig. Geordnete Übergangsmetallnanocluster auf gitterfehlangepassten zweidimensionalen Materialien sind solche Modellsysteme. Als katalytisch aktive Materialien für die Nanopartikel wurden Pd und Pt gewählt. Graphen und hexagonales Bornitrid (h-BN) bilden ein Moiré auf Rh(111) und damit ein Templat zur Anordnung der Cluster. Gleichzeitig sind diese 2D-Materialien chemisch inaktiv, d.h. alle beobachteten Reaktionen finden nur auf den Nanopartikeln und nicht auf dem Träger statt.

Um Katalysatorvergiftung besser zu verstehen, wurde der Einfluss von Schwefel auf Pd- und Pt-Nanopartikel untersucht, indem die Veränderung des Adsorptions- und Desorptionsverhaltens des Sondenmoleküls CO sowie die Wechselwirkung zwischen Schwefel und CO untersucht wurden. Da Oxidation ein möglicher Weg zur Schwefelentfernung und Katalysatorreaktivierung ist, wurde die Wechselwirkung zwischen Sauerstoff und Schwefel auf Pt-Nanoclustern gemessen und die Oxidations-kinetik bestimmt.

Legierungskatalysatoren haben oftmals überlegene Eigenschaften im Vergleich zu Einzelmetallen. Bimetallische PdPt-Legierungsnanocluster wurden präpariert und die Adsorption und Desorption von CO auf frischen und behandelten Clustern sowie die adsorbat- und temperaturinduzierte Clusterdynamik erforscht.

Um die Größenabhängigkeit des Wachstums von Pt-Nanoclustern und ihres Reifungsverhaltens bei erhöhter Temperatur zu bestimmen, wurde das h-BN/Rh(111)-Nanonetz mit Partikeln von einem bis fünfzig Atomen Größe keilartig gefüllt. Die Adsorption und Zersetzung von Ethen auf sauberen und kohlenstoffbedeckten Pt/h-BN-Nanoclustern wurde, auch als Modell für Verkokung, untersucht. Sie wurden des Weiteren als Templat zum Wachstum von Nanographen verwendet, wobei sich gleichzeitig van-der-Waals-Nanoheterostrukturen bilden.

Abstract

Heterogeneous catalysis is the backbone of the chemical industry. To understand these processes in detail and to develop better catalysts and methods to prevent or reduce deactivation processes, the investigation of highly controllable model systems is crucial. Transition metal nanocluster arrays supported on lattice-mismatched two-dimensional (2D) materials are such a model system. As catalytic active materials Pd and Pt were chosen for the nanoparticles. Graphene and hexagonal boron nitride (*h*-BN) form a Moiré structure on Rh(111), providing a template for the nanocluster arrays. At the same time, these 2D materials are chemically innocent, meaning that all observed reactions only happen on the nanoparticles and not on the support.

To better understand catalyst poisoning, the influence of sulfur on Pd and Pt nanoparticles was investigated by observing the changes of the adsorption and desorption behavior of the probe molecule CO as well as the interaction between sulfur and CO. As oxidation is a possible way to remove sulfur for reactivating catalysts, the interaction between oxygen and sulfur on Pt nanoclusters was measured and the kinetics of the oxidation was determined.

Alloy catalysts have, in many cases, superior properties compared to their single metal counterparts. Bimetallic PdPt alloy nanoclusters were prepared and the adsorption and desorption of CO on fresh and already treated clusters and the dynamics of the clusters caused by adsorbates and temperature investigated.

To access the size-dependence of catalytic particles, the *h*-BN/Rh(111) nanomesh was filled with Pt nanoclusters of one to fifty atoms size in a wedge-like manner. Their growth mechanism and their ripening behavior at elevated temperatures were determined in a size-dependent way. The adsorption and decomposition of ethylene was investigated on clean and carbon pre-covered Pt/*h*-BN nanoclusters, also as a model for coking. They were further used as template to grow nano-graphene and, thereby, to form van der Waals nano-heterostructures.

Content

1   Introduction

Catalysis is elementary to sustain today's society.[1] It stands behind almost every product, as it is involved in the production of the necessary materials and chemicals. Producing these accounts for about one-quarter of the industrial energy usage.[2] *E.g.*, one half of the nutrition of humanity is dependent on fertilizer that is based on the ammonia synthesis via the Haber-Bosch process.[3] Most technical processes in the production of bulk chemicals use heterogeneous catalysts, where the catalyst is in a different (solid) phase than the reaction mixture (gaseous or liquid educts and products); homogeneous and enzymatic catalysts play a minor role in this area and are more suitable for fine and special chemicals. The typical heterogeneous catalyst consists of polydisperse transition metal nanoparticles on an oxide support that has a porous structure to maximize the surface area available for chemical reactions. Its main advantage is that it is very convenient for continuous processes, as it is immobile. Homogeneous catalysts and enzymes afford a recycling step or stay in the product. A catalyst works by offering a new reaction pathway that has a lower activation barrier than the direct reaction. This enables the reaction to occur at milder, thus energy-saving, conditions and can also reduce byproducts by selectively enhancing the pathway to the desired product. The catalytic reaction consists of five steps: Diffusion of the reactants to the catalyst, binding of the reactants to the catalyst, the reaction on the catalyst, the desorption of the products from the catalyst, and the diffusion of the products away from the catalyst. Thereby, the catalyst is not consumed and regains its original structure at the end of a catalytic cycle, ready for the next one. The quality of a catalyst is defined by its activity, selectivity, and stability. All of these three properties are connected to catalyst deactivation, as it reduces the activity and selectivity, while the stability defines the robustness against deactivation.

Heterogeneous catalysts suffer from four kinds of deactivation processes caused by external influence: poisoning, deposition, sintering, and loss of active material by volatilization and abrasion.[4–6] They are schematically shown in Figure 1.1. Poisoning is caused by adsorbates and works via one or more of three mechanisms: physical blocking of the active surface area, changes in the electronic or geometric surface structure, or hindering of the diffusion of other adsorbates. For poisoning, already small amounts of the poison can have a high impact, but these can also be positive. Well-controlled poisoning, called (chemical) tempering, is used to enhance the selectivity of processes, *e.g.*, the reforming of naphtha. New Pt-Re/Al$_2$O$_3$ reforming catalysts are pretreated with low concentrations of a sulfur compound. This poisons some very active sites and, thus, limits the high

hydrocracking activity.[7] As an additional example, sulfur enhances the selectivity of the conversion of butadiene to butenes on Pd/SiO₂.[8] However, in many cases, sulfur is an unwelcome, yet abundant component in different feedstocks, mostly in form of SO_2 and H_2S. As Pd and Pt are widely used catalyst materials,[5,6,9,10] their deactivation by sulfur is a hot topic.[11–13] Examples are reforming of naphtha or the three-way catalyst of cars. Revealing the mechanism of sulfur poisoning of these two metals is part of this thesis, as is the coking of Pt. The difference between poisoning and deposition, which in the most common case of carbon deposits is called coking, is that in the latter case the access of the educts to the catalyst is simply physically blocked by large amounts of material, while poisoning changes the properties of the catalyst. Processes like fluid catalytic cracking suffer from such high coking rates that a continuous regeneration of the catalyst in a fluidized bed reactor is necessary. The burning of the coke is integrated into the process in such a way that it provides the heat for the cracking.[14]
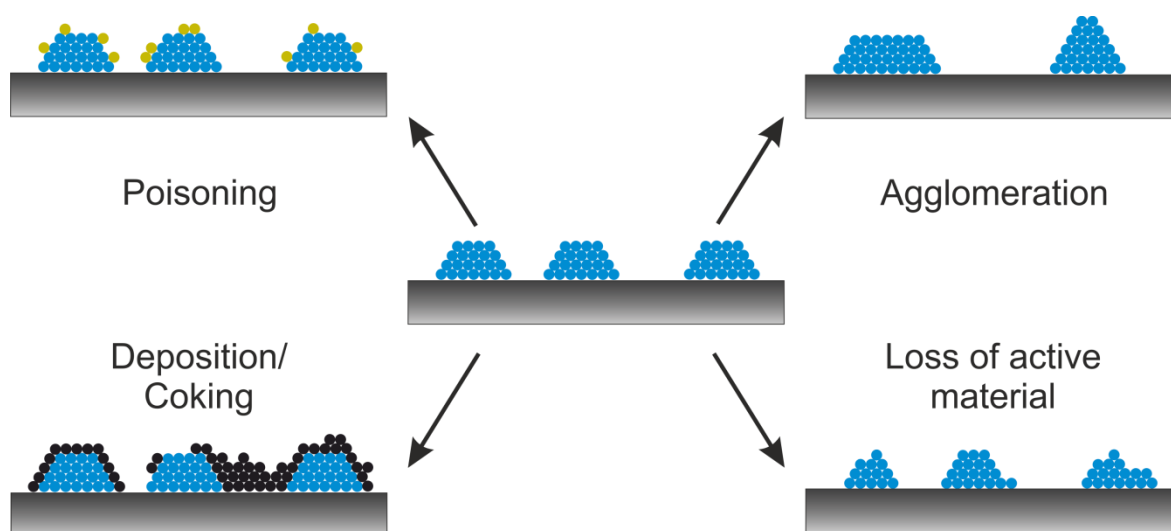

Figure 1.1: Deactivation mechanisms of heterogeneous catalysts.

Another type of catalyst deactivation is agglomeration. In general, it follows one of two mechanisms: Ostwald[15] and Smoluchowski[16] ripening. In the first case, particles exchange single atoms, while staying at the same spot. Due to their lower vapor pressure, bigger particles will grow at the expense of smaller ones. Thereby, the number of particles will decrease, while their average size will increase. In the Smoluchowski mechanism, whole particles diffuse and merge with each other. In both cases, this leads to a loss of surface area of the active material according to the cubic square law. Furthermore, there is the solid state transformation mechanism that changes the internal structure of a catalyst, called sintering. Thereby, over time, the material transforms into a

thermodynamically more favorable structure that is less active for catalysis. A related phenomenon is investigated in this thesis, that is, the dynamics and structural change of a PdPt alloy system. Knowledge about such changes and the dynamics are also crucial if one wants to fine-tune existing or to tailor completely new catalysts. Therefore, the active sites have to be identified as well as all factors that influence their reactivity. The ultimate goal is to be able to design the ideal catalyst for a desired product or process *ab initio*. It should catalyze the reaction with high selectivity under mild conditions using the most basic feed stocks. By now, most catalyst design approaches in engineering are more or less based on try and error, in better cases on educated guessing.

To be able to design a catalyst in a rational approach, in-depth knowledge of the interface between the catalyst and the reaction mixture, *i.e.*, the catalyst surface, and the processes there is crucial. Surface science provides a wide range of tools to obtain this understanding. Yet, it is not possible to apply most spectroscopic and microscopic methods to commercial catalysts *in operando*, as they require ultra-high vacuum (UHV) conditions. On the one hand, the operation conditions, often high pressures and temperatures, are hostile to the instruments and methods. On the other hand, the complexity of the systems and the number of parallel and connected processes makes an understanding of a single process challenging. Therefore, it is necessary to use simplified model systems under accessible conditions. The two differences to applied catalysts are referred as the pressure gap and the materials gap. To bridge the pressure gap, one can modify existing measurement methods to make them more robust, *e.g.*, atomic force microscopy (AFM) in liquids[17] or near-ambient pressure X-ray photoelectron spectroscopy (NAP-XPS).[18]

For closing the materials gap, choosing the right model systems is the key. Metal nanoclusters supported on chemically innocent two-dimensional materials are utilized to achieve this in the present thesis. This approach bases on a step-wise increase of the complexity of the models system, while in each step the knowledge gained on the simpler system is transferred to the more complex one, see Figure 1.2.
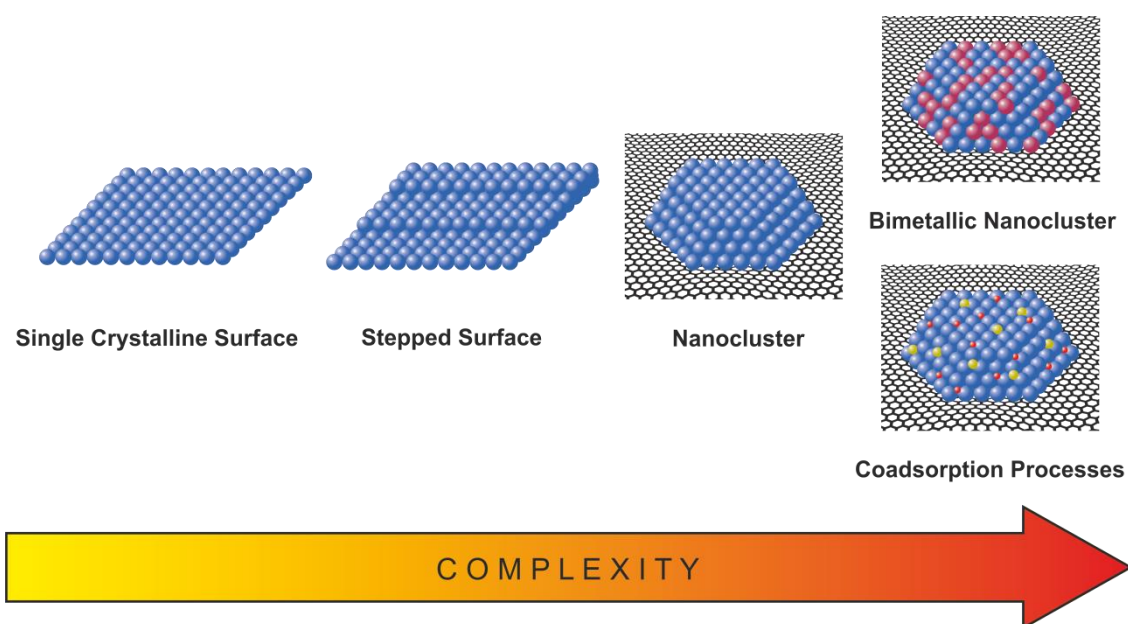
Figure 1.2: Bridging the materials gap by stepwise increasing the complexity of model systems.

The starting point are single crystalline metal surfaces with low Miller indices, typically (111) and (100) surfaces. While these are the simplest model systems one can get, they are still suitable as a model system for real catalysts, as facets of those orientations are the dominating structures of nanoparticles. Thus, they provide fundamental knowledge of the surface processes as the basis everything more complex is built on. The introduction of steps on the surface allows for studying these important binding sites. In a system, where they exist, step sites often dominate the reaction properties.[19] The next level is to model the nanoparticles that are the reactive sites of a catalyst. Therefore, one actually uses nanoparticles but in a defined way. The nanoparticles in a catalyst generally are polydisperse with a heterogeneous size-distribution and a complex interaction with the oxide support that itself is often directly involved in the reaction. Thus, it is convenient to use nanoclusters of a controllable size with a narrow size-distribution on a simple support that does little more than carrying the nanoparticles.

Suitable support materials are two-dimensional materials like graphene and hexagonal boron nitride (h-BN). They have the advantage that they are chemically innocent towards reactions that happen on the nanoclusters, as only highly reactive adsorbates like radicals will bind to them. This suppresses spillover and reverse-spillover effects, where adsorbates diffuse between the particle and the support. Thus, the investigated processes and reactions will only happen on the nanoclusters. If the 2D-material is grown on a lattice mismatched single crystal like Ir(111) or Rh(111) one gets the

additional advantage of a template effect. A Moiré structure forms that traps the nanoparticles in the valleys and separates them from each other by the hills. The size-distribution during the growth is narrowed and agglomeration effects are suppressed.[20,21] They were used with success to investigate adsorption and desorption processes[22–25] as well as simple reaction kinetics.[23] In this work, we will go one step further and utilize Pd and Pt nanoclusters supported on the Moiré structures of graphene and h-BN on Rh(111) to investigate adsorbate-adsorbate interactions as they occur in catalyst poisoning and coking. We will have a look at size-dependent effects and go to more complex bimetallic nanoparticle systems. Another application is to use the nanoclusters together with graphene and h-BN as part of heterostacks. These are layered nanomaterials held together by van der Waals forces.[26] In this case, the nanocluster arrays are not only a model system but a building block for various, mostly electronic devices.[27] Such can be photodetectors, data storage materials, or field-effect transistors. Graphene-covered nanoparticles could also have interesting catalytic properties, because a graphene-cover can enhance reactions of molecules trapped between it and the metal-surface.[28] Additionally, this opens a new route to synthesize nanographene.

In this thesis, Pd and Pt nanoclusters on graphene and h-BN on a Rh(111) single crystal were investigated by synchrotron-based high-resolution X-ray photoelectron spectroscopy (HR-XPS) and near-edge X-ray absorption fine structure (NEXAFS) measurements. Chapters 2.1 – 2.3 will introduce into the generation of synchrotron light and the used techniques. The experimental setup will be presented in Chapter 2.4, followed by the data acquisition in Chapter 2.5. Chapter 2.6 will explain the synthesis of borazine, which is the precursor for the growth of h-BN. In Chapter 2.7, the advantages and properties of graphene and h-BN as templates for metal nanocluster arrays will be discussed. Chapter 3 will give insight into the poisoning of Pd (Chapter 3.1) and Pt (Chapter 3.2) nanoparticles by sulfur and how the adsorption of the probe molecule CO is influenced by it. This will be supplemented by investigations of the reactivation by sulfur oxidation on Pt nanoclusters in Chapter 3.3. The bimetallic PdPt alloy particle system and its dynamics will be presented in Chapter 4. Pt nanocluster arrays supported on h-BN/Rh(111) will be the content of Chapter 5. It consists of basic investigations of the size-dependent grow and temperature stability of these nanoparticles (Chapter 5.1), the adsorption and reaction of ethylene as model system for coking (Chapter 5.2), and their use as a building block for nano-heterostructures/template for growing nanographene (Chapter 5.3). Finally, Chapter 6 will summarize the main results of this thesis.

2 Fundamentals

This chapter will introduce into the experimental techniques used by the author for this thesis, as well as their theoretical background and their implementation in the experimental setup. As all measurements were done at a synchrotron facility, Chapter 2.1 will introduce the basics of synchrotrons and the generation of X-ray radiation by them. The X-ray radiation was applied for two experimental techniques: X-ray photoelectron spectroscopy (XPS) was the primary method used in this work, and the underlying photoemission process and its use as spectroscopic method will be described in Chapter 2.2. Near-edge X-ray absorption fine structure (NEXAFS) measurements were used to supplement the XPS data. Thus, Chapter 2.3 will briefly introduce this technique. The experimental setup, the "Sync"-machine, will be presented in Chapter 2.4 together with the basic sample preparation. As borazine is the necessary precursor for the growth of h-BN, Chapter 2.5 will give details about its synthesis. Chapter 2.6 will introduce the Moiré structure of graphene and h-BN on Rh(111) and how they are utilized as templates for metal nanocluster arrays.

2.1 Synchrotron Radiation

As the spectroscopic methods used in this work require high-flux monochromatic X-rays that are not available with lab sources, all measurements were conducted at the synchrotron facility BESSY II (Berliner Elektronenspeicherring für Synchrotronstrahlung) of the Helmholtz-Zentrum Berlin. This chapter introduces in the generation of synchrotron radiation using the example of BESSY II (Figure 2.1).

Synchrotron radiation is a special kind of Bremsstrahlung and was predicted by Iwanenko and Pomerantschuk in 1944.[29] It is emitted when an electric charge is accelerated perpendicular to its flight path. This process constantly happens in nature when fast, charged particles interact with stellar magnetic fields in space. The same effect dedicated for the generation of X-rays is used in a synchrotron. Here, relativistic electrons are used as the charged particles. At BESSY II, they have an energy of 1.7 GeV. To access this energy, the electrons, produced by thermal emission in an electron gun, are first accelerated in a microtron and reach their final energy in the booster ring. They are then injected into the storage ring, which is the actual synchrotron. BESSY II has a circumference of 240 m with 32 bending magnets that keep the electrons in a closed polygonal

path. Thereby, the electrons are traveling through the storage ring in bunches and have a lifetime of several hours. To compensate the losses, new electrons are injected during operation. The already mentioned bending magnets have a second use as simple light sources. For higher fluxes, designated insertion devices like wigglers and undulators are used. A wiggler is an array of dipole magnets that forces the electrons on a sinusoidal flight path; they "wiggle". Like bending magnets, wigglers produce a broad energy spectrum.
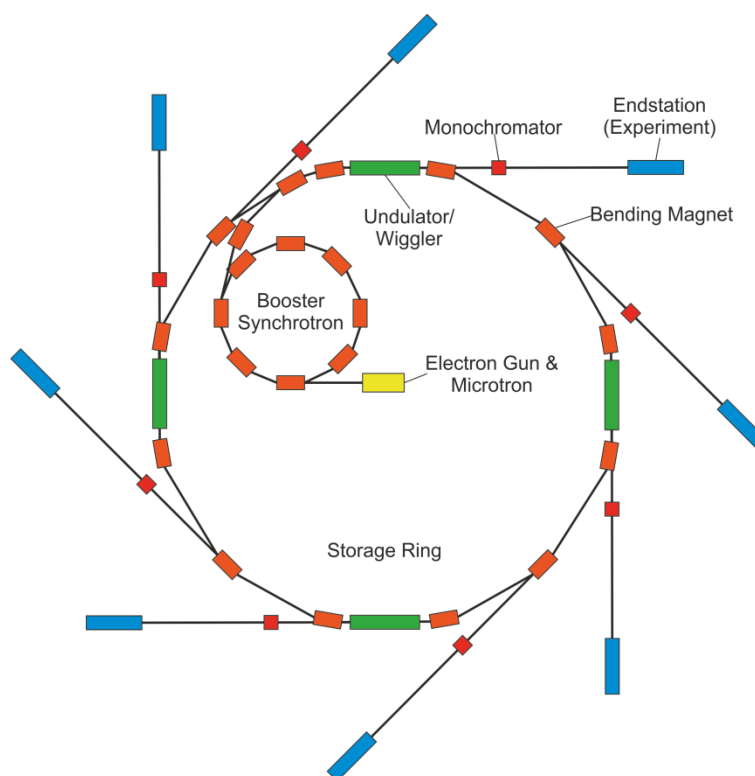

Figure 2.1: Scheme of a synchrotron facility with eight beamlines.

Undulators are similar to wigglers, but the gap between the dipole magnets is smaller. Thus, the emitted radiation lobes of the single dipole pairs interfere, leading to a sharper spectrum, higher intensity, and higher brilliance. The emitted spectrum consists of a few peaks of few electron volts width that are the harmonics of a single fundamental. The fine-tuning of the photon energy for all insertion devices is done by filtering with a monochromator. Another property of the so produced light is its polarization. The standard polarization is linear horizontal in the plane of the synchrotron (Figure 2.2). By altering the array of the undulator magnets and therefore the orientation and shape of the magnetic field, it is possible to alter the angle of linear polarization plane and to produce circular and elliptical polarized light. A range of experimental techniques use

synchrotron light. From those, two were applied in this thesis. They will be presented in the following two chapters.
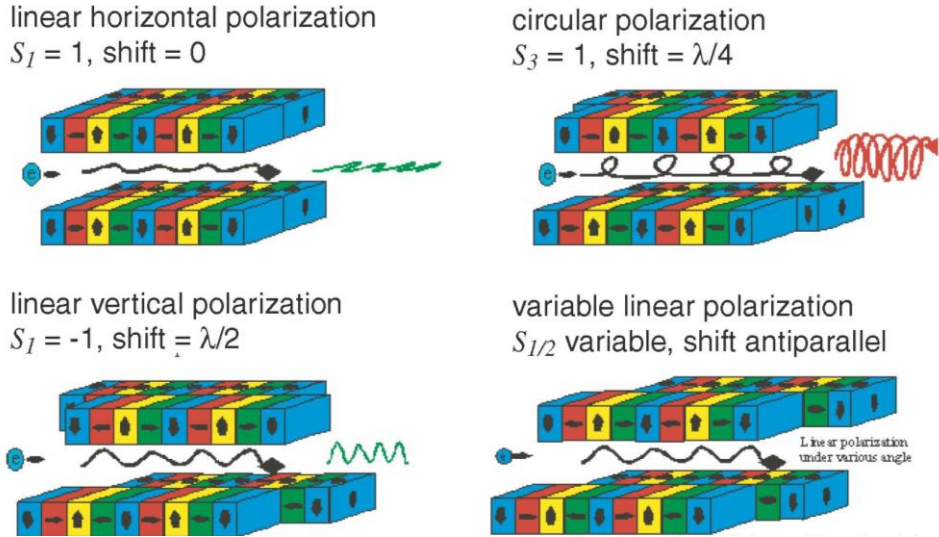

Figure 2.2: Scheme of an APPLE-2 undulator emitting synchrotron radiation with different polarizations.[30]

2.2 Photoelectron Spectroscopy

X-ray photoelectron spectroscopy (XPS), also called Electron Spectroscopy for Chemical Analysis (ESCA), is a method for studying the chemical composition of surfaces using the photoelectric effect, which was discovered in 1887 by Hertz and Hallwachs.[31] It is the main spectroscopic method used in this thesis. A scheme of the process is shown in Figure 2.3. The explanation was given in 1905 by Einstein[32] and the maximal kinetic energy $E_{Kin,max}$ of the photoelectrons is given by:

$$E_{Kin,max} = h\nu - \Phi,$$

where h is the Planck constant and Φ the work function, *i.e.,* the minimal energy to bring an electron from the Fermi level into the vacuum. For insulators and semi-conductors, the Fermi level is located in the center of the energy gap between the valence and the conduction band of a material. In metals, it is located at the border between the occupied and unoccupied states of the conduction band. When doing XPS, also the electron's binding energy E_B has to be considered:

$$E_{Kin} = h\nu - E_B - \Phi$$

Φ is a constant of the sample, but often hard to measure. As the spectrometer also has a work function, it is convenient for conducting samples to electrically connect electron analyzer and sample, so their Fermi levels align. E_{kin} (and E_B) is then referenced to the Fermi level E_{Fermi} and the above formula changes to:

$$E_{kin,F} = h\nu - E_B.$$

The binding energy of the electrons depends on the element and the specific orbital it is released from; it is, therefore, element specific. Additionally, the oxidation state and the chemical environment of the atom result in a change of the orbital's energy and, thus, generate a chemical shift of the binding energy. The chemical shift is a superposition of initial and final state effects. An initial state effect is caused by the situation before the photoemission process and caused by a change of the charge density of a probed atom, *e.g.*, its oxidation state. Less electron density means a stronger bonding of the (remaining) electrons, as the positive charge of the nucleus is less shielded. Final state effects occur during the photoemission process: These can be energy losses to other electrons in higher shells that are either promoted into excited states (shake up) or into the vacuum (shake off). Also, shielding of the core hole can affect the binding energy. An effective screening of the core holes by negative charges leads to a higher kinetic energy of the photoelectron due to less coulomb interaction between the core hole and the emitted photoelectron. *E.g.*, the binding energy difference between molecules in the gas phase and on metal substrates is an effect of the shielding of the core-holes by electrons of the substrate, resulting in higher kinetic energies, therefore, lower binding energies of the photoelectrons.
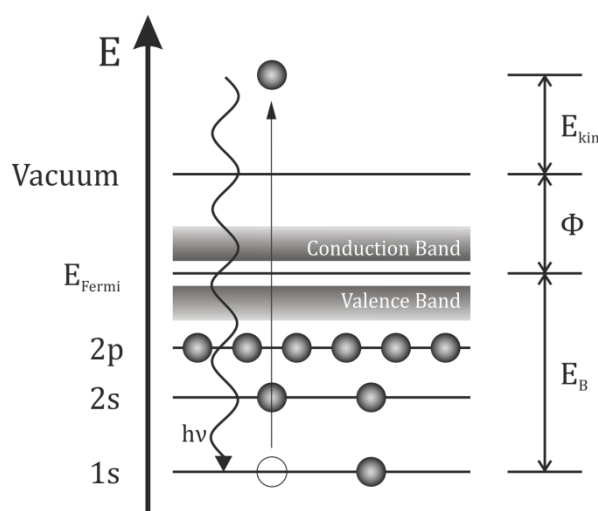

Figure 2.3: Scheme of the photoemission process.

As the probability for photoemission is independent of the chemical surrounding, qualitative and quantitative information of the surface and adsorbate layers are obtained. While, in theory, it is possible to quantify the XP-signal from basic principles using Fermi's golden rule, actually formulated by Paul Dirac,[33]

$$\Gamma_{i \to f} = \frac{2\pi}{\hbar} |\langle f|H'|i\rangle|^2 \rho(E_f),$$

it is more convenient to use the signal of a known, ordered structure as a reference. Typically, this is a closed layer of a simple adsorbate like CO or a 2D material like graphene or h-BN, whose quality and coverage was cross-checked with a second method, normally low energy electron diffraction (LEED). However, this has to be done carefully, as photoelectron diffraction can influence the intensity of the signal.[34]

Measuring XPS at a synchrotron comes with several advantages: The most obvious is the high flux of photons. This enables fast measurements with an excellent signal to noise ratio but also a higher resolution. The latter comes from the high brilliance, as it allows for a better monochromatization and a small spot size without going to unacceptable low fluxes. The small spot size on the sample makes scanning of non-homogeneous samples possible. The tuneability of the photon energy gives a high surface sensitivity due to the comparably low mean free path of the electrons, which is around 3 Å at a kinetic energy of 100 eV.[35] This makes adjusting the excitation energy for each chemical element necessary. Additionally, it opens the possibility to do a series of measurement at different excitation energies and to produce depth profiles of a sample.

2.3   Near-Edge X-ray Absorption Fine Structure

Another application of the tuneability of synchrotron light is the measurement of near-edge X-ray absorption fine structures (NEXAFS). While in XPS the energy of the photoelectrons is scanned at a fixed photon energy, in X-ray absorption spectroscopy (XAS), the photon energy is scanned. Like in all kinds of absorption spectroscopy, it is the aim to excite transitions of the sample material. In the case of XAS, these are excitations of core electrons to the unoccupied electronic states (Figure 2.4). The near-edge in NEXAFS means that the scanning range is limited to ~20 eV above an absorption edge of the sample. Since NEXAFS probes the unoccupied states of a sample, its information is complementary to XPS that probes the occupied states. NEXAFS proves especially

valuable for molecular systems, as here the transition into π*-orbitals results in sharp peaks. This is because the π*-orbitals have a narrow energy distribution and are typically below the ionization threshold. NEXAFS also detects transmissions into the σ*-orbitals, though they are less defined and result in broad signals, as they are above the ionization threshold in the quasi-continuum. Only the centrifugal barrier separates these states from the vacuum. Similar to XPS, NEXAFS peaks show a chemical shift. Thus, NEXAFS is sensitive to the chemical surrounding of the probed transition. Furthermore, NEXAFS is sensitive to the orientation of orbitals/the transition dipole moment with respect to the incoming light, if it is polarized. Only transitions into orbitals, whose dipole moments are orientated parallel to the light's direction of polarization, are excited. By measuring at two or more incidence angles, the orientation of the orbitals and, therefore, of the adsorbed molecules can be received. In this work, measurements normal to the surface and at 70° with respect to the surface normal were conducted.
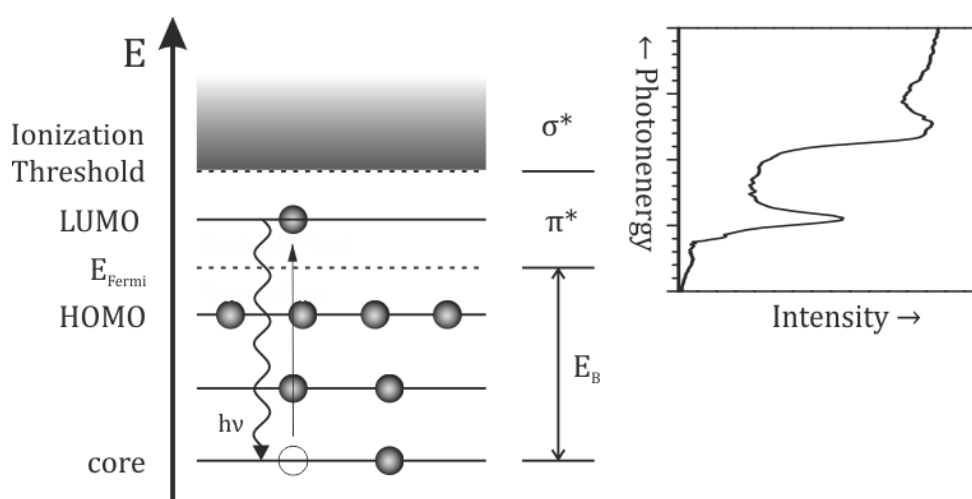

Figure 2.4: Scheme of the light absorption and excitation of electrons from the core levels to the unoccupied states as occurring during NEXAFS measurements. Attached is an exemplary NEXFAS-spectrum of graphene on Pt nanoclusters.

To record XA-spectra, several methods are available: Photon transmission, fluorescence yield (where secondary photons are measured), and total, partial, and Auger electron yield (where the photoelectrons are detected). The latter three differ in the energy window of the detected electrons. In total yield, all electrons are measured. For partial yield, electrons below a specific kinetic energy are filtered out, while for Auger yield only electrons of a particular energy range may pass to the detector. In this work, a home build detector was used in partial yield mode. The partial yield mode has the advantage that it is more surface sensitive than total yield while giving a better signal intensity than Auger yield.

2.4 Experimental Setup

All experiments presented in this thesis were conducted in the "Sync"-apparatus. This is a mobile machine that consists of two main chambers, a supersonic molecular beam, and a separately pumped dosing system, build by Pink GmbH Vakuumtechnik. A scheme is provided in Figure 2.5. For measurements, it is connected to one of several open port undulator beamlines at BESSY II, the synchrotron facility located in the Berlin-Adlershof campus of the Helmholtz-Zentrum Berlin für Materialien und Energie.

The preparation chamber is equipped with an ion sputter gun (Specs, IQE 11/35) for sample cleaning, LEED optics (Specs, Er-LEED), two single and one triple electron beam evaporator (Fokus) for the evaporation of metals (Pd and Pt), and a quartz crystal micro balance (QCM, Sycon Instruments STM-100/MF) for measuring their deposition rate. It is connected to the dosing system. A gate valve connects the preparation chamber with the analysis chamber. A hemispherical photoelectron energy analyzer (Omicron, EA 125 U7 HR) with seven channeltrons (Burle), a single channeltron NEXAFS analyzer (home-build), and a quadrupole mass spectrometer (QMS, Pfeifer, Prisma QME 200) are attached to it. The analysis chamber is also connected to the dosing system via a multi-capillary array doser, it has an inlet for the supersonic molecular beam, and it is attached to the beamline. The dosing system possesses four leak valves and was used for exposing the sample to borazine and SO_2. The three-stage supersonic molecular beam has a nozzle of 100 µm diameter. CO, O_2, and ethylene were dosed via two mass flow controllers.

At BESSY II, the machine was attached to the open port undulator beamlines U49/2-PGM2 ([P1]), UE56/2-PGM-2 ([P2] – [P6]), and UE56/2-PGM-1 ([P7]). U49/2 is a planar hybrid type undulator with 84 periods that produces linear horizontally polarized light. UE56/2 is an APPLE2 type undulator with 30 periods that can produce linear horizontally, linear vertically, elliptically, and circularly polarized light. The measurements were conducted, while BESSY II was operated in multi-bunch top-up mode with 250 mA ring current, *i.e.*, new electrons are injected every few minutes to keep the ring current almost constant.
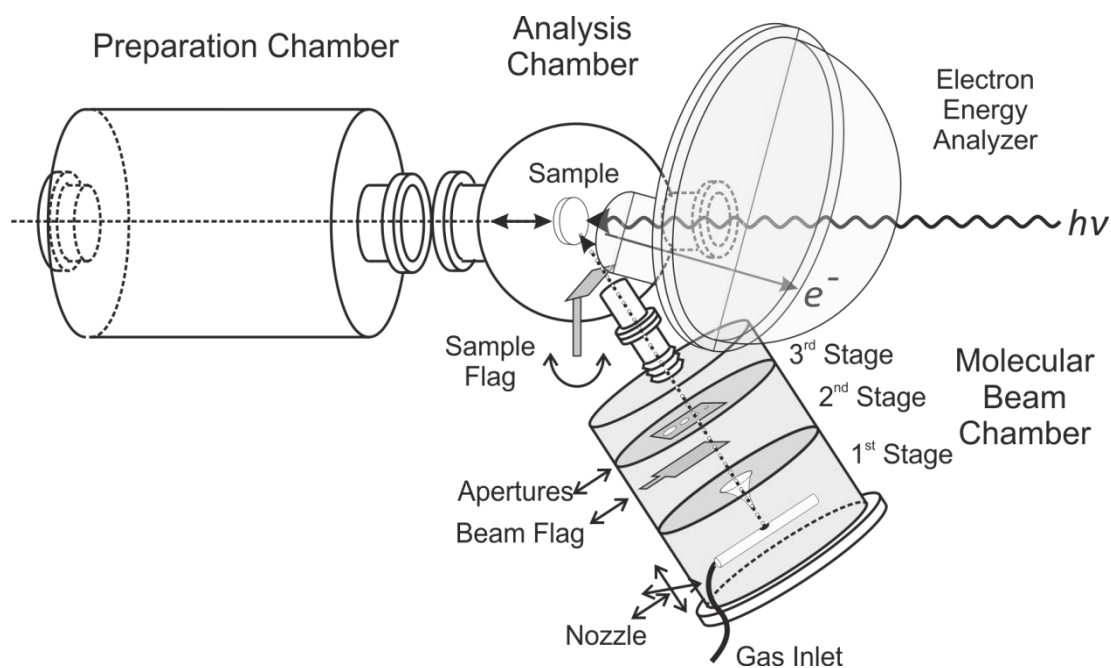
Figure 2.5: Scheme of the "Sync"-apparatus. Adapted after.[36]

The sample was a cylindrical Rh(111) single crystal (MaTeck) with a diameter of 10 mm, a thickness of 3 mm, and an orientation accuracy of 0.1°. It is mounted on a xyzφθ-manipulator with rotary feedthrough via two tantalum wires, spot-welded on the sides of the crystal. The manipulator head also allows for tilting of the sample by 90° and transferring it between the two chambers by an 800 mm travel. Two independent K-type thermocouples are spot-welded to the sides of the crystal to measure the temperature. The temperature is adjustable between 100 and 1400 K by resistive heating and liquid nitrogen cooling. A tungsten filament at the backside of the sample allows heating of the sample while minimizing the magnetic field that would disturb the flight path of the photoelectrons and thus reduce the signal intensity. Filament heating is used for temperature-programmed experiments (TPXPS), where XP-spectra are measured, while a heating ramp of typically 0.2 – 0.5 K/s is driven up to 550 K.

The Rh(111) sample was cleaned by Ar^+-sputtering and oxidizing at 900 K, each followed by heating to 1200 K to remove excess Ar and oxygen and to reconstruct the surface after the sputtering process. The cleanliness of the crystal was checked by XPS at several spots.

2.5 Data Acquisition and Evaluation

The XP-spectra were recorded in normal emission with a beam incident angle of 50°. The X-ray spot on the sample was rectangular shaped with a vertical dimension of 30 - 80 μm (depending on the used exit slit width) and a horizontal dimension of <140 – 1400 μm (depending on the beamline). To prevent beam damage, the position of the X-ray spot was shifted between each spectrum for radiation-sensitive samples.

For evaluation, the binding energy of the XP-spectra were referenced to the Fermi level. A linear background was subtracted, and the XP-spectra were fitted with a set of asymmetric Doniach-Šunjić functions convoluted with Gaussian functions.[37] The Gaussian function accounts for the linewidth due to the experimental setup that is the analyzer resolution and the monochromaticity of the X-rays. The Doniach-Šunjić function is an asymmetric extension of a Lorentzian profile. Its width accounts for the natural linewidth of a signal caused by the lifetime of the excited state according to Heisenberg's uncertainty principle.[38] The asymmetry of the peaks is necessary to take the special shape of XP-spectra into account. The emitted photoelectrons can further interact with matter, which leads to elastic energy losses. These lead to an increased background intensity on the high binding energy side of XP-spectra. Special backgrounds were invented to handle this issue, like Shirley[39] or Tougaard.[40] However, additional effects like the creation of electron-hole pairs at the Fermi level can influence the symmetry of an XP signal. They are not taken into account by mentioned background subtraction methods but can be handled with asymmetric fit functions. The mentioned data evaluation process was done using a custom procedure in IGOR Pro 6.22A (WaveMetrics).

To quantify the XP-spectra, different calibration methods were used depending on the kind of species: 2D material like h-BN provide an internal calibration of the signal for a closed layer, as their structure is known and their quality can be cross-checked with other spectroscopic or microscopic methods like LEED or scanning tunneling microscopy (STM). Forming a 13x13 on 12x12 superstructure on Rh(111), a closed h-BN layer consists of 169/144 ≈ 1.17 ML of each, boron and nitrogen. The amounts of evaporated metals (Pd and Pt) were calibrated by using a QCM to monitor the deposition rate of the electron beam evaporators at the sample position. The deposited film thicknesses were converted into coverages. Coverages of adsorbates were calibrated using reference structures checked by LEED. For C and O coverages, the (2x2) structure of CO on

Rh(111) with 0.75 ML was used as reference (1 ML is defined as 1 CO molecule per surface atom).[41] Sulfur coverages on the nanoclusters were referenced by a c(2x2) overlayer of S with a coverage of θ_S = 0.5 ML on a Pd(100) single crystal[42] and a (2x2) overlayer of S with a coverage of θ_S = 0.25 ML on a Pt(111) single crystal, respectively.[43] To gain relative sulfur coverages $\theta_{S, rel}$, the surface of the particles was determined by comparing the integrals of the CO-saturated nanoparticles and 0.75 ML CO on Rh(111).

NEXAFS was recorded in partial yield at angles of 0° and 70° of the X-ray beam with respect to the surface normal. The retention voltage was -180 V for the C K-edge. The spectra were normalized with respect to the ring current of the synchrotron and divided by reference spectra of the clean Rh(111) single crystal to cancel out the spectral shape of the used X-rays. The evaluation of the NEXAFS data, as well as further evaluation of the fitted XPS data, was done with Origin 9.0G (OriginLab).

2.6 Borazine Synthesis

The growth of *h*-BN layers by chemical vapor deposition requires a compound that contains boron and nitrogen atoms in a 1:1 stoichiometric ratio and is easy to evaporate and decompose. While, at least in theory, for the growth of graphene, all kinds of hydrocarbons are available as precursor, the range of choices is very limited for BN compounds. In the beginning, amino borane (BH_3NH_3) was used in this group. However, this white solid requires a heatable evaporator and passivates over time in UHV. Thus, it was replaced by the better-to-handle liquid borazine ($B_3N_3H_6$) that can be dosed via a leak valve. As borazine is not easily commercially available, it was synthesized by the author, according to the method of Sneddon:[44] Ammonium sulfate ((NH_4)$_2SO_4$; 82.3 g; 0.62 mol) and Sodium borohydride ($NaBH_4$; 30.7 g; 0.81 mol) were mixed with tetraglyme (250 ml) in a three-neck round-bottomed flask fitted with a thermometer and reflux condenser. The tetraglyme was dried with sodium beforehand. The exit was connected to a vacuum line via three cooling traps with temperatures of -45, -78, and -196 °C. The reaction mixture was gradually warmed to 135 °C over the course of 1 h and held at this temperature under a dynamic vacuum of a rotary vane pump by the continuous removal of the evolved hydrogen and borazine through the vacuum line until hydrogen evolution stopped. The borazine was caught in the -78 °C trap (12.6 g; 0.156 mol; 57.9% based on the starting BH_4^-).

$$3\,(NH_4)_2SO_4 \quad + \quad 6\,NaBH_4 \quad \xrightarrow[\text{Tetragylme}]{120\text{-}140\,°C,\ 3\,h} \quad 2 \quad \text{[Borazine]} \quad + \quad 2\,Na_2SO_4 \quad + \quad 18\,H_2$$
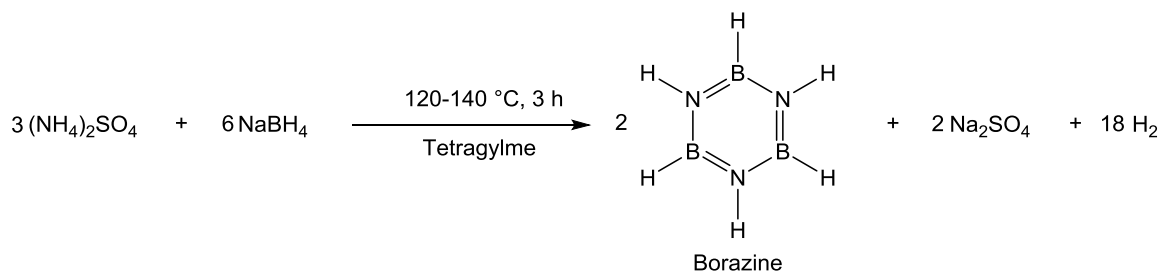
Borazine

Figure 2.6: Synthesis of borazine according to the method of Sneddon.[44]

2.7 Lattice Mismatched 2D Materials as Templates for Nanocluster Arrays

Graphene and *h*-BN are highly-ordered two-dimensional materials with a hexagonal structure and a thickness of one atom. The graphene unit cell contains two carbon atoms, while the *h*-BN unit cell contains one boron and one nitrogen atom. All atoms are sp^2-hybridized. The original interest of putting these material on metal surfaces was as protective coating, *e.g.*, against oxidation, as graphene and *h*-BN proof as rather inert against chemical reactions.[45] Functionalization requires highly reactive reactants like radicals[46,47] or tricks like electronic activation combined with reactive electrophiles.[48] Over time, the interest has shifted towards the 2D material themselves and their interaction with the metal substrate, especially as they can be easily prepared via self-assembly on any metal surface with threefold or sixfold symmetry. There are two groups of metal-2D overlayer interactions: Weak hybridization between the transition metal d-states and the graphene/*h*-BN π-states, which can be understood as physisorption, and strong hybridization that is chemisorption.[49] However, there is no sharp border between the two interactions. Transition metal surfaces with weak hybridization are, *e.g.*, Cu(111),[50] Ir(111),[51] and Pt(111), while strong hybridization is found, *e.g.*, with Ni(111), Rh(111), and Ru(001).[52] Thereby, Ni(111) is special as it is lattice-matched with graphene and *h*-BN. Thus, they form perfectly flat layers on Ni(111) with two C atoms or one B and one N atom interacting with one Ni atom. The other mentioned metal surfaces are lattice-mismatched. This forces graphene and *h*-BN into Moiré superstructures that can be understood as hexagonal ordered hill and valley structures. Thereby, the hills are weakly and the valleys strongly interacting with the metal. The lattice constant of the Moiré, as well as the height and steepness of the hills, strongly depend on the metal and also differ between graphene

and *h*-BN. Graphene forms a (10x10)/(9x9) superstructure on Ir(111),[51] a (12x12)/(11x11) superstructure on Rh(111) and Ru(111),[53] while on Pt(111) several graphene phases exist with different periodicities and orientations.[52]

The XP-spectrum of a well-ordered graphene layer on Rh(111) is shown in Figure 2.7a. The strongly interacting C atoms that are close to the Rh substrate – the "valleys" of the Moiré – are depicted in ochre, and the weakly interacting C atoms that are further away from the metal surface - the "hills" - are depicted in green. To grow high-quality graphene on Rh(111) via chemical vapor deposition, it is important to choose the right conditions. A temperature of 920 K and an ethylene pressure that should not be too high, ideally ~ 2 x 10^{-8} mbar, are used.[54] Lower temperatures lead to more defects and more carbide, while higher temperatures suppress the growth of graphene without going to higher pressures. Exceeding the mentioned ethylene pressure will result in too many nucleation points for the growth and thus a high number of domains and domain boundaries.
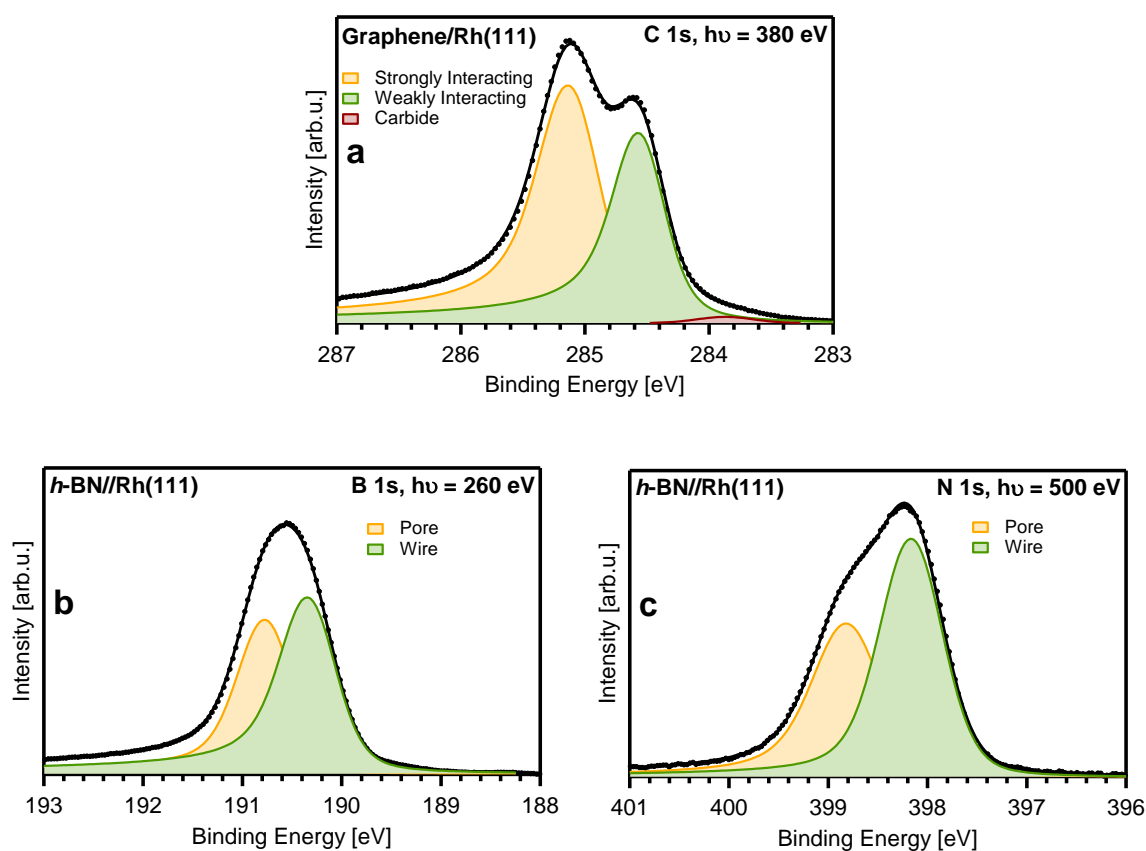
**Figure 2.7:** XP-spectra of lattice-mismatched 2D materials on Rh(111): a) C 1s spectrum of graphene∕Rh(111); b) B 1s spectrum of *h*-BN∕Rh(111); c) N 1s spectrum of *h*-BN∕Rh(111). All spectra were measured at 150 K to reduce thermal broadening.

h-BN usually interacts stronger with the substrate as graphene, especially for Ir(111),[55,56] resulting in steeper transitions between the stronger and weaker interacting parts of the Moiré.[49] These are referred as pores and wires of a nanomesh.[57] On Rh(111), *h*-BN is grown via chemical vapor deposition of ~ 2 x 10^{-8} mbar borazine at 1050 K.[57] Figure 2.8a shows an STM picture of a freshly grown *h*-BN/Rh(111). The hexagonal structure of the wires and the round pores are clearly visible. Similar to graphene, the pores and wires of the *h*-BN nanomesh result in two peaks in XPS, shown in Figure 2.7b for the B 1s and Figure 2.7c for the N 1s. The ratios of the integrals of the signals of the pores (ochre) and wires (green) are similar in both core-levels, but the pore peak is comparatively broader in the N 1s due to a stronger interaction between B and Rh than N and Rh in the pores.[49] The Moiré superstructures of *h*-BN usually have slightly bigger lattice constants compared to graphene: (13x13)/(12x12) on Ir(111),[55,56,58] Rh(111),[59] and Ru(111)[49] and (10x10)/(9x9) on Pt(111).[59] However, on Pt(111), the corrugation is so weak that no nanomesh forms. On the lattice-matched Cu(111) and Ni(111), *h*-BN grows flat as graphene.[60–62]
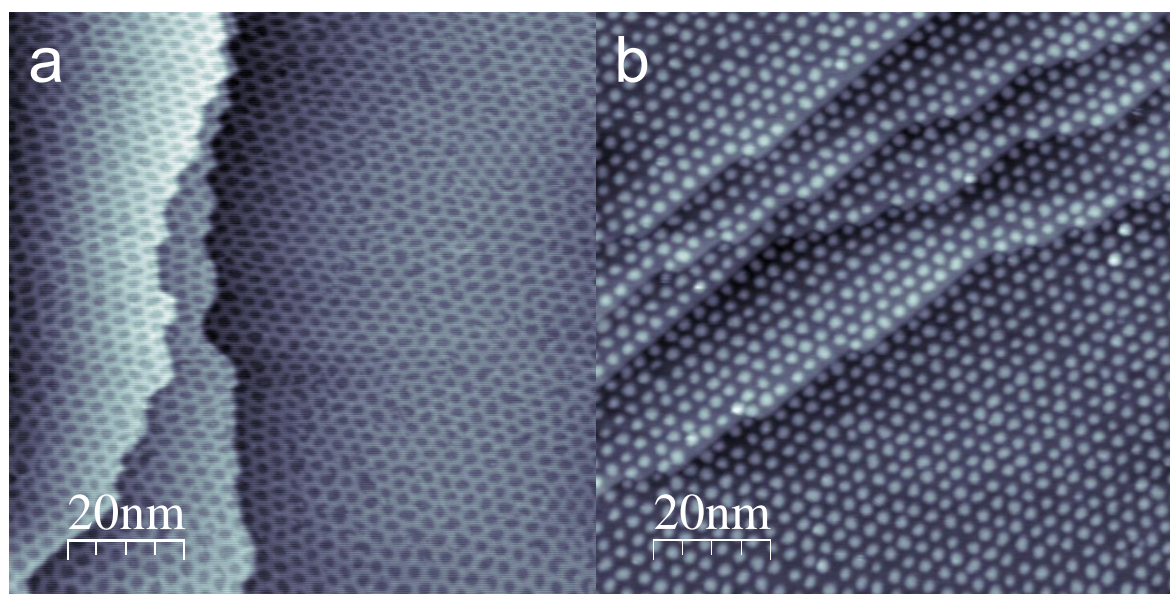
Figure 2.8: STM images of the a) freshly prepared *h*-BN/Rh(111) nanomesh and b) with 0.094 ML Pt supported on *h*-BN/Rh(111) forming Pt nanocluster arrays. Both pictures were taken at room temperature.

The chemical inertness and the Moiré structure make graphene and *h*-BN supported on transition metals a great substrate to grow nanocluster arrays. Such nanoclusters can be utilized as model system to bridge the materials gap between flat single crystals and industrial catalysts.[63] The latter usually consist of metal nanoparticles of various size and shape on oxide supports. While for model catalysis one can deposit more defined nanoclusters on highly ordered, flat oxides, the oxide

support always has a strong influence to the experiments. Chemical reactions can take place on the oxide and oxide-nanoparticle-interface, and species can diffuse between the nanoparticles and the support – spillover, and reverse-spillover. Nanoclusters on graphene or h-BN do not show these effects, as no adsorbates stick to the chemically innocent support. Thus, all observed processes only happen on the nanoclusters. Electronic interactions with the substrate do, of course, still exist. The other advantage is the template effect provided by the Moiré pattern. It leads to well-ordered nanocluster arrays with a narrow size-distribution, which makes the investigation of size-dependent effects easier. According to X-ray diffraction results of nanocluster arrays on graphene/Ir(111), they can be seen as hexagonal truncated pyramids.[64] Furthermore, it suppresses sintering processes compared to a flat support, making the system more robust. Figure 2.8b shows a Pt nanocluster array supported on an h-BN/Rh(111) nanomesh. Beside the interest in these nanocluster arrays themselves,[20,51,65–69] they are used to investigate numerous processes like sintering/thermal stability,[21,23,70–73] surface dynamics,[64,73] adsorption processes,[22,23,73,74] poisoning,[75,76] coking, and chemical reactions[22–24,77] and their kinetics.[23] Further examples will be presented in the following chapters in detail.

3   Sulfur on Metal Nanocluster Arrays

Palladium[9] and Platinum[5,6] catalysts are used in numerous applications. As sulfur and its oxides are common impurities in several feedstocks, the deactivation of catalysts through poisoning with sulfur is a widespread challenge for Pd[11,12] and for Pt.[7,10] The lowering of the catalyst's activity can happen by physically blocking the active sites, by modification of the adsorption properties or chemical nature of these sites through changing their electronic and geometric structure, and by hindrance of the diffusion of other adsorbates.[4] The regeneration of the catalyst activity, therefore, requires the removal of sulfur.[78]

In this chapter, Pd and Pt nanocluster arrays on the graphene/Rh(111) Moiré are used as a model system to investigate how sulfur changes the behavior of adsorbates using the probe molecule CO to observe changes in available adsorption sites on Pd and Pt nanoparticles. Figure 3.1 presents a scheme of such a nanocluster with the existing adsorption sites. The oxidation of sulfur as a possible way to remove it from Pt nanoclusters is the content of the third subchapter. Here, also insights into the oxidation kinetics are gained.
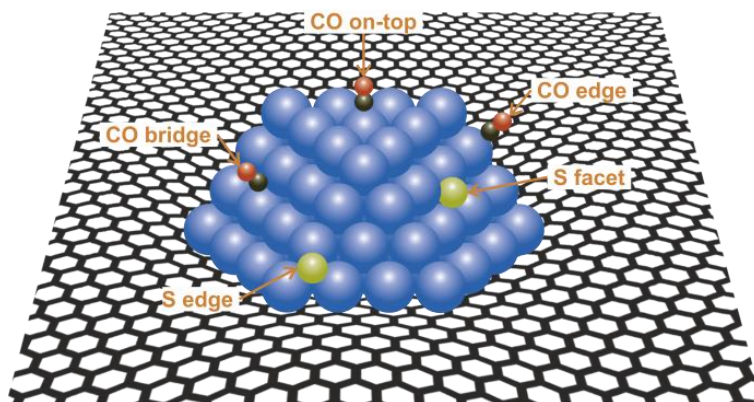
Figure 3.1: Schematic drawing of a Pt nanocluster with 92 atoms corresponding to a nominal platinum coverage of 0.8 ML on the graphene/Rh(111) Moiré. The different possible adsorption sites of CO and S are marked.

In all experiments, the sulfur deposition was conducted by adsorbing SO_2 onto the stabilized nanoparticles and subsequent heating to 500 K. Thereby, SO_2 disproportionates to elemental S and SO_3. SO_3 desorbs from the nanoparticles, leaving sulfur behind.[24]

3.1 Sulfur Poisoning of Palladium Nanocluster Arrays [P1]

At first, the poisoning of Pd nanocluster arrays supported on graphene/Rh(111) is presented. Figure 3.2 is a scheme of this process. To investigate the blocking of the cluster surface, CO was used as probe molecule. The adsorption process of CO on Pd nanoclusters preadsorbed with $\theta_{S, rel}$ = 0.14 ML is shown in Figure 3.3 as a plot of *in situ* C 1s XP-spectra and the fitted spectrum measured at CO saturation.
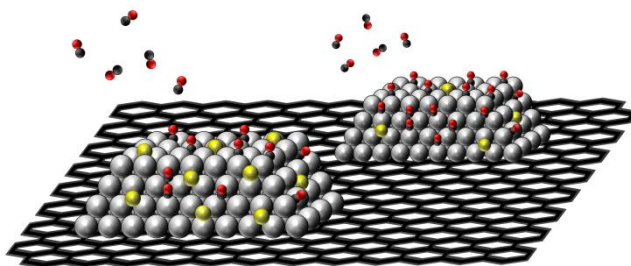

Figure 3.2: Scheme of the CO-adsorption on sulfur-poisoned Pd nanoparticles supported on graphene/Rh(111).

The thick black spectrum in Figure 3.3a shows the pristine Pd particles after poisoning with sulfur. The blue spectrum was recorded after saturation of the particles with CO. Both spectra show the two characteristic signals of graphene, at 285.08 and 284.53 eV, resulting from different interaction strengths of the carbon atoms in the Moiré pattern with the Rh(111) substrate.[53] After adsorption of CO, the graphene signals are slightly damped (blue spectrum in Figure 3.3a). Upon increasing the CO exposure, CO-related peaks evolve at ~286 eV. For a quantitative analysis, the spectra are fitted. Figure 3.3b shows the resulting fit, with the slightly damped graphene signal (orange), a small carbide contribution at 283.83 eV (magenta), and two CO-related peaks, CO^A at 285.99 eV (green) and CO^B at 286.11 eV (blue). As the surface of the Pd nanoparticles is considered to consist of different edges and facets,[21] the assignment of the CO species is not straightforward but can be done by considering the binding energies of CO on single crystalline surfaces.[79,80] From this comparison, the species at 285.99 eV (CO^A) is assigned to CO adsorbed at Pd steps and at terrace hollow sites, while the species at 286.11 eV (CO^B) is assigned to CO bonded to terrace bridge and possibly top sites.

_____
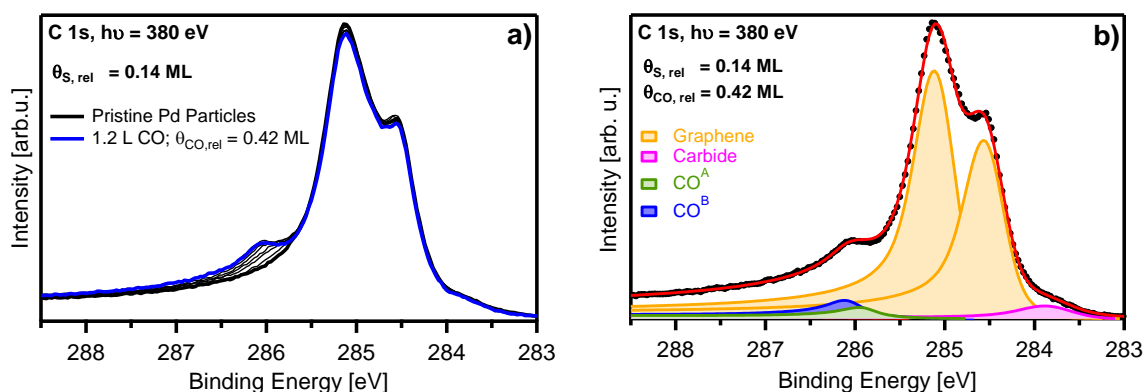
Figure 3.3: Adsorption of 2 x 10^{-9} mbar of CO on 0.53 ML of Pd/graphene/Rh(111) at 150 K for a sulfur precoverage of $\theta_{S, rel}$ = 0.14 ML: a) selected C 1s spectra during adsorption up to exposures of 1.2 L (blue spectrum); b) fit of C 1s spectrum at 1.2 L CO.

Similar measurements have been performed for different sulfur coverages, that is, $\theta_{S,rel}$ = 0.00, 0.04, 0.10, and 0.14 ML. The corresponding quantitative analyses are shown in Figure 3.4a (total CO coverage) and 3.4c (individual species). The measurements performed with different amounts of sulfur show that the total amount of adsorbed CO at saturation is reduced by the preadsorbed sulfur, from 0.75 ML for the sulfur-free particles to 0.42 ML for $\theta_{S, rel}$ = 0.14 ML, that is, to 56%.

The analysis further shows that not only the amount of CO decreases with an increasing amount of adsorbed sulfur, but also the relative site occupation changes. The CO^A species (full symbols) shows a maximum for all experiments; this maximum is reached at a lower exposure and a lower coverage of CO for increasing amounts of sulfur, which is attributed to the fact that less free highly coordinated adsorption sites remain in the presence of sulfur. At exposures above 0.3 – 0.4 L, the CO^B species (open symbols) grows, and simultaneously also a rearrangement (depopulation) of already adsorbed CO from step/hollow sites occurs. The CO coverage saturates at ~0.7 L, with the saturation coverage decreasing with an increasing amount of coadsorbed sulfur. This reduction is more distinct for the step/hollow species (CO^A), with a reduction by 55% (that is, from 0.375 to 0.17 ML) than for CO^B at bridge/top sites with a reduction by 31% (that is, from $\theta_{CO, rel}$ = 0.375 to 0.26 ML), for 0.14 ML S (black symbols).
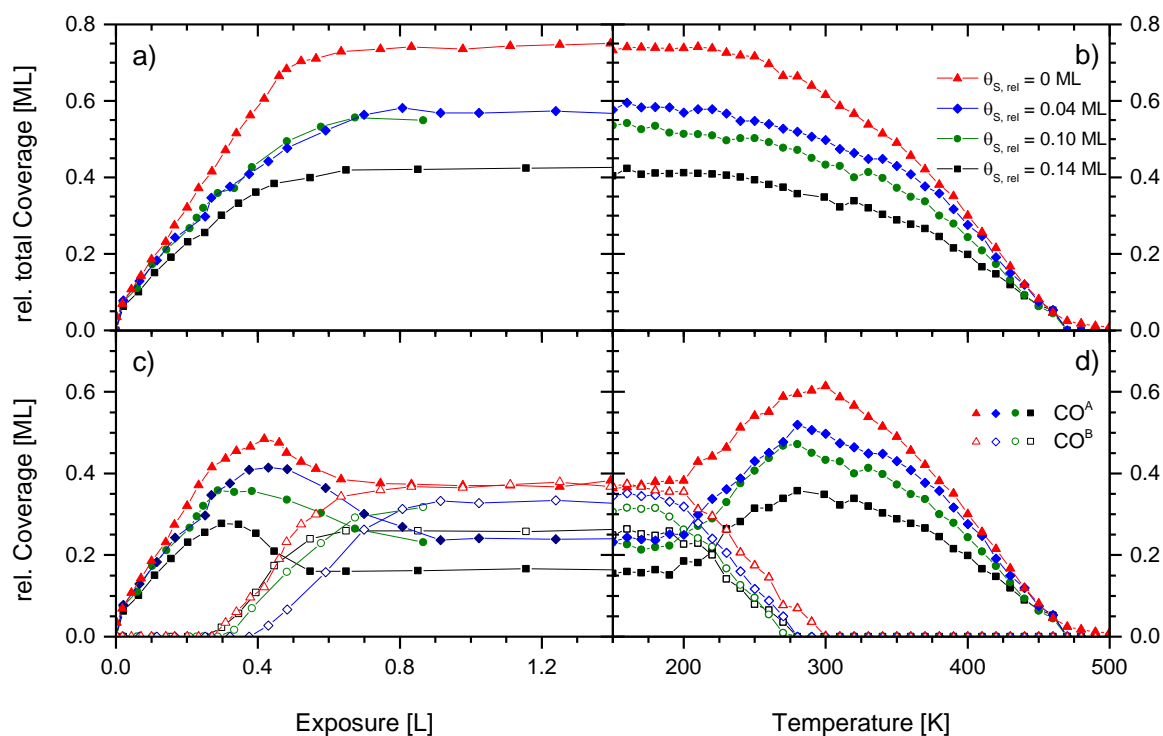
Figure 3.4: Quantitative analysis obtained from fitting C 1s spectra measured during CO adsorption at a pressure of 2 x 10^{-9} mbar at 150 K and successive desorption of CO on sulfur-free and sulfur-poisoned Pd-nanoparticles on graphene/Rh(111): a) Total CO coverage and c) individual CO coverages (CO^A and CO^B) during adsorption as obtained by peak fitting (see, *e.g.* Fig. 1c); b) Total CO coverage and d) individual CO coverages during TPXPS of CO, β = 0.5 K/s.

This behavior can be understood considering the fact that sulfur prefers to bind to highly coordinated sites, like step or hollow sites. We find that the total amount of CO is reduced from 0.75 to 0.43 ML (Figure 3.4a). Considering a maximal sulfur coverage of $3/7 \approx 0.43$ ML on Pd(111)[81,82] and a linear decrease of the CO coverage with $\theta_{S,\ rel} = 0.14$ ML should reduce the adsorption sites for CO by 33%, that is, from 0.75 to 0.50 ML. On the other hand, on Pd(100), total blocking of CO adsorption is achieved already for 0.25 ML S;[83] here, 0.14 ML should reduce the adsorption sites by 56%, that is, from 0.75 to only 0.32 ML. The fact that our result of $\theta_{CO,\ rel} = 0.42$ ML falls in between these values is an indication that the surface of the nanoparticles is comprised of a mixture of (111) and (100) facets. This is also supported by a linear extrapolation that leads to a sulfur coverage of 0.36 ± 0.03 ML that would lead to a complete blocking of all adsorption sites for CO. Again this is in between the results expected for (111) and (100) facets.

Changes can also be followed in the S 2p core level spectra upon CO adsorption. For the sulfur precovered, CO-free particles, one sulfur species is found that is assigned to sulfur bonded in

_____

hollow or edge sites. During CO adsorption, a second species occurs. The second species is explained by adsorbate-adsorbate interactions between sulfur and CO, which possibly induce a site change of part of the sulfur atoms. Interestingly, a quantitative analysis shows that, independent of the sulfur amount, the distribution of both sulfur species is always one to one at CO saturation. Based on this 1:1 ratio, it is proposed that due to coadsorbed CO, S is displaced towards a neighboring S atom, thereby forming an S pair at different adsorption sites. The driving force for this compression is the creation of addional adsorption sites for CO, and also explains the site change despite the fact that on the clean surface sulfur is known to be immobile at temperatures below 180 K.[84]

To complete the investigations, the thermal evolution of the adsorbed CO layers was studied. When heating the sample, the behavior observed during adsorption is reversed. The quantitative analysis of the C 1s spectra from the TPXPS in Figure 3.4b (total CO coverage) and 3.3d (individual species) shows that two processes occur parallel between 200 and 300 K. The CO^B species decreases by desorption and also a rearrangement to step/hollow sites is found, which is the reversal of the observations during the adsorption. At 300 K, the CO^A species shows a maximum before desorbing at higher temperatures. The whole desorption process is finished at 475 K and is not influenced by the preadsorbed sulfur since all experiments show the same behavior at the same temperatures, independent of θ_S. For sulfur, the desorption of CO overall leads to an inversion of the effects observed during the adsorption. As for the adsorption, these effects are stronger for smaller amounts of sulfur. After cooling the sample down, the original S 2p spectrum is observed. Therefore, the CO adsorption-desorption cycle is reversible.

In summary, sulfur adsorbs at highly coordinated sites and blocks these sites for CO. Other adsorption sites are blocked to a minor degree. As the desorption temperatures of CO are independent of the sulfur amount, the Pd-CO bond-strength seems not be effected by sulfur. Thus, blocking of adsorption sites on Pd by sulfur happens via steric hindrance, while electronic effects seem not to play a role. The degree of site-blocking is in between that of Pd(111) and Pd(100) surfaces, which indicates the nanocluster surface to consist of a mixture of (111) and (100) facets. Interestingly, coadsorbed CO influences the preadsorbed sulfur, that is, indication is found for a displacement of S atoms such that S pairs are formed on the surface, creating more space to adsorb CO on the nanoparticles.

3.2 Sulfur Poisoning of Platinum Nanocluster Arrays [P2]

In this chapter, the influence of preadsorbed sulfur on the adsorption behavior of CO on Pt nanoparticles supported on graphene/Rh(111) is discussed. Figure 3.5 provides a scheme of this process. Figure 3.6 shows as an example the C 1s spectrum of a CO-saturated surface with a sulfur precoverage of θ_S = 0.08 ML and the corresponding peak fitting. The two signals at 285.09 and 284.51 eV are characteristic of graphene on Rh(111) and result from the different interaction strengths of the carbon atoms in the Moiré structure with the single crystal surface.[53]
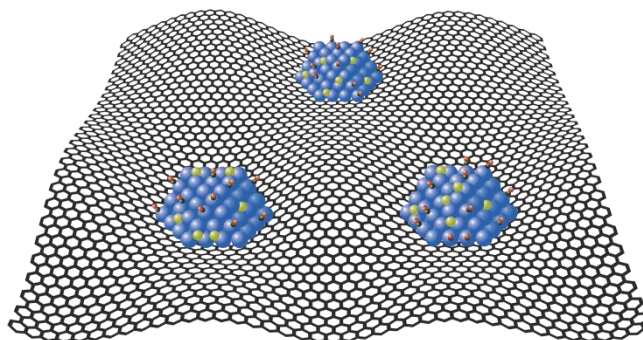

Figure 3.5: Scheme of the CO-adsorption on sulfur-poisoned Pt nanoparticles supported on graphene/Rh(111).

The CO signals are fitted with three peaks. By comparison with results from sulfur-free Pt nanoclusters[23] as well as flat and stepped Pt surfaces,[85–87] they are assigned the following: The peak at 286.8 eV (green) stems from CO at on-top sites on the cluster facets; the peak at 286.2 eV (orange) is due to CO at bridge sites on the cluster facets, similar to Pt(111), where the two species are found at 286.8 and 286.1 eV.[85] The peak at 286.5 eV (magenta) is attributed to cluster edge and kink sites, by comparison to the stepped Pt(355) surface, where an additional CO signal at 286.4 eV is assigned to CO at the step sites.

The quantitative analysis of the CO adsorption process is shown in Figure 3.7 for sulfur precoverages of 0.00, 0.06, 0.08, 0.12, and 0.17 ML. For each sulfur coverage, panel a) shows the CO coverages of the edge sites (red), the facet on-top sites (blue), the facet bridge sites (green), and the sum of on-top and bridge facet sites (black). With increasing sulfur precoverage, the CO saturation coverage on the nanoclusters decreases roughly linearly, from 0.49 ML CO for θ_S = 0.00 to 0.19 ML CO for θ_S = 0.17 ML, as indicated by the vertical dotted lines. By extrapolation, complete blocking of CO adsorption on the nanoparticles is estimated to occur around θ_S = 0.28 ± 0.07 ML. This compares very well with the amount of one-third of a monolayer, which is required for a complete

_____

blocking of CO adsorption on Pt(111), Pt(322), and Pt(355) single crystals.[84,88] Again, this indicates the similarity of these nanocluster arrays to the (111)-like surfaces.
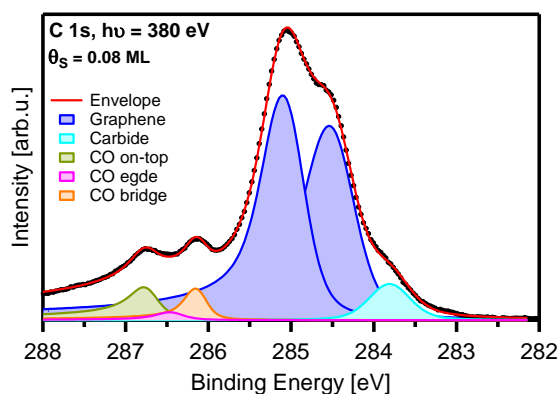

Figure 3.6: C 1s spectrum at CO saturation for θ_S = 0.08 ML, including fit results, on Pt nanoparticles on graphene/Rh(111); CO was dosed at temperatures of 120 - 150 K, and a pressure of 2×10^{-9} mbar; the nominal Pt coverage was 0.8 ML.

The edge sites are much more affected by site blocking than the facet sites: When comparing the CO saturation coverages for the sulfur-free cluster and for the sulfur–precovered cluster with θ_S = 0.17 ML, the coverage is lowered from 0.41 to 0.17 ML for the facets (as indicated by the black horizontal arrow), and from 0.09 to 0.02 ML for the edges/steps (red arrow). This latter, nonzero value shows that even at high sulfur precoverages, CO can adsorb at edge sites. It is attributed to gaps between the sulfur atoms at the edges of the particles. They arise from the finite size of the edges as compared to the stepped single crystals, where this behavior was not observed.

The preferential blocking of edge sites also leads to an earlier onset of the CO adsorption on the facet sites, from 0.05 ML for θ_S = 0.00 ML to 0.005 ML for θ_S = 0.17 ML. For up to θ_S=0.08 ML, the CO edge saturation coverage saturates shortly after the onset of adsorption on the facets. Starting at θ_S = 0.12 ML (as deduced from an additional data set, not shown), however, CO adsorption on the edge sites of the particles is initially almost completely blocked, but can be achieved to some extent by high exposures (see data for θ_S = 0.12 and 0.17 ML). This indicates that CO displaces S from the edge sites, even at 150 K, as an corresponding change in the S 2p signal is found, where S at edges and on facets are distinguishable. Additionally, a shift of the S 2p signal is observed during the adsorption of CO that could be due to the formation of compressed sulfur layers by CO, as was also found on Pt(111)[89] and on Pd nanoclusters in the chapter before.
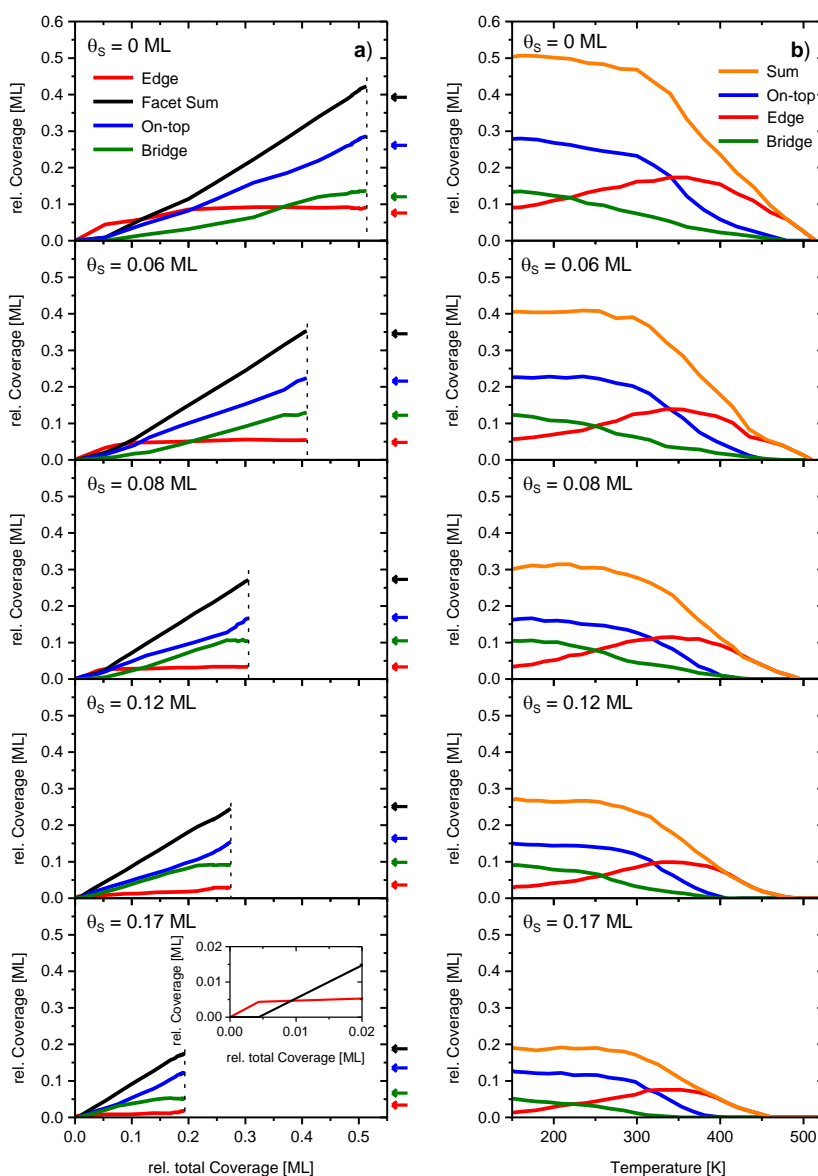
Figure 3.7: Quantitative analysis of the C 1s spectra collected during CO adsorption on Pt nanoparticles on graphene/Rh(111) (0.8 ML) at 120 - 150 K, with sulfur precoverages from 0 to 0.17 ML. a) Coverage of edge and facet on-top and bridge sites; the inset for θ_S = 0.17 ML shows a magnification of the beginning of this experiment; black, blue, green, and red arrows are a guide to the eye for the final coverages. b) Thermal evolution of the saturated CO layers.

The amount of θ_S = 0.12 ML, at which initial CO adsorption at edges is suppressed, is very similar to what is observed on Pt(355), where $\theta_S \approx$ 0.10 ML is required for a total blocking of the steps (on Pt(322), only $\theta_S \approx$ 0.06 ML is required due to the formation of double steps)[84]. This similarity is in line with the fact that both on clean Pt(355) and on the clean Pt clusters ~20% of the adsorbed molecules are found at step/edge sites. The small differences might be explained by the existence of

different density of edges/steps, but also by the existence of kinks and corners that are not (or only to a very small extent) present on the well-defined, stepped platinum surfaces.

Figure 3.7a also shows the effect of sulfur on the relative population of facet on-top and bridge sites at saturation (indicated by blue and green horizontal arrows). While the site blocking correlates almost linearly with θ_S for the on-top sites, small sulfur coverages ($\theta_S \leq 0.08$ ML) have nearly no effect on the coverage of bridge-bonded CO ($\theta_{CO, br} = 0.13$ ML). However, for $\theta_S = 0.17$ ML, both on-top and bridge sites are reduced to a very similar extent, that is, the occupation of bridge sites is reduced to less than half of its initial value ($\theta_{CO, br} = 0.05$ ML). A similar blocking behavior of bridge binding sites was found on a stepped Pt(322) crystal.[84] There, no blocking of CO bridge is observed up to $\theta_S = 0.06$ ML, while higher sulfur coverages lead to a strong decrease of the CO bridge population. Similarly, on the flat Pt(111) surface a strong suppression of bridge sites at high sulfur coverages is found.[88,90] The preadsorbed sulfur also influences the site preference during adsorption: For small S coverages up to 0.08 ML, less CO bridge sites are populated than on-top sites; for 0.14 and 0.17 ML both sites are initially populated to the same extent. At high CO coverage, on-top sites dominate, independent of the sulfur coverage.

Next, the thermal evolution of the adsorbed CO layers is addressed by temperature programmed XPS experiments. The quantitative analyses for selected sulfur precoverages after peak fitting are depicted in Figure 3.7b. During heating, the edge CO species increases, while CO on-top and especially the CO bridge species on the facets decrease. This increase of the edge species indicates a rearrangement of the adsorbed CO molecules upon heating, as was also observed for CO on Pt(322)[91] and platinum nanocluster arrays.[23] For the sulfur-precovered Pt clusters, the changes are more pronounced than for the sulfur-free case. For all S coverages, the maximum population of CO at edge sites is reached at 340 ± 10 K; interestingly, the increase is roughly independent of θ_S, with a value of ~0.08 ML CO, indicating that always roughly the same amount of CO diffuses to the edges. The increase in edge site occupation by CO is attributed to the fact that sulfur blocks these sites at low temperatures. Upon heating, a site exchange of S and CO occurs, such that CO replaces S at the edge sites. Such a site exchange was also found on stepped Pt(322) and Pt(355) surfaces.[84] At the same time, a pronounced change in the S 2p peak shape is observed between 230 and 330 K. It is caused by the replacement of S at edge sites by CO, which leads to a higher population of the facet sites. Interestingly, the displacement of sulfur is less pronounced for high sulfur coverages, because the number of empty sites on the facets is not sufficient for all sulfur atoms that would be

displaced by CO. A comparison of the amounts of migrated CO and S results in two CO molecules displacing one sulfur atom at the edge sites. Based on this observation, the difference in strength between sulfur edge and facet bonds is smaller than the corresponding difference for CO, and the replacement does not occur already at 150 K only due to kinetic limitations.

At 300 K, CO desorption sets in as a second process, leading to a fast decrease of both on-top and bridge CO species. With increasing S coverage, desorption of the on-top species shifts to lower temperatures by ~30 K, from ~360 K for the sulfur-free case to 330 K at θ_S = 0.17 ML. The denoted values correspond to the temperatures, where the signal has decreased to half of the initial coverage (as an estimate of the inflection point, with the highest desorption rate). Due to the lower signal of the bridge species, such an analysis is not possible; however, the individual behavior of facet on-top and bridge sites can still be compared by the temperature, where their XPS signals vanish. For the sulfur-free case (top panel in Figure 3.7b), both disappear at 470 ± 10 K. This similarity vanishes at higher sulfur coverage. For θ_S = 0.17 ML, the on-top species disappears at 390 ± 10 K, the bridge species already at 330 ± 15 K. This more drastic change is related to the displacement of sulfur from the edge sites to the facets where sulfur preferentially occupies highly coordinated sites leading to a loss of bridge bonded CO. The edge CO contributions follow a rather similar path, although the initial coverage varies strongly. Yet, the desorption temperature of the CO edge species decreases with increasing sulfur coverage, from 455 K on the sulfur-free clusters to 410 K (all ± 10 K) for θ_S = 0.17 ML. At high temperatures, the decrease of the total CO coverage mimics the behavior of the edge species, because CO at edge sites is the most stable surface species.

When comparing the results to stepped Pt surfaces, the overall behavior is similar to Pt(355), especially the pronounced diffusion of CO to the steps at elevated temperatures, and the reduction of the desorption temperature caused by sulfur with also a stronger effect on the step species. In contrast, the CO bridge species is more stable during annealing on the nanoclusters than on the Pt(355) surface, where the rearrangement to the steps is finished at 220 K, while it takes up to 330 K on the clusters. On Pt(322), the rearrangement sets in at 200 K and is completed at 330 K.[84]

CO desorption also reverses the shift of the S 2p spectra until at 430 K the original situation prior to CO adsorption is restored, as it enables the sulfur to diffuse back to the edges. Also, the damping of the S signal that was observed during CO adsorption is reversed. This temperature-dependent behavior makes the sulfur adsorption on Pt nanoclusters probed by CO well comparable to that on the stepped Pt(111) surfaces, Pt(355) and Pt(322).

To conclude the influence of sulfur on the adsorption and desorption of CO on graphene-supported Pt nanocluster arrays: Both sulfur and CO prefer the adsorption at edge sites over facets. Thus, a strong blocking effect for CO on edges was observed with a total blocking of edges at θ_S = 0.12 ML. On facets, on-top sites are blocked already by small amounts of sulfur, while bridge sites are not affected until θ_S = 0.08 ML. At higher coverages, also a strong blocking effect of bridge sites sets in. At about θ_S = 0.28 ML, all sites are blocked for CO. Upon heating, first, a site exchange of CO and S occurs. CO displaces S from the edges to facets, with the maximum CO coverage at edges reached at 330 K. This effect is more pronounced for small sulfur coverages. At higher temperature, the desorption of CO enables the sulfur to diffuse back to the edges. While the overall desorption behavior is not influenced by sulfur, a reduction of the desorption temperature was found for CO bound to edge sites. Because of this, the poisoning effect of sulfur works primarily by blocking of sites, especially edge sites, while electronic effects play a minor role.

3.3 Oxidation of Sulfur on Platinum Nanocluster Arrays [P3]

After discussing the poisoning effects of sulfur, this chapter describes the oxidation of sulfur on Pt nanocluster arrays supported on the graphene/Rh(111) Moiré, see Figure 3.8 for a scheme. Oxidation is one way to remove sulfur from metal surfaces by creating volatile SO_2 and SO_3 species and, thereby, regenerating the catalyst's activity. Therefore, isothermal oxidation experiments were conducted at sample temperatures between 350 and 450 K and an oxygen pressure of 1.4 x 10^{-6} mbar.
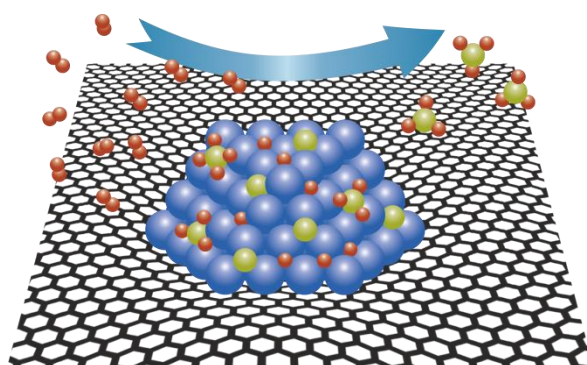

Figure 3.8: Scheme of the sulfur oxidation on Pt nanoparticles supported on graphene/Rh(111).

The following SO_x species can be observed in the oxidation process: A main contribution at 162.31 eV ($S\,2p_{3/2}$) is assigned to S adsorption at edges, with a shoulder at 162.00 eV ($S\,2p_{3/2}$) belonging to S adsorbed on the facets of the nanoparticles. The assignment to edge and facet sites is based on the similarity of the binding energies of the observed species to those at step and terrace sites on Pt single crystals, respectively.[23,24,76] Upon exposure to molecular oxygen from the supersonic molecular beam, a fast initial shift of the S 2p signal by ~100 meV to higher binding energy is observed, which is due to lateral interactions of atomic oxygen with the preadsorbed sulfur. As all measurements were conducted above 300 K, the oxygen molecules dissociate directly after adsorption.[92] After that, a continuous shift of the sulfur signal towards lower binding energies occurs. This shift is assigned to a slow displacement of sulfur by oxygen from the edge sites to the facet sites. Such a displacement from steps to terraces was also found on Pt(355), Pt(322), and in a study of Pt nanoclusters.[19] New surface species are formed with a binding energy of 166.03 eV, which is typical for SO_3 and at 167.10 eV that is SO_4.[19] As no SO or SO_2 are detected in the experiments, these intermediates of the oxidation process have to react very fast to the next higher oxidation state. Therefore, the first reaction step from S to SO has to be the rate-determining step.

The quantitative analyses of two experiments at 350 and 430 K are shown in Figure 3.9a and 3.9b, respectively. In addition, the behavior of the facet signal and the total signal of atomic sulfur is plotted in a semi-logarithmic plot in Figures 3.9c and 3.9d, respectively, along with the data from similar measurements at 375 and 400 K. At 350 K (Figure 3.9a), S_{edge} (red) decays roughly exponentially, while the amount of S_{facet} (green) increases continuously. This behavior indicates a displacement of sulfur from the edges to the facets by oxygen. The process is rather slow, as it occurs throughout the whole experiment up to 800 s; note that the particles are saturated with oxygen after a few seconds due to the high pressure on the sample. As an estimate, a Pt(111) surface is saturated after ~30 s and a stepped surface even faster in about 4 s due to an eight times higher sticking coefficient.[93] In addition to the replacement of atomic sulfur from the edges, SO_3 (blue) slowly forms and saturates at around 400 s. No SO_4 (orange) forms at this temperature. The constant sum of all sulfur species (atomic S and SO_3) indicates that after the saturation of SO_3, no sulfur components desorb from the nanoparticles. However, the overall amount of sulfur decreases at the beginning of the experiment, when the conversion rate is high. This is due to a partial desorption of SO_2 and possibly SO_3 at 350 K, as found in TP-XPS experiments of SO_2 and SO_2/O on different platinum surfaces.[24,94,95]

_____
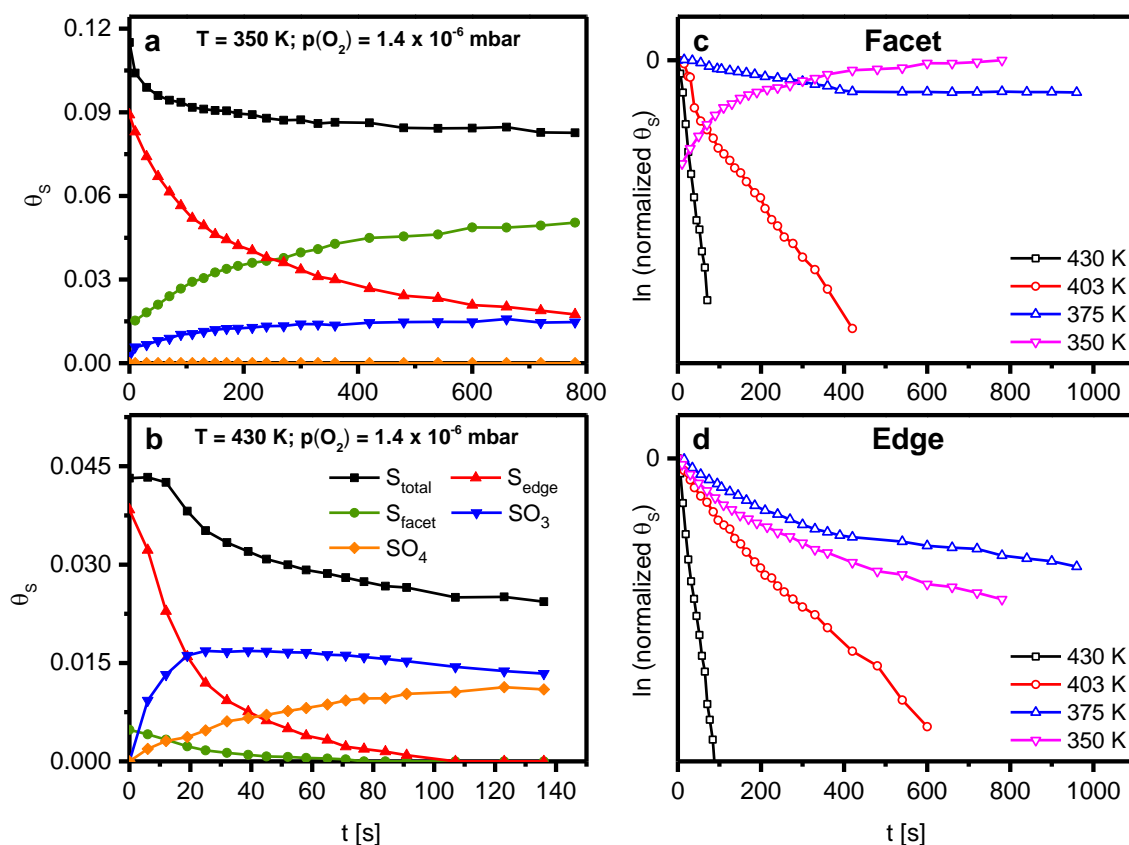
Figure 3.9: Quantitative analyses of isothermal oxidations of sulfur on 0.8 ML Pt∕graphene∕Rh(111): a) At 430 K and an oxygen pressure of 1.4 x 10^{-6} mbar, b) at 350 K and an oxygen pressure of 1.4 x 10^{-6} mbar. c) Logarithmic plots of normalized sulfur coverage for facet species and d) edge species vs. time for sulfur oxidation on 0.8 ML Pt∕graphene∕Rh(111) at various surface temperatures and an oxygen pressure of 1.4 x 10^{-6} mbar.

At 430 K (Figure 3.9b), the oxidation of elemental sulfur to SO_3 (blue) and subsequently to SO_4 (orange) is the dominant surface process. From the beginning, a decay of S_{edge} (red) and S_{facet} (green) is observed. Thereby, the reaction of S_{edge} is faster than that of S_{facet}. During an initial induction period, the total S coverage is constant. This induction period thus includes the accumulation of oxygen and sulfur oxides on the surface, before SO_x species desorb, which occurs until the end of the experiment. The amount of SO_3 increases due to the oxidation up to 25 s, where it has its maximum, and decreases slowly after that. The final oxidation product SO_4 is detected from the very beginning and until the end of the experiment. Although no displacement of sulfur from the edge sites to the facets is observed, this process probably also occurs at these temperatures. From these observations, it is obvious that the evaluation of the reaction kinetics of the sulfur oxidation on Pt nanoclusters is not straightforward, as diffusion/displacement, oxygen accumulation, and the reaction at different reactive sites occur simultaneously with different kinetics. This contrasts the

situation on Pt(111) and Pt(355), where pseudo-first-order reaction kinetics was observed for low sulfur coverages under the excess of oxygen.[19]

The absence of a simple first-order kinetics is most evident from the semi-logarithmic plots of the amounts of sulfur adsorbed on facets (Figures 3.9c) and edge sites (Figure 3.9d) for 350, 375, 403, and 430 K, at an oxygen pressure of 1.4×10^{-6} mbar. Sulfur at facet sites increases at 350 K and non-linearly decreases at 375 and 403 K. Only for 430 K, a linear decrease is found, as would be expected for first-order kinetics. For the edges, again a non-linear behavior is observed at 350, 375, and 403 K, and only at 430 K, the decrease is linear. From the absence of a linear decrease for all temperatures, it is clear that the activation energy cannot be determined from a simple Arrhenius analysis.

Nevertheless, it is interesting to compare the rate of the sulfur consumption on the different model surfaces studied, that is, Pt(111),[19] Pt(355),[19] Pt(322), and the nanoparticle arrays. Using experiments at a temperature of ~405 K and a pressure of $1.4\text{-}2.0 \times 10^{-6}$ mbar for comparison, it shows that the oxidation reaction is slowest on Pt(111), where the amount of elemental sulfur decreases to 30% of the initial coverage over the time of 900 s. The reaction on Pt(355) is fastest, that is, the surface is sulfur-free already after ~60 s. For the nanoparticles and Pt(322), the behavior is quite similar initially and in between these two extremes, attributed to the fact that they both provide fourfold-hollow sites for sulfur adsorption; see Refs.[24,76,84] The high bond strength of sulfur to these sites is likely to result in a very slow exchange of sulfur and oxygen at the [100] edge/step sites. This slows down the sulfur oxidation in comparison with Pt(355) with its [111] steps, where this exchange is very fast, and the reactive oxygen species is formed at the step/edge sites.[19] The difference between the nanoclusters and Pt(322) is at least partly due to the higher sulfur coverages in the nanocluster experiment, where not only the edge sites but also the facet sites are populated. Preparation of smaller S coverages on the nanoclusters would lead to a low signal to noise ratio that is not compatible with fast measurements. Finally, site blocking by the reaction products, $i.e.$, SO_3 and SO_4, also cannot be neglected on the nanoclusters. This effect increases during the experiment. It is negligible on the single crystals with low S coverages, since there is enough space, so the reaction products do not hinder the reaction.

To summarize, the oxidation of sulfur on graphene-supported platinum nanocluster arrays was studied $in situ$ using high-resolution XPS at temperatures between 350 and 430 K. From the XP spectra, SO_4 was identified as the final oxidation product, with SO_3 being the only observable

_____

intermediate. Therefore, the other oxidation states SO and SO_2 react very fast to the next oxidation state and that the first reaction step that is from S to SO is rate determining. During the adsorption of oxygen, a displacement of sulfur from the edges to the facets by oxygen is observed. In contrast to Pt(111) and stepped Pt(355), the reaction kinetics cannot be described by simple pseudo-first order behavior. The study emphasizes the importance of steps/edges and defects for oxidation catalysis. Furthermore, the results suggest that Pt nanoparticle arrays are an excellent model system because an atomic/molecular understanding of the kinetics becomes accessible when using *in situ* methods such as synchrotron-based fast HR-XPS.

4   Bimetallic PdPt-Alloy Nanocluster Arrays [P4]

As mentioned above, both palladium and platinum are widely used catalytic materials. They are utilized as single metals[96,97] as well as in alloys.[98] Alloying with Pd is used, *e.g.*, to enhance the performance and stability of Pt catalysts in reactions that include an oxygen reduction,[99] or to stabilize species like aldehydes that would decompose on the single metals.[100] Bimetallic nanoparticles show improved resistance towards sintering[101] and a higher activity in reactions like the CO oxidation[102] compared to their monometallic counterparts.

To produce alloy nanoclusters, Pd and Pt were deposited simultaneously on the sample by electron beam evaporation at 150 K. This resulted in nanoclusters consisting of nominally 0.87 ML Pd and 0.68 ML Pt, *i.e.*, they include 28% more Pd than Pt. The alloy forms during co-evaporation as random, single atoms from the evaporators combine on the substrate. The process is further thermodynamically driven by the negative enthalpy of mixing (-4.8 kJ/mol[103–105] at 150 K for $Pd_{50}Pt_{50}$).[106,107] A scheme of such an alloy nanocluster is presented in Figure 4.1 together with a graphical summary of the results of the present chapter.
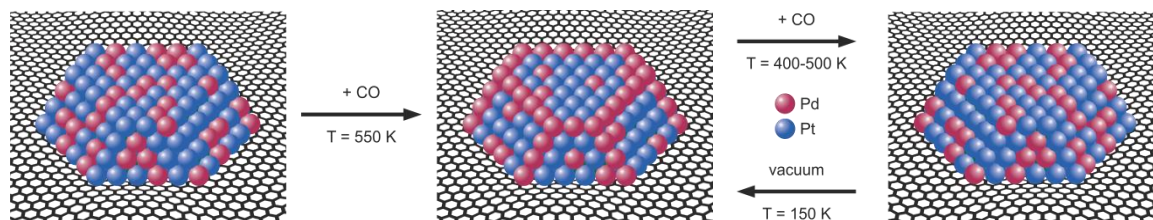
Figure 4.1: Scheme of the restructuring during the stabilization process and the dynamics of bimetallic PdPt alloy nanoclusters supported on graphene∕Rh(111).

To investigate the adsorption site occupation and the dynamic behavior of the metal distribution during adsorption and thermal treatment of CO on PdPt alloy nanocluster arrays supported on the graphene/Rh(111) Moiré, a series of CO adsorption and desorption experiments on *in situ* prepared PdPt clusters was conducted. Figure 4.2 shows selected fits of C 1s spectra during the first and the second CO-adsorption/desorption cycle on the freshly prepared nanoparticles. All CO coverages will be given relative to the maximum total CO coverage $\theta_{CO, max}$.

The following species occur in the C 1s spectra: Two contributions from graphene at 284.47 and 285.07 eV that are assigned to the strongly and weakly bound regions of the graphene Moiré structure on Rh(111), in line with literature.[53] A small peak at 283.71 eV is carbidic carbon that is a

residue from the preparation process. The CO peaks are assigned by comparing their binding energies to literature values for flat Pt(111)[79,108] and Pd(111),[79,108] stepped Pt single crystals,[86,91] and pure Pd[22,23] and Pt[22,23] nanoclusters. Note that in all cases small coverage-dependent shifts were observed.[108,109] Also, with increasing coverage, all peaks shift to higher binding energies by ~100 meV, which is attributed to increasing CO-CO interactions.[85] From this comparison, the peak at 286.60 eV is assigned to CO at Pt on-top facet sites and the peak at 286.35 eV to CO at Pt edge sites. The peak at 286.03 eV is attributed to a mixture/combination of CO bridge species at Pd, Pt or mixed PdPt sites. The three sites likely have slightly different binding energies. This is concluded from the significant increase of the full width at half maximum (FWHM) from 0.35 eV for pure Pt nanoclusters to 0.54 eV for the alloy clusters. In comparison, the FWHMs of the other CO species are identical (CO[Pt edge], CO[Pd edge/hollow]) or increase only slightly (0.52 to 0.60 eV in the case of CO[Pt on-top]). It also becomes apparent that on the alloy all Pt-CO species are shifted by ~100 meV to lower binding energies, compared to the monometallic systems, which might be related to the different chemical surrounding, or a different final state screening. These results are in line with a study on Ag/Pt alloys, where the C 1s binding energies of CO adsorbed at specific alloy sites were shifted up to 150 meV compared to pure Pt(111), depending on the fraction of Ag on the Pt(111) surface.[109]

During the first CO adsorption experiment, that is, on the untreated nanoclusters (Figure 4.2a), the Pt edge sites (green) are occupied by CO right from the beginning with a coverage of 0.06, caused by adsorption from the background gases during the preparation process. The Pt edge site occupation reaches a final relative coverage of 0.11. The CO[bridge] sites (blue), which are also partly occupied from the very beginning (0.06) become the dominant species during the experiment, with a maximum relative coverage of 0.59. The CO[Pt on-top] sites (black) grow only at higher coverages and become the second most common species at saturation with a relative coverage of 0.30. Please note that CO[Pd on-top] (286.29 eV) has nearly the same C 1s binding energy as CO[Pt edge] (286.35 eV). Nevertheless, the observed peak should be solely due to CO[Pt edge] sites. This conclusion is based on the observation that CO[Pd on-top] is only present in densely packed CO layers, while the here identified CO[Pt edge] is already present in diluted CO overlayers.[79]

To investigate possible restructuring phenomena, the CO-covered alloy nanoclusters were heated to 550 K, while continuously recording XP-spectra, see Figure 4.2b. This leads to a complex desorption behavior that allows for insights into the dynamics of the restructuring process. Upon

heating, the relative coverage of $CO^{Pt\,on\text{-}top}$ (black) immediately starts to decrease, from of 0.30 at 150 K to 0.10 at 320 K, while at the same time the relative $CO^{Pt\,edge}$ coverage (green) rises from 0.11 to 0.26. The simultaneity of these processes indicates that a rearrangement of CO from the facets to the edges occurs. CO^{bridge} (blue) initially decreases only slightly, and then steeply above 260 K to finally vanish at ~480 K. Starting at 240 K, a new species develops at 285.76 eV (red) that is assigned to CO adsorbed on the edge and hollow sites of Pd, $CO^{Pd\,edge/hollow}$.[22,79] It reaches a small plateau at ~360 K before it starts to vanish above 385 K, together with the CO^{bridge} and $CO^{Pt\,on\text{-}top}$ species, until ~480 K. The $CO^{Pt\,edge}$ species is the most stable species and vanishes only at 500 K, that is, at ~20 K higher temperatures than the other species. The graphene signals significantly increase upon heating. This increase is attributed to a change of the particle morphology towards a more three-dimensional shape, which reduces the damping of the underlying graphene. Such a change was found before for single-metal nanoclusters.[21–23]
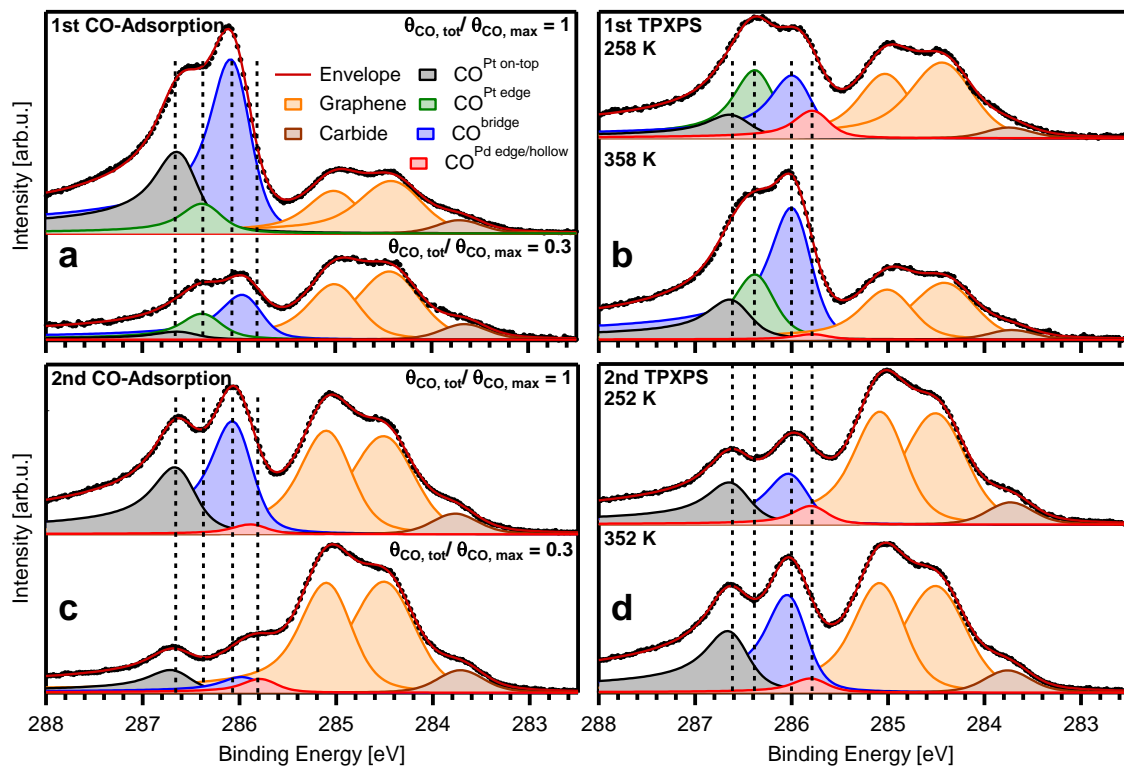
Figure 4.2: Fits of selected C 1s XP-spectra collected during CO-adsorption/desorption cycles on PdPt-alloy nanocluster arrays (0.87 ML Pd, 0.68 ML Pt) on graphene/Rh(111). a) First adsorption of CO at a pressure of 2 x 10-9 mbar at 150 K, b) first TPXPS with β = 0.5 K/s, c) second adsorption of CO at a pressure of 2 x 10-9 mbar at 150 K, d) second TPXPS with β = 0.5 K/s.

A second adsorption experiment was performed to characterize the shape changes during the first adsorption/desorption cycle, again with the idea to use CO as a probe molecule to access the surface

composition. The two exemplary, fitted spectra collected during CO adsorption, shown in Figure 4.2c, are remarkably different from the data measured in the first experiment for the as-prepared nanoclusters. The graphene signal has a much larger intensity, which is due to the restructuring of the nanoclusters in the first heating cycle and the resulting decreased damping of the photoelectrons from graphene. Upon CO adsorption, the $CO^{Pt\,on\text{-}top}$ species (black) increases at first, which contrasts the situation in the first cycle, where this species was only populated starting at a total CO coverage of 0.20. The increase of $CO^{Pt\,on\text{-}top}$ is followed by the increase of the CO^{bridge} species (blue) and the $CO^{Pd\,edge/hollow}$ species at 285.76 eV (red). Note that this latter species was not observed at all in the first adsorption experiment on the as-prepared nanoclusters. At a total CO coverage of 0.35, the $CO^{Pd\,edge/hollow}$ reaches its maximum relative coverage of 0.07 and after that decreases to 0.04 at saturation. At the same time, the CO^{bridge} species strongly increases and becomes the dominant species at CO saturation, with a relative coverage of 0.59. $CO^{Pt\,on\text{-}top}$ has reached a relative coverage of 0.37 at saturation. Interestingly, throughout the adsorption experiment, no signal characteristic of $CO^{Pt\,edge}$ sites (green) is observed.

This behavior is in stark contrast to what is found on the as-prepared clusters, and to what is found on monometallic Pt clusters and surfaces. On these systems, the first species to be populated is the Pt edge sites, whereas in the second CO adsorption experiment no CO bonded to Pt edge sites on the alloy nanoclusters is found. Therefore, in the course of the restructuring process in the first adsorption/desorption cycle, all Pi at edges has to be replaced by Pd atoms.

To further study possible restructuring phenomena, the CO-covered alloy nanoclusters were again heated to 550 K, see Figure 4.2d. The observed desorption behavior mirrors the behavior during the adsorption process. Above ~195 K, $CO^{Pt\,on\text{-}top,}$ and CO^{bridge} species desorb as the primary process and finally vanish at ~460 K. Simultaneously, a small rearrangement towards $CO^{Pd\,edge/hollow}$ sites with a maximum relative coverage of 0.09 around 360 – 380 K is observed, which also vanish at ~480 K. Interestingly, starting above 360 K, a small amount of $CO^{Pt\,edge}$ species (green) with a maximum relative coverage of 0.04 is found again. This observation indicates a dynamical change of the particle surface composition with temperature, such that – in the presence of CO – Pt atoms diffuse to the edge sites. The $CO^{Pt\,edge}$ species has its maximum intensity at ~420 K and is more stable than the other species, that is, it vanishes at ~500 K. Above this temperature, the nanoclusters are CO-free.

As a subsequent experiment shows no CO adsorption at Pt edge sites, the Pt at edges is again replaced with Pd during the cooldown of the sample. Overall, the C 1s spectra of this third adsorption mimic those of the second one, indicating that no further changes of the particles have occurred after the second CO adsorption/desorption cycle. They are stabilized.

The dynamic changes of the nanoclusters, that is, the observation of Pt edge sites above 360 K and other possible changes of the nanoparticle surface at elevated temperatures, were reproduced with a series of measurements with the molecular beam. Thereby, a high pressure (3×10^{-6} mbar at the sample surface) of CO and heating were applied for 5 min before and were maintained during each measurement. In Figure 4.3, the C 1s spectra for temperatures of 150 to 400 K, in the presence of the CO beam, show peaks characteristic of CO$^{Pt\ on\text{-}top}$, CO^{bridge}, and CO$^{Pd\ hollow/edge}$ species but no signal of a CO$^{Pt\ edge}$ species. They look similar to their counterparts from the TPXPS experiment, yet, with slightly higher CO-related peaks. This is due to the CO pressure of 3×10^{-6} mbar on the sample that causes a dynamic equilibrium between adsorption and desorption, while during the TPXPS experiment, the CO beam is switched off. The spectrum at 500 K displays a very different shape, that is, it is dominated by the CO$^{Pt\ edge}$ peak, indicating the creation of Pt edge sites in the presence of CO (this effect is to some extent already seen at 400 K).
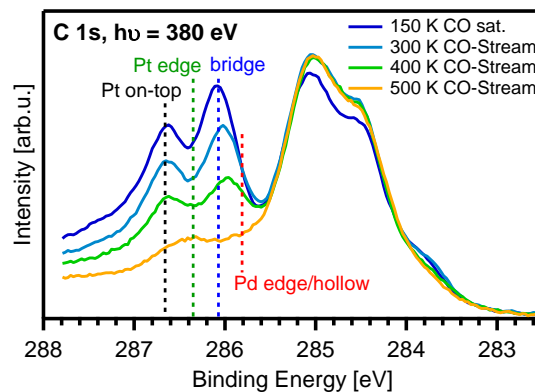
Figure 4.3: C 1s XP-spectra at a photon energy of 380 eV of PdPt-alloy CO-saturated nanoclusters (0.87 ML Pd, 0.68 ML Pt) on graphene/Rh(111) for temperatures of 300, 400, and 500 K with a CO pressure of 3×10^{-6} mbar applied on the sample for 5 min before and during the measurement. For comparison, the spectrum of the restructured particles saturated with CO at 150 K is shown.

In conclusion, the influence of CO on PdPt alloy nanocluster arrays supported on the graphene-Moiré on Rh(111) was investigated using *in situ* HR-XPS. Annealing of the as-prepared nanoclusters to 550 K after exposure to CO leads to a restructuring of the nanoparticles towards a more three-dimensional shape. In the course of the heating, the Pt atoms at the edges of the clusters

are replaced by Pd atoms, while the facets are dominated by Pt; overall, the fraction of Pt at the surface increases. The first heating cycle after exposure to CO at low temperature leads not only to a restructuring but also to a stabilization of the nanoclusters. This is concluded from the fact that repeated CO adsorption and desorption cycles cause no further changes. Interestingly, however, dynamic changes occur during TPXPS or when applying a CO or O_2-stream using a supersonic molecular beam at constant temperatures. Up to 340 K, CO molecules rearrange from facet to edge sites. Starting above 360 K, Pt edges are formed again. They only exist at elevated temperatures in the presence of CO, as they disappear, when the system cools down in vacuum.

5   Platinum Nanocluster Arrays on *h*-BN/Rh(111)

In the previous chapters, metal nanoclusters on graphene/Rh(111) were the matter of interest. While these are intriguing model systems for the researched processes, they have one downside: The huge graphene signal produces a background that makes investigations on processes that involve aliphatic, aromatic, olefinic, or carbidic carbon challenging. Changing the support to *h*-BN/Rh(111) avoids this strong C 1s signal and its background and makes such measurements easily accessible. Another advantage of *h*-BN is its stronger binding to the Rh crystal compared to graphene. This leads to a higher cluster stability and can avoid intercalation.[110] In this chapter, three examples of how to utilize the Pt/*h*-BN/Rh(111) system will be given: Chapter 5.1 will introduce the basics and deal with the Pt nanoclusters on the *h*-BN/Rh(111) support in a size-selective manner over the range from one to fifty atoms per clusters. In Chapter 5.2, the decomposition reaction of ethylene will be presented as well as the influence of carbon residues on this process. Finally, in Chapter 5.3, the Pt nanoclusters will be utilized as a template to grow a graphene/Pt/*h*-BN van der Waals heterostructure.

5.1 Growth and Stability of Pt Nanoclusters on *h*-BN/Rh(111) from 1 to 50 atoms [P5]

In this chapter, the basics of growing Pt nanoclusters on *h*-BN/Rh(111) and annealing effects are investigated by a combination of STM and HR-XPS studies. In Figure 5.1, the STM images and Pt $4f_{7/2}$ XP-spectra of Pt nanocluster arrays on *h*-BN/Rh(111) are shown for coverages of a) $\theta_{Pt} =$ 0.005, b) 0.09, and c) 0.42 ML, after deposition at 295 K. By accounting for the size of the Moiré unit cell, these coverages can be translated to an average number of atoms per unit cell. Dividing by the number of filled pores leads to the number of atoms per cluster, namely 2.3, 12, and 55 atoms, respectively. For the low Pt coverages in Figure 5.1a, the structure of the *h*-BN Moiré is still visible. Here, about 27% of the *h*-BN pores are filled with Pt clusters, which appear as light protrusions within the pores. As the apparent size of the clusters varies, and the average number of atoms per cluster is very low (2.3 atoms), this number also includes single atoms. Single atoms of Pd, Mn, and Co on *h*-BN have already been investigated in STM, but mostly at low temperature.[111,112] Notably,

at RT, no Pt atoms or clusters hop from one pore to another, at least within the timescale of data acquisition (1-2 min per image). This behavior is attributed to the high diffusion barrier of 1.23 eV for single Pt atoms between different pores on *h*-BN, which was determined by density functional theory (DFT) calculations.[68] However, the diffusion barriers within the pores seem to be lower than the one between the pores, as some of the Pt clusters move, as seen in STM videos.
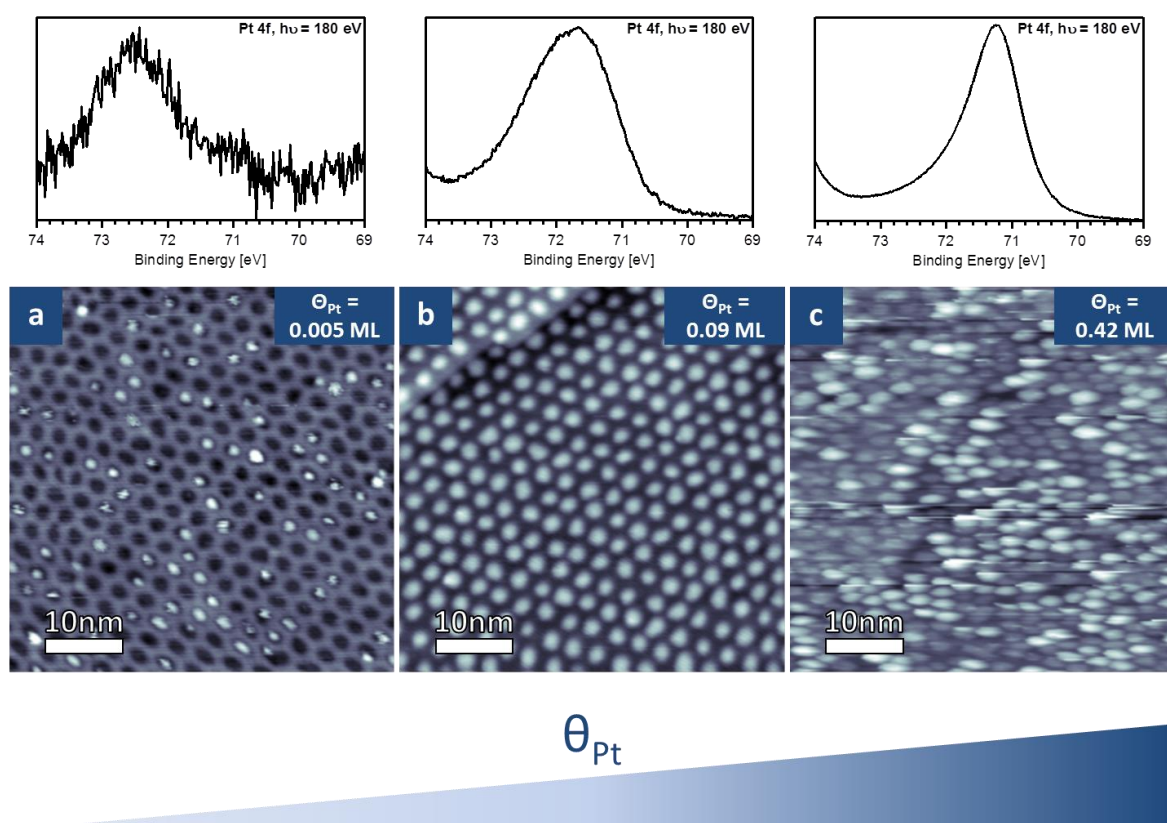
Figure 5.1: STM images of Pt nanocluster on *h*-BN∕Rh(111) with different Pt coverages at 295 K and corresponding Pt 4f$_{7/2}$ XP-spectra. At low coverage a) empty pores and small clusters coexist, b) around 0.1 ML equally appearing filled pores are observed and c) at higher coverages smaller and larger clusters are present. Θ_{Pt} = a) 0.005, b) 0.09, c) 0.42 ML; U = a) -1.0, b) 1.5, c) 1.2 V; I = 1.0 nA. hν = 180 eV.

To further characterize the Pt/*h*-BN/Rh(111) system by HR-XPS at 150 K a Pt wedge was deposited, *i.e.*, a Pt deposit with a linear coverage gradient on a 1 cm large *h*-BN/Rh(111) sample in one single deposition step. Fits to selected N 1s and B 1s spectra are shown in Figure 5.2a and 5.2b, respectively. Without Pt (bottom spectra), the two well-known peaks of pristine *h*-BN are clearly visible in the N 1s and B 1s spectra.[59] They are attributed to *h*-BN in the pores (red; N 1s: 398.81 eV, B 1s: 190.72 eV) and on the wires of the nanomesh (blue; N 1s: 398.16 eV, B 1s: 190.36 eV). Increasing the Pt coverage results in a decrease in intensity of both N 1s and B 1s peaks

at higher XPS binding energies, *i.e.*, the pore species, and for higher coverages an overall shift of all features towards lower binding energies. To fit the corresponding spectra for Pt covered *h*-BN, a new, third peak (green in Figure 5.2) is added at 398.62 eV in the N 1s region and 190.54 eV in the B 1s region (best seen for 0.019 ML Pt). This new peak is assigned to *h*-BN pores of the nanomesh that contain Pt. In Figure 5.2, representative fits for three different Pt coverages in the low coverage regime (up to 0.094 ML) are shown with an assignment of the different peaks to the different *h*-BN species. The peak of the pore filled with Pt already arises at coverages as low as 0.0014 ML, where part of the *h*-BN pores are filled, but on average only with one single atom. Notably, it has been demonstrated that even single atoms can alter the electronics of a whole pore of the *h*-BN/Rh(111) nanomesh, in this example lowering the *h*-BN-substrate bond strength of all BN units in the pore.[112] In the Pt $4f_{7/2}$ (Figure 5.2c), the Pt atoms of the "surface" (green) and the "bulk" (blue) layer of the clusters can be distinguished. The center of gravity of the peak shifts from 72.54 eV at the lowest Pt coverage of 0.0009 ML to 71.25 eV at the highest Pt coverage of 0.334 ML. Thereby, the change in binding energy is most pronounced for the low Pt coverages and saturates at higher coverages at about 71.22 eV. A similar size-dependent shift to lower binding energies for larger clusters was also reported for the Au/*h*-BN/Rh(111) system.[72] The shift in binding energy goes along with a decrease of the FWHM from ~3 eV to 1.03 eV with increasing Pt coverage. This indicates that in small clusters the Pt atoms have different chemical environments, whereas in large clusters one (or only few) species is dominant.

When doing a quantitative analysis of the XP-spectra recorded for different Pt coverages after deposition at 150 K and after annealing at elevated temperatures it shows that the number of empty pores decreases continuously with increasing Pt coverage up to 0.094 ML at 150 K. Simultaneously, the number of pores containing Pt increases. At a Pt coverage of 0.094 ML, all pores of the nanomesh are filled with Pt, resulting in an average amount of ~12 Pt atoms per pore. This coverage matches the results from the corresponding STM experiments (here θ_{Pt} = 0.09 ML, see Figure 5.1b). After heating to 400 K, the XP-spectra in both the N 1s and the B 1s region do not display significant changes compared to the freshly prepared system at 150 K in the complete coverage range from 0 to 0.33 ML Pt. STM confirms these findings: no significant changes are observed between the STM images of 0.094 ML Pt deposited at 160 K with the corresponding images recorded after the sample was held at RT for 16 h and annealed at 400 K for 80 min. Therefore, the nanoclusters are thermally stable up to 400 K. However, these results contradict a

Poisson distribution of the Pt atoms in the pores, which means that a diffusion process even at 150 K has to take place after impact of the atoms that results in their clustering.
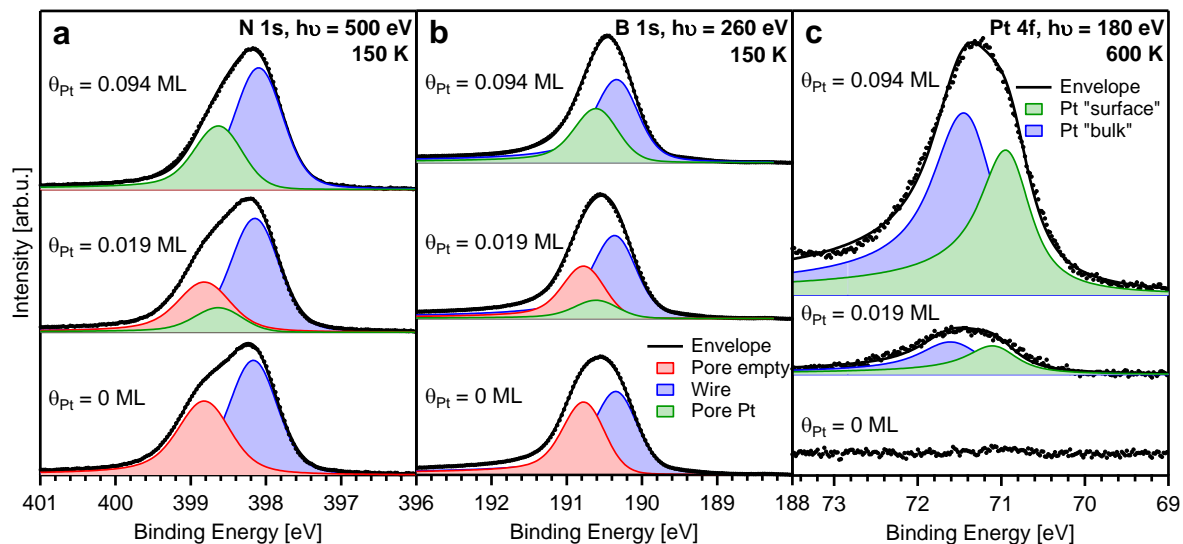

Figure 5.2: Selected fits of XP-spectra of Pt nanocluster arrays on *h*-BN∕Rh(111) for θ_{Pt} = 0, 0.019, and 0.094 ML. The N 1s and B 1s spectra were measured after evaporation at 150 K without any further treatment of the sample, the Pt 4f spectra after heating to 600 K to remove residues from the evaporation process: a) N 1s, b) B 1s, c) Pt 4f$_{7/2}$.

The situation changes after annealing to 500 K. The number of Pt clusters decreases, some clusters appear brighter in STM, and the *h*-BN background becomes visible. This trend continues at even higher temperatures. In the XPS studies, the changes are less pronounced at comparable temperatures, probably due to the significant shorter annealing times. Even after heating to 600 K, the number of Pt clusters remains nearly constant for Pt coverages below 0.20 ML. Only for Pt coverages beyond 0.20 ML, the number of empty pores increases. We suppose that at this temperature some of the larger Pt nanoclusters grow at the cost of smaller ones, resulting in an overall decrease in the number of clusters and the appearance of empty pores. This process occurs more frequently with rising Pt coverage, whereas low cluster densities and small clusters suppress the effect. After annealing at 800 K, the number of empty pores increases at all coverages, indicating a lower number of (larger) clusters. This decrease in the number of Pt clusters is caused by Ostwald ripening, similar to what is observed for Pd.[110] Nevertheless, for lower Pt coverages, the number of empty pores is still lower than for higher coverages with a minimum at about 0.15 ML. This means that the ripening process is slower in the low Pt coverage regime. After annealing at 1000 K, all of the Pt nanoclusters have coalesced resulting in a small number of large Pt particles. Due to the

strong damping of the large particles, no signal attributed to pore species filled with Pt is observed in the N 1s and B 1s region.

The corresponding Pt $4f_{7/2}$ spectra (not shown) reveal an overall decrease in Pt $4f_{7/2}$ binding energies when annealed. For small coverages, the effect is even stronger. Thus, finally, the Pt $4f_{7/2}$ peak positions for all coverages align at 70.98 eV after heating to 1000 K. This means, that all the Pt nanoparticles have nearly the same three-dimensional like structure, with only their number depending on the coverage. This fits the observation in the N 1s and B 1s regions that suggest a low number of huge clusters after annealing to 1000 K, as the signal of the occupied pores vanishes due to damping by the clusters inside them.

This section demonstrated that HR-XPS offers a possibility to distinguish empty and filled pores of Pt nanoclusters entrapped in the Moiré pattern of *h*-BN/Rh(111). In combination with STM, the ratio between empty and filled pores was studied as a function of coverage and temperature. Towards this goal, a Pt-wedge was prepared, where a steady gradient in the Pt-coverage is created across several mm of the Rh single crystal. At 0.1 ML, the clusters appear remarkable uniform in STM, and there are no more empty pores. At coverages below 0.1 ML an unexpected growth mechanism is found where the cluster size distribution cannot be explained by a Poisson distribution. Instead, there are less but larger clusters entrapped in the *h*-BN nanomesh than expected by statistics. This gives evidence for some mobility of the Pt atoms immediately after evaporation, *i.e.*, a hot precursor is involved in the cluster growth. An active ripening process was not observed at RT. Instead, the Pt clusters are stable up to around 400 K for up to hours. Above 400 K the clusters undergo Ostwald Ripening, though there is an enhanced resistance against ripening for Pt coverages below 0.2 ML. The findings reveal that the coverage regime between 0.1 and 0.2 ML of Pt on *h*-BN/Rh(111) features attractively defined conditions and could serve as a model system that advances one step further into the materials gap between model catalysis and real catalysts.

5.2 Ethylene: Its adsorption, reaction, and coking on Pt/*h*-BN/Rh(111) nanocluster arrays [P6]

All catalyzed reactions that involve hydrocarbons suffer from catalyst deactivation by coking, *i.e.*, carbon accumulates on the catalyst surface and reduces the activity of the catalyst.[5,113] This makes, often costly, catalyst regeneration necessary. Therefore, the prevention or at least reduction of coking is an important topic for the abundant number of processes that have ethylene involved as product[114–116] or educt.[117] Besides the negative effect of catalyst deactivation, controlled coking can have positive effects like preventing cracking in dehydrogenation reactions.[118,119] Several species were identified in literature to be involved in the ethylene decomposition: Starting from π-bonded C_2H_4 below 52 K,[120] different C_2H_y species, like σ-bonded C_2H_4, $CHCH_3$ (ethylidene), and $CHCH_2$ (vinyl), have been suggested, especially at low temperatures. On all systems, ethylidyne (CCH_3) was identified as the main intermediate at room temperature (RT). CCH_3 is also the most stable species at low temperature.[121] However, on [100]-like surfaces, acetylene, and vinylidene were found in addition.[122,123]

The fitted spectra of ethylene-saturated Pt(111), Pt(355), and Pt nanoparticles are presented in Figure 5.4. On Pt(111) (Figure 5.4a), the adiabatic ethylene peak is located at 283.16 eV with two vibrational excitations that come with a difference of 350 meV at higher binding energy and an S-factor of 0.36.[124] On the stepped Pt(355) single crystal (Figure 5.4b), two carbon species are found, with the adiabatic signals at 283.21 and 283.62 eV. By comparison with flat Pt(111), the one at 283.21 eV is assigned to ethylene adsorbed on the flat [111]-terraces of the Pt(355) crystal. The signal at 283.62 eV is attributed to ethylene molecules bound to the [111]-like step sites of the Pt(355) crystal. Analogous, on the nanocluster arrays (Figure 5.4c), the signal at 283.35 eV belongs to ethylene adsorbed on the facets and the one at 283.86 eV to ethylene on the edges. At saturation, 63% C_2H_4 at facets and 37% C_2H_4 at edges are found at on the particles. The binding energies on the nanoclusters are shifted to higher binding energies, which is attributed to the limited number of valence electrons in the small nanoclusters compared to single crystals and to the electronic influence of the *h*-BN support. The fraction of edge adsorption sites for C_2H_4 on the nanoparticles of 37% is slightly higher than the fraction of step adsorption sites of 25% on Pt(355). All mentioned ethylene-species are σ-bonded to two on-top sites, as π-bonded C_2H_4 only exists below 52 K on Pt.[120] On both, nanoclusters and the stepped surface, both ethylene species grow with a 1:1 ratio

until saturation of the step/edge species, after which only the terrace/facet species continues to grow. From this, the saturation coverage of 0.22 ML, and the 1:3 step to terrace end ratio on Pt(355), it is concluded that ethylene adsorbs with a geometry that consists of stripes of two molecules at a 60° angle with respect to the steps. Thereby, ethylene occupies first the mixed step and terrace binding sites and then the pure terrace sites, yielding a structure very similar to the (2x2) structure of ethylene on Pt(111).[125] The proposed structure is shown in Figure 5.3.
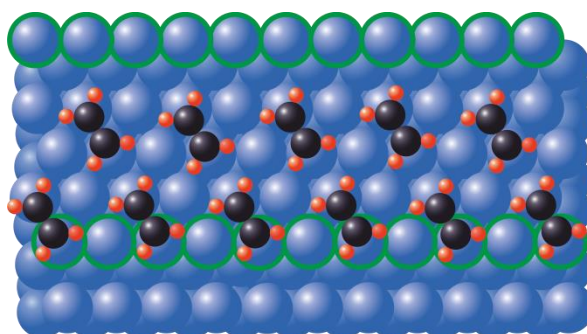

Figure 5.3: Scheme of the adsorption structure of ethylene on Pt(355). The step atoms are marked with a green rim.

Two representative spectra measured during the annealing of ethylene-saturated nanoclusters are presented with their fits in Figure 5.4f and 5.4h. Three reaction phases can be distinguished during the heating. The first sets in at 250 until 332 K, when three new species are formed at the cost of both ethylene species. Their adiabatic peaks are found at 284.30, 284.09, and 283.64 eV. While the first two both have their first vibrational excitation at 450 meV higher binding energies and an S-factor of 0.21, the vibration-splitting of the signal at 283.64 eV is 420 meV, and the S-factor is 0.16. These three species are also found in the same temperature range on Pt(355) (Figure 5.4e), yet at slightly lower binding energies at 284.19, 284.01, and 283.64 eV and with a different ratio, the latter due to a different density of step sites. Therefore, the peak at 284.30 eV is assigned as ethylidyne at facet sites (corresponding to $CCH_3^{terrace}$ at 284.19 eV) and the one at 284.09 eV as CCH_3 bound to edge sites of the nanoparticles (corresponding to CCH_3^{step} at 284.01 eV).[124] While the formation of ethylidyne-species is expected from the results on Pt(111), the peak at 283.64 eV is not. From the analysis of the vibrational fine structure, it is concluded that it is vinylidene (CCH_2), a known intermediate on (100)-surfaces.[122,126] Additionally, DFT calculations showed that on stepped Pt crystals the formation of CCH_2 becomes as likely as the formation of CCH_3 with ethylene as educt.[127] CCH_3^{facet} starts to decrease at 363 K until it is completely gone at 490 K. In comparison, the amount of CCH_3^{egde} starts to decrease at 443 K until it is gone at 497 K. Together

with the onset of the decrease of CCH$_2$ at 412 K, a new species at 283.81 eV is formed, identified as CCH, also found on Pt(111).[124] It has a maximum at 474 K and vanishes at the same time as CCH$_2$ at 531 K. Above 451 K, elemental carbon forms as the final product of the ethylene reaction, detected as a broad signal, as it is a mixture of several species of C-atoms (see Figure 5.4g and h). After the reaction, partial desorption of ethylene leads to a decrease of the total amount of C by 38% from θ_C = 0.81 to 0.51 ML (not shown). On Pt(355), the same reaction pathway with the same intermediates occurs. Here, the CCH is found at 283.91 eV. The overall comparison of the Pt(355) and the Pt nanoclusters shows the similarity of the reaction on the [111]-steps and the cluster edge sites.

Furthermore, the ethylene/Pt nanocluster system was used as a model for coking. By a systematic approach of ethylene-adsorption and TPXPS, the amount of preadsorbed carbon was increased after every ethylene dehydrogenation reaction. The influence of the preadsorbed carbon was then investigated in the next ethylene adsorption/TPXPS cycle.
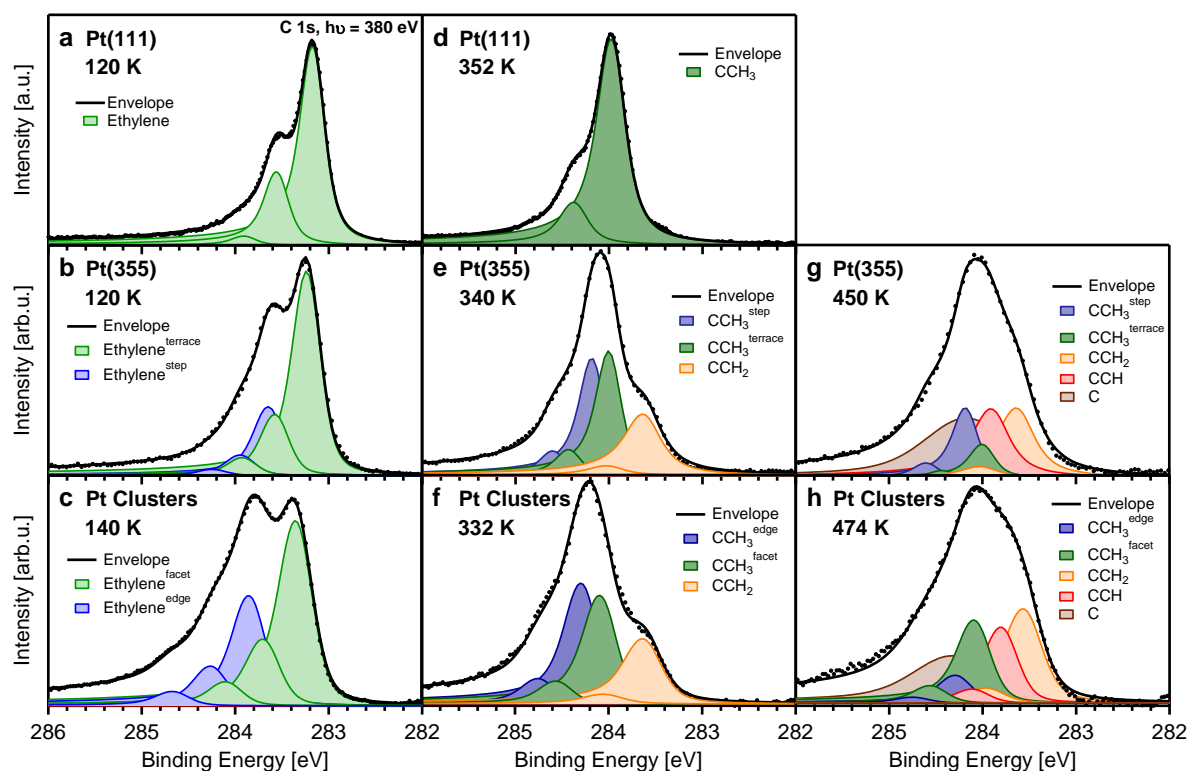

Figure 5.4: C 1s XP-spectra of saturated ethylene layers on different Pt surfaces and their corresponding fits at adsorption temperature a)-c) and during TPXPS d)-g): a), d) Pt(111); b), e), g) Pt(355); c), f), h) 0.7 ML Pt∕*h*-BN∕Rh(111) nanocluster arrays.

The C 1s spectra of ethylene-saturated Pt clusters are shown in Figure 5.5a for θ_C = 0, 0.51, and 0.79 ML. The denoted amounts of carbide were determined at 140 K. A comparison of the carbide-free and coked nanoclusters shows that carbon residues not only decrease the amount of ethylene that can be adsorbed but also change the adsorption behavior. The *in situ* measurements show that the adsorption rate on the edge sites is massively reduced compared to the facet sites, especially in the beginning. However, the difference in the final distribution between facet and edge species is less pronounced. The facet to edge ratio of ethylene of 63:37 for θ_C = 0 ML remains about the same with 68:32 for θ_C = 0.51 ML and 66:34 for θ_C = 0.79 ML. Extrapolation of the blocking leads to a complete suppression for $C_2H_4^{edge}$ at θ_C = 1.30 ML and $C_2H_4^{facet}$ at θ_C = 1.52 ML (Figure 5.6b). As the carbide should preferentially form at and bind to the edge sites, the roughly constant ratio of ethylene at edges and facets comes with surprise. However, this observation is probably an artifact from the conduct of the experiment, as CO adsorption/desorption experiments were performed between the ethylene cycles. It is known that CO displaces other adsorbates from the edges at elevated temperature what explains the observations.[76]

Also, the thermal reaction of ethylene is changed by the carbon-residues, as the reaction mechanism changes. The amounts of the intermediates CCH_2 and CCH are remarkably decreased. DFT showed that the formation of CCH_2 is strongly connected to the presence of step sites,[127] already small amounts of carbon there should influence this barrier. For θ_C = 0.79 ML, CCH_2 and CCH are no longer observed.
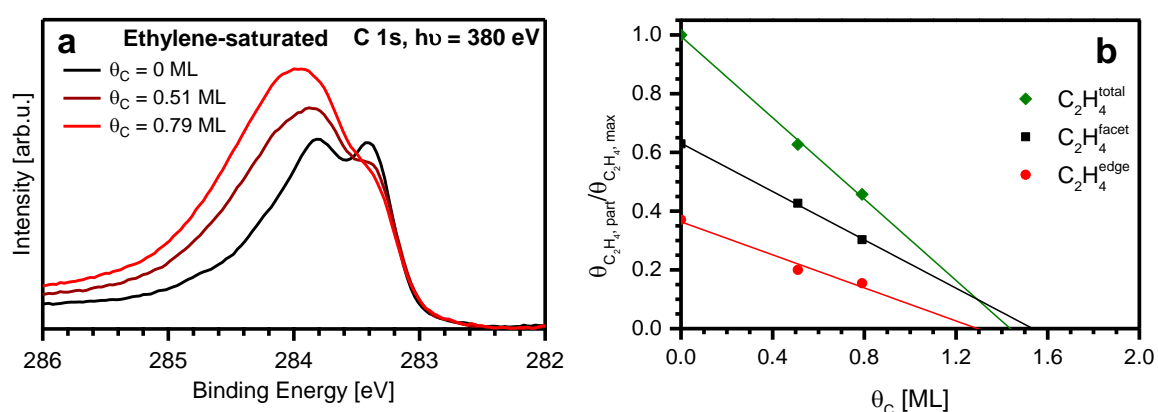

Figure 5.5: a) C 1s XP-spectra and b) saturation coverages of ethylene on 0.7 ML Pt∕*h*-BN∕Rh(111) nanocluster arrays for different amounts of preadsorbed carbon to illustrate the site-blocking by carbon. C_2H_4 was adsorbed and measured at 140 K.

In summary, the adsorption and decomposition of ethylene on clean and carbon pre-covered Pt nanocluster arrays on the *h*-BN/Rh(111) nanomesh were investigated and compared to the results on a flat Pt(111) and a stepped Pt(355) surface. While on Pt(111), the reaction is straightforward with CCH_3 and CCH as observed intermediates, on Pt(355) and Pt nanoclusters, an additional CCH_3 species bound to the edge/step sites is found, and a new reaction path opens with CCH_2 as stable intermediate. Thereby, Pt(355) and Pt nanoclusters were remarkably similar and only differed in the ratio of the intermediates. Carbon pre-covered clusters simulate coked catalysts. The maximal ethylene coverage decreases linearly with the amount of preadsorbed carbon. Thereby, the edges are more affected than the facets and already small amounts of carbon suppress the new reaction path via CCH_2 effectively. This fits to the predictions of DFT calculations that show the importance of edge sites for this pathway.[127]

5.3 Nano-heterostructures: Pt Nanoclusters between *h*-BN and Nanographene [P7]

In this section, a new synthesis route for nanographene will be presented, using Pt nanocluster arrays on *h*-BN/Rh(111) as template. Until now, it can only be prepared using synthetic organic chemistry, where atomically precise methods are available.[128] Nanographene is of high interest due to its nonbonding π-states at the edges of the nanosheets.[129] Its growth on the nanoclusters is also a way to produce graphene/Pt/*h*-BN heterostacks, see Figure 5.6. The unique properties of 2D materials along with the huge number of possible combinations allow for the discovery and investigation of a variety of physical phenomena. In order to build van der Waals heterostructures, combinations of *h*-BN, graphene and transition metal dichalcogenides like MoS_2 are frequently studied.[26] Thereby, *h*-BN is considered as the ideal insulating and chemical non-interacting substrate, while graphene is a conductor and dichalcogenides are semiconductors.
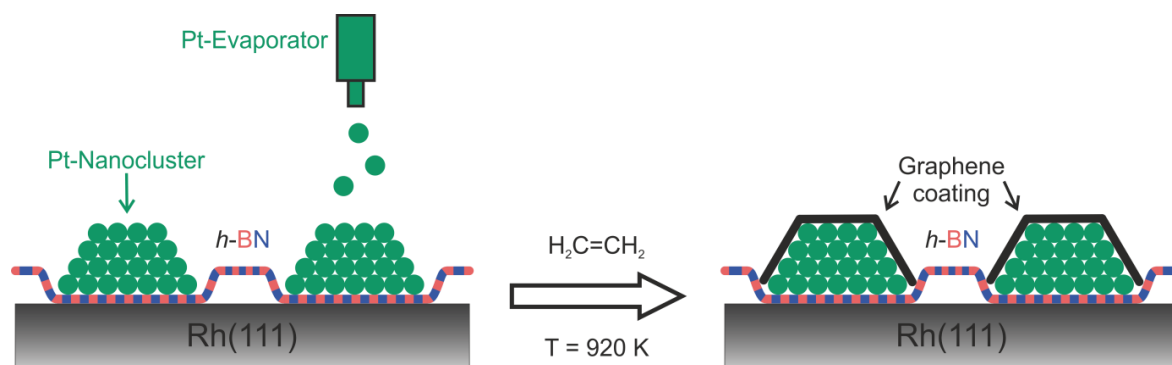
Figure 5.6: Scheme of the preparation process of a graphene/Pt/*h*-BN nano-heterostructure on Rh(111).

After deposition of 0.81 ML Pt at 150 K, the sample was exposed to CO until saturation and then heated to 550 K.[23] By this procedure, the nanoparticles containing, on average 108 atoms become more three-dimensional-shaped and more robust towards ripening processes in follow-up experiments. The average cluster size is calculated from the Pt coverage and the pore size, under the premise of a Poisson distribution during the evaporation process.[20] To be able to distinguish purely temperature-induced changes of the nanoclusters like ripening from the changes caused by the growth of graphene, the sample was annealed to the growth temperature of graphene, that is, 920 K. This leads to the formation of larger clusters, causing a slight damping of the Pt signal; at the same time, the clusters occupy a smaller surface area, leading to larger substrate signals. Heating to 920 K leads to about half the pores containing a Pt nanocluster. This is due to ripening that results in an average cluster size of 216 atoms. The argument is further supported by the decrease of surface areas of the clusters.

To grow graphene and encapsulate the nanoparticles, the Pt nanocluster array was exposed to 2.5 x 10^{-8} mbar ethylene at 920 K. The resulting C 1s spectra measured *in situ* during the growth process at 920 K are presented in Figure 5.7a; a fitted spectrum, measured after the end of the experiment, at a temperature below 200 K is shown in Figure 5.7b, along with the quantitative analysis as inset. The carbon signal initially starts to grow at 284.08 eV but quickly shifts to a binding energy of 284.25 eV. This behavior is attributed to the initial formation of disordered C atoms until the first graphene flakes are formed, which then grow further to form closed graphene layers on the Pt nanoclusters. Right from the beginning of the experiment, a small shoulder at 283.61 eV develops and stays at a low level of ~2% of the total signal. This signal is assigned to carbide, which inevitably forms during graphene growth by chemical vapor deposition. For graphene growth on Pt(111), it vanishes into the bulk during further growth.[54] However, as the nanoclusters are only a few layers

high, the carbide always remains in the detection volume of XPS. Saturation of the graphene signal occurs above ~21 L ethylene exposure, at a carbon coverage of 0.56 ML. The graphene growth process is self-limiting after the formation of one monolayer on Pt.[130] The fact that graphene growth saturates at 0.56 ML, while one graphene layer on Rh(111) has 2.38 ML C, shows that graphene grows only on the catalytically active Pt nanoparticles, but not on the *h*-BN. This also indicates that with the growth parameters used here, the Pt nanoclusters cannot be used as catalyst or nuclei to form a macroscopically extended graphene layer on top of the Pt/*h*-BN system. The fitted spectrum in Figure 5.7b was measured below 200 K to avoid thermal broadening, as observed in the *in situ* measurements at 920 K. The fit results in a binding energy of 284.25 eV with a FWHM of 0.51 eV.

The C 1s binding energy of 284.25 eV for graphene on the Pt nanoclusters resembles the literature value for graphene on Pt(111).[53] Yet, the FWHM of 0.51 eV is larger than the value of 0.35 eV in literature. We attribute this to the fact that the Pt clusters exhibit non-uniform sites such as steps, edges, and kinks, which are expected to yield slightly different C 1s binding energies. In addition, the grown nanographene should contain a number of five-membered rings in order to compensate for the curvature of the nanoparticles, similar to fullerenes. Furthermore, the C atoms at the rim interact with the B and N atoms of the *h*-BN. Binding energy shifts caused by the interaction of C with B and N atoms were reported for graphene nanoflakes embedded in *h*-BCN/Ir(111).[131] The combination of these effects broadens the C 1s peak.
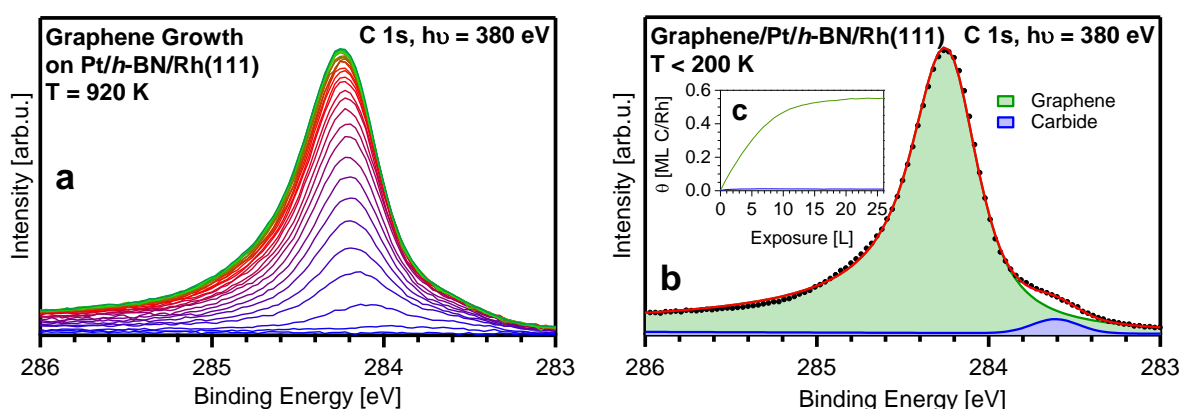
**Figure 5.7:** a) *In situ* XP-spectra of the growth of graphene on 0.81 ML Pt nanocluster arrays on *h*-BN⁄Rh(111) measured in the C 1s core-level with an excitation energy of 380 eV. Ethylene was dosed with a pressure of 2.5 x 10⁻⁸ mbar at a temperature of 920 K for 30 min until saturation. b) Fitted C 1s XP-spectrum of the saturated system after cooling below 200 K. c) Quantitative analysis of the spectra shown in a).

The graphene layer on the Pt nanoclusters was further characterized by NEXAFS at the C K-edge (see Figure 5.8). Monolayer graphene on Pt shows a distinct set of four peaks, at 285.7 (A) and 284.4 eV (A') at gracing incidence (GI) and 292 (B) and 293 eV (C) at normal incidence (NI).[53,130] Peak A is assigned to excitation to the $\pi^\star$-orbital, and peaks B and C to excitations to the $\sigma_1^\star$-and $\sigma_2^\star$-orbitals, respectively. These three peaks are also found for highly-ordered pyrolytic graphene (HOPG) at the same photon energies.[132] The fourth peak/shoulder, A', found on graphene on Pt at 284.4 eV[53,130] has been assigned to a lowering of the Fermi level due to charge transfer and weak orbital mixing with the substrate. In the NEXAFS measurements on the graphene/Pt/*h*-BN heterostructure, shown in Figure 5.8, the same set of four features at the same photon energies as found for graphene on Pt(111) is observed. Notably, the spectra show only a very weak dependence on the incidence angle, attributed to the three-dimensional shape, that is, the curvature of the nanographene, which is wrapped around the nanoparticle. Thereby, many geometries coexist, averaging out the angle-dependent features.[130] This observation gives further strong evidence that the Pt nanoclusters on *h*-BN/Rh(111) are completely covered with a graphene layer.
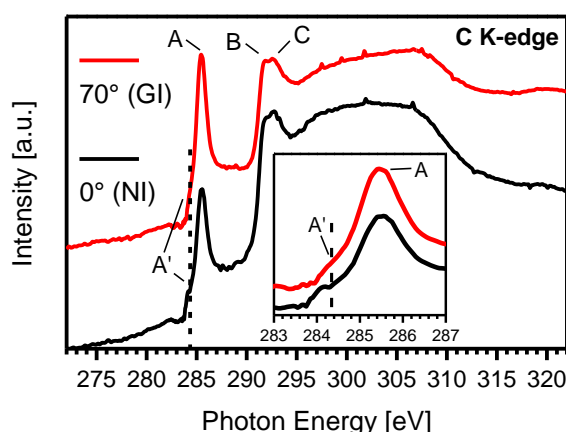
Figure 5.8: Partial yield NEXAFS of graphene/Pt/*h*-BN/Rh(111) measured at incidence angles normal to the surface (0°, Normal Incident, black) and at 70° vs. the surface normal (Gracing Incident, red) for the C K-edge. The inset shows a zoom of the pre-edge feature. The synchrotron light was linear horizontally polarized.

To test the quality of the graphene encapsulation, the graphene-covered clusters were exposed at 150 K to a CO-stream from a supersonic molecular beam, corresponding to a CO pressure of 7.4 x 10^{-7} mbar. CO is known to strongly bind to Pt.[133] Notably, there are no CO-induced changes in the C 1s XP-spectra measured *in situ* at the elevated pressure and in the Pt 4f spectra measured *ex situ*. Especially, the Pt 4f signal is very sensitive towards CO, and already traces are causing an observable surface-core-level-shift.[23] The absence of any CO-induced changes proves that the

graphene layer is impermeable, and that the Pt nanoclusters are completely encapsulated with graphene on top and *h*-BN at the bottom.

In conclusion, van der Waals nano-heterostacks of *h*-BN/metal/graphene were formed. Such heterostacks are a promising building block for nanoelectronics, nanomagnets, or similar applications. At the same time, this opens a new route to synthesize nanographene under UHV conditions. Well-ordered, supported Pt nanoparticles on *h*-BN/Rh(111) were used as a seeds for graphene growth. Therefore, 2.5 x 10^{-8} mbar ethylene were adsorbed at 920 K. The growth was followed *in situ* with high-resolution synchrotron XPS, and the expected formation was reached. The nanographene layers were further characterized by NEXAFS and were shown to be impermeable to CO. As the nanographene grows only on the Pt nanoparticles, its size is determined by the size of the clusters.

6   Summary

The aim of this thesis was the investigation of metal nanocluster arrays supported on lattice-mismatched two-dimensional materials that work as chemically innocent templates. Thereby, a special focus was set to use these nanoclusters as model system for catalysts and catalyst deactivation. Synchrotron-based high-resolution XPS and NEXAFS were utilized to achieve this.

The influence of sulfur on the adsorption and desorption behavior of CO on graphene-supported palladium and platinum nanoparticles was investigated as model for catalyst poisoning. On Pd nanoclusters, sulfur adsorbs at highly coordinated sites and blocks these sites for CO. Other adsorption sites are blocked to a minor degree. As the desorption temperatures of CO are independent of the sulfur amount, the Pd-CO bond-strength seems not be affected by sulfur. Thus, blocking of adsorption sites on Pd by sulfur happens via steric hindrance, while electronic effects seem not to play a role. The degree of site-blocking is in between that of Pd(111) and Pd(100) surfaces, which indicates that the nanocluster surface consists of a mixture of (111) and (100) facets. Interestingly, coadsorbed CO has an influence on the preadsorbed sulfur. There are indications of a displacement of S atoms such that S pairs are formed on the surface, creating more space to adsorb CO on the nanoparticles. On Pt nanoclusters, both sulfur and CO prefer the adsorption at edge sites over facets. Thus, a strong blocking effect for CO on edges was observed with a total blocking of edges at $\theta_S = 0.12$ ML. On facets, on-top sites are blocked already by small amounts of sulfur, while bridge sites are not affected until $\theta_S = 0.08$ ML. At higher coverages, also a strong blocking effect of bridge sites sets in. Estimated 0.28 ML S block all sites for CO. Upon heating, first, a site exchange of CO and S occurs where CO displaces S from the edges to facets, with the maximum CO coverage at edges reached at 330 K. This effect is more pronounced for small sulfur coverages. At higher temperature, the desorption of CO enables sulfur to diffuse back to the edges. While the overall desorption behavior is not influenced by sulfur, a reduction of the desorption temperature was found for CO bound to edge sites of the Pt nanoclusters. Concluding from this, the poisoning effect of sulfur works primary by blocking of sites, especially edge sites, while electronic effects play a minor role.

The oxidation of sulfur on Pt nanoclusters at temperatures between 350 and 430 K was studied as a way of catalyst reactivation. SO_4 was identified as the final oxidation product, with SO_3 being the only observable intermediate, that is, SO and SO_2 react very fast to the next oxidation step and that

the first reaction step that is from S to SO is rate determining. During the adsorption of oxygen, a displacement of sulfur from the edges to the facets by oxygen is observed. In contrast to Pt(111) and stepped Pt(355), the reaction kinetics cannot be described by simple pseudo-first order behavior.

The influence of CO on PdPt alloy nanocluster arrays supported on the graphene-Moiré on Rh(111) was investigated. Annealing of the as-prepared nanoclusters to 550 K after exposure to CO leads to a restructuring of the nanoparticles towards a more three-dimensional shape. In the course of the heating, the Pt atoms at the edges of the clusters are replaced by Pd atoms, while the facets are dominated by Pt; overall, the fraction of Pt at the surface increases. The first heating cycle after exposure to CO at low temperature leads not only to a restructuring but also to a stabilization of the nanoclusters. This is concluded from the fact that repeated CO adsorption and desorption cycles cause no further changes. Interestingly, there are, however, dynamic changes during TPXPS or when applying a CO- or O_2-stream using a supersonic molecular beam at elevated temperatures. Up to 340 K, CO molecules rearrange from terrace to edge sites. Starting above 360 K, Pt edges are formed again. Yet, they only exist at elevated temperatures in the presence of CO, as they disappear, when the system is cooled down in vacuum.

h-BN/Rh(111) was used as an alternative substrate to graphene/Rh(111) without the large carbon background. HR-XPS offers a possibility to distinguish empty and filled pores of Pt nanoclusters entrapped in the nanomesh. In combination with STM, the ratio between empty and filled pores was studied as a function of coverage and temperature. Therefore, a steady gradient in the Pt-coverage was created across several mm of the Rh single crystal. At 0.1 ML, the clusters appear remarkably uniform in STM and there are no more empty pores. The nucleation regime at coverages below 0.1 ML exhibits an unexpected growth mechanism where the cluster size distribution cannot be explained by a Poisson distribution. Instead, less but larger clusters are entrapped in the h-BN nanomesh than expected by statistics. This gives evidence for some mobility of the Pt atoms immediately after evaporation, also called hot precursor effect. Yet, an active ripening process was not observed at RT. Instead, the Pt clusters are stable up to around 400 K for up to hours. Above 400 K, the clusters undergo Ostwald Ripening, though there is an enhanced resistance against ripening for Pt coverages below 0.2 ML.

The adsorption and decomposition of ethylene on clean and carbon pre-covered Pt nanocluster arrays on h-BN/Rh(111) was investigated. The results were compared with that on a flat Pt(111) and a stepped Pt(355) surface. While on Pt(111), there is only one reaction pathway via CCH_3 and

CCH, on Pt(355) and Pt nanoclusters, an additional CCH_3 species bound to the edge/step sites and a new reaction path via CCH_2 are observed. Thereby, the reaction pathway and the reaction intermediates on Pt(355) and Pt nanoclusters were remarkably similar and only differ in the ratio of the intermediates. The measurements on carbon pre-covered clusters simulated coking of the Pt catalysts. The amount of ethylene that adsorbed decreased linearly with the carbon coverage. Thereby, the edges are more affected than the facets and already small amounts of carbon suppress the new reaction path via CCH_2 effectively.

The growth of van der Waals nano-heterostacks of *h*-BN/metal/graphene gives a promising building block for nanoelectronics, nanomagnets, or similar applications. Additionally, it opens a new route to synthesize nanographene under UHV conditions. Well-ordered, supported Pt nanoparticles on *h*-BN/Rh(111) were used as seeds for graphene growth through exposure to 2.5 x 10^{-8} mbar ethylene at 920 K. The growth was followed *in situ* with high-resolution synchrotron XPS. The nanographene layers were further characterized by NEXAFS and were shown to be impermeable to CO. As the nanographene grows only on the Pt nanoparticles and not on the *h*-BN regions in between, therefore, its size is determined by the size of the clusters.

In summary, the results suggest that supported nanoparticle arrays are an excellent model system because their well-defined conditions enable an atomic / molecular understanding of the adsorption, desorption, and reaction processes including their kinetics when using *in situ* methods such as synchrotron-based fast HR-XPS. The study further emphasizes the importance of steps/edges and defects for catalysis. Thereby, such nanocluster arrays advance one step further into the materials gap between model catalysis and real catalysts.

7   Zusammenfassung

Ziel dieser Arbeit war die Untersuchung geordneter Metallnanocluster, die auf gitterfehlangepassten zweidimensionalen Materialien geträgert wurden. Diese dienten als chemisch inaktive Template. Dabei lag der Fokus auf der Verwendung der Nanocluster als Modellsystem für Katalysatoren und deren Deaktivierung. Als Untersuchungsmethoden wurden synchrotronbasierte hochaufgelöste XPS und NEXAFS eingesetzt.

Der Einfluss von Schwefel auf die Adsorption und Desorption von CO auf graphengeträgerten Palladium- und Platinnanopartikeln fungierte als Modellsystem für Katalysatorvergiftung. Auf Pd-Nanoclustern adsorbiert Schwefel an hochkoordinerten Plätzen und blockiert diese für CO. Andere Adsorptionsplätze sind weniger betroffen. Da die CO-Desorptionstemperatur unabhängig von der Schwefelmenge ist, scheint Schwefel die Pd-CO-Bindungsstärke nicht zu beeinflussen. Dies spricht für die Blockierung der Adsorptionsplätze auf Pd durch sterische Hinderung, während elektronische Effekte keine Rolle zu spielen scheinen. Der Grad der Blockierung liegt dabei zwischen dem auf Pd(111)- und Pd(100)-Oberflächen, was zeigt, dass die Nanocluster aus einer Mischung von (111)- und (100)-Facetten bestehen. Umgekehrt beeinflusst koadsorbiertes CO auch den voradsorbierten Schwefel. Es gibt Anzeichen, dass sich Schwefelpaare auf der Oberfläche durch Verdrängung von Schwefelatomen bilden und so mehr Platz für CO auf den Nanopartikeln entsteht. Auf Pt-Nanoclustern bevorzugen sowohl Schwefel als auch CO die Adsorption auf Kantenplätzen gegenüber der auf Facettenplätzen. Deshalb wurde eine stärkere Blockierung der Kanten beobachtet. Für $\theta_S = 0.12$ ML ist diese vollständig. Auf den Facetten werden Top-Plätze bereits von geringen Schwefelmengen, blockiert, während Brückenplätze erst ab $\theta_S = 0.08$ ML betroffen sind. Bei höheren Bedeckung werden aber auch letztere stark blockiert. Etwa 0.28 ML S blockieren alle Plätze für CO. Beim Heizen tauschen zunächst CO und Schwefel die Plätze, wobei CO Schwefel von den Kanten auf die Facetten verdrängt. Dieser Effekt ist für kleine Schwefelbedeckungen stärker ausgeprägt und erreicht sein Maximum jeweils bei 330 K. Bei höheren Temperaturen ermöglicht die Desorption von CO es dem Schwefel zurück an die Kanten zu diffundieren. Während das allgemeine Desorptionsverhalten nicht durch Schwefel beeinflusst wird, bewirkt er eine Reduzierung der Desorptionstemperatur für CO an den Kanten der Pt-Nanoclustern. Das bedeutet, dass die Schwefelvergiftung hauptsächlich über die Blockierung von Plätzen, insbesondere an Kanten, funktioniert, während elektronische Effekte eine untergeordnete Rolle spielen.

Die Schwefeloxidation auf Pt-Nanoclustern stellt einen Weg zur Katalysatorreaktivierung dar. Für die untersuchten Temperaturen zwischen 350 und 430 K ist SO_3 das einzig beobachtete Intermediat, was bedeutet, dass SO und SO_2 sehr schnell zur nächsten Oxidationsstufe weiterreagieren, und dass der erste Reaktionsschritt von S nach SO geschwindigkeitsbestimmend ist. Letztlich bildet sich SO_4 als Endprodukt. Während der Sauerstoffadsorption verdrängt Sauerstoff den Schwefel von den Kanten auf die Facetten. Im Gegensatz zu Pt(111) und gestuftem Pt(355) kann die Reaktionskinetik nicht durch einfache pseudo-erste Ordnung beschrieben werden.

Weiter wurde der Einfluss von CO auf PdPt-Legieungsnanocluster geträgert auf dem Graphenmoiré auf Rh(111) erforscht. Heizen der frisch präparierten, CO-bedeckten Nanocluster auf 550 K führt zu ihrer Restrukturierung in eine dreidimensionalere Gestalt. Gleichzeitig ersetzen Pd-Atome sämtliche Pt-Atome an den Clusterkanten, während auf den Facetten Pt vorherrscht; insgesamt nimmt der Pt-Anteil der Oberfläche zu. Der erste Heizzyklus nach der CO-Adsorption bei niedriger Temperatur führt nicht nur zu besagter Restrukturierung, sondern auch zu einer Stabilisierung der Nanocluster, da wiederholte CO-Adsorptions- und Desorptionszyklen keine weiteren Änderungen verursachen. Interessanterweise gibt es jedoch dynamische Änderungen während einer Heizrampe oder bei Anlegen eines CO- oder O_2-Stroms aus einem Überschallmolekularstrahl bei erhöhten Temperaturen. Bis 340 K ordnen sich CO-Moleküle von Facetten- auf Kantenplätze um. Beginnend über 360 K bilden sich zudem wieder Pt-Kanten, die allerdings nur bei erhöhter Temperatur in der Gegenwart von CO existieren. Sie verschwinden, sobald das System im Ultrahochvakuum abkühlt.

h-BN/Rh(111) diente als alternatives Substrat zu Graphen/Rh(111) ohne großes Kohlenstoff-hintergrundsignal im XPS. Durch Kombination von HR-XPS und STM wurde das Verhältnis von leeren und mit Pt-Nanoclustern gefüllten Poren der Moiréstruktur von h-BN/Rh(111) als Funktion der Bedeckung untersucht. Dabei bietet auch HR-XPS eine Möglichkeit leere und gefüllte Poren zu unterscheiden. Hierzu wurde ein kontinuierlicher Gradient der Pt-Bedeckung über mehrere mm des Rh-Einkristalls aufgedampft. Bei einer nominellen Pt-Bedeckung von 0.1 ML erscheinen die Cluster im STM bemerkenswert einheitlich und es gibt keine leeren Poren mehr. Im Nukleationsbereich unter 0.1 ML zeigt sich ein unerwartetes Partikelwachstum, bei dem die Clustergrößenverteilung stark von einer Poissonverteilung abweicht. Stattdessen befinden sich weniger, dafür größere Cluster im h-BN-Nanonetz als erwartet. Dies weist auf eine gewisse

Mobilität der Pt-Atome unmittelbar nach dem Verdampfen – einen sogenannten „hot precursor" – hin. Die Pt-Cluster zeigen keine Reifung bei RT und sind bis etwa 400 K über Stunden stabil. Über 400 K unterliegen sie allerdings Ostwaldreifung, wobei Pt-Bedeckungen unter 0.2 ML eine erhöhte Resistenz gegen Reifung aufweisen.

Die Abwesenheit eines Kohlenstoffhintergrundsignals ermöglichte die Untersuchung der Adsorption und Zersetzung von Ethen auf sauberen und kohlenstoffbedeckten Pt-Nanoclustern auf h-BN/Rh(111). Die Ergebnisse wurden mit denen auf flachem Pt(111) und gestuftem Pt(355) Oberflächen verglichen. Während es auf Pt(111) nur einen Reaktionsweg über CCH_3 und CCH gibt, existiert auf Pt(355) und Pt-Nanoclustern eine zusätzliche CCH_3-Spezies, die an die Kanten/Stufen gebunden ist, sowie ein neuer Reaktionspfad über CCH_2. Dabei erwiesen sich Pt(355) und Pt-Nanocluster als bemerkenswert ähnlich und unterschieden sich nur im Verhältnis der Zwischenstufen. Die Messungen auf kohlenstoffbedeckten Clustern simulierten die Verkokung von Katalysatoren. Die adsorbierbare Ethenmenge nimmt linear mit der Kohlenstoffbedeckung ab. Hierbei sind die Kanten stärker betroffen als die Facetten und bereits kleine Kohlenstoffmengen unterdrücken effektiv den neuen Reaktionsweg über CCH_2.

Das Wachstum von van-der-Waals-Nanoheterostapeln aus h-BN/Metall/Graphen stellt einen vielversprechenden Baustein für Nanoelektronik, Nanomagnete oder ähnliche Anwendungen dar. Zusätzlich eröffnet es einen neuen Syntheseweg für Nanographen unter UHV-Bedingungen. Geordnete, auf h-BN geträgerte Pt-Nanopartikel dienten als Wachstumskeime für Graphen bei einem Ethendruck von $2{,}5 \times 10^{-8}$ mbar und 920 K. Sein Wachstum wurde *in situ* mit HR-XPS verfolgt. Die Nanographenlagen wurden weiter mit NEXAFS charakterisiert und erwiesen sich als undurchlässig für CO. Da das Nanographen nur auf den Pt-Nanopartikeln und nicht auf dem dazwischenliegendem h-BN wächst, wird seine Größe von der Clustergröße bestimmt.

Zusammenfassend ergeben die Resultate, dass geordnete, geträgerte Nanopartikel ein exzellentes Modellsystem darstellen, da ihre wohldefinierten Eigenschaften ein atomares/molekulares Verständnis von Adsorptions-, Desorptions- und Reaktionsprozessen inklusive deren Kinetik ermöglichen, wenn *in situ*-Methoden wie synchrotronbasiertes, schnelles HR-XPS eingesetzt werden. Die Untersuchung zeigt zudem die Bedeutung von Stufen/Kanten und Defekten für die Katalyse. Dabei sind derartige Nanoclusteranordnungen ein weiterer Schritt in die Materiallücke zwischen Modellkatalyse und echten Katalysatoren.

8   Literature

[1]   C. M. Friend, B. Xu, Heterogeneous Catalysis: A Central Science for a Sustainable Future, *Acc. Chem. Res.* **2017**, *50*, 517–521.

[2]   ExxonMobile, *2018 Outlook for Energy: A View to 2040*, **2018**.

[3]   J. W. Erisman, M. A. Sutton, J. Galloway, Z. Klimont, W. Winiwarter, How a century of ammonia synthesis changed the world, *Nat. Geosci.* **2008**, *1*, 636–639.

[4]   P. Forzatti, L. Lietti, Catalyst deactivation, *Catal. Today* **1999**, *52*, 165–181.

[5]   J. A. Moulijn, A. E. Van Diepen, F. Kapteijn, Catalyst deactivation: Is it predictable? What to do?, *Appl. Catal. A Gen.* **2001**, *212*, 3–16.

[6]   C. H. Bartholomew, Mechanisms of catalyst deactivation, *Appl. Catal. A Gen.* **2001**, *212*, 17–60.

[7]   C. N. Satterfield, in *Heterog. Catal. Ind. Pract.*, McGraw Hill Book Co., New York, **1991**.

[8]   J. C. Rodríguez, J. Santamaría, A. Monzón, Hydrogenation of 1,3-butadiene on Pd/SiO2 in the presence of H2S deactivation and reactivation of the catalyst, *Appl. Catal. A Gen.* **1997**, *165*, 147–157.

[9]   P. Albers, J. Pietsch, S. F. Parker, Poisoning and deactivation of palladium catalysts, *J. Mol. Catal. A Chem.* **2001**, *173*, 275–286.

[10]   J. Oudar, Sulfur adsorption and poisoning of metallic catalysts, *Catal. Rev. - Sci. Eng.* **1980**, *22*, 171–195.

[11]   T.-C. Yu, H. Shaw, The effect of sulfur poisoning on methane oxidation over palladium supported on γ-alumina catalysts, *Appl. Catal. B Environ.* **1998**, *18*, 105–114.

[12]   V. Meeyoo, J. H. Lee, D. L. Trimm, N. W. Cant, Hydrogen sulphide emission control by combined adsorption and catalytic combustion, *Catal. Today* **1998**, *44*, 67–72.

[13]   J. K. Lampert, M. S. Kazi, R. J. Farrauto, Palladium catalyst performance for methane emissions abatement from lean burn natural gas vehicles, *Appl. Catal. B Environ.* **1997**, *14*, 211–223.

[14]   J. R. Grace, H. Bi, in *Circ. Fluid. Beds*, Springer Netherlands, Dordrecht, **1997**, pp. 1–20.

[15]   W. Ostwald, Über die vermeintliche Isomerie des roten und gelben Quecksilberoxyds und die Oberflächenspannung fester Körper, *Zeitschrift für Phys. Chemie* **1900**, *34U*, 495–503.

[16]   M. v. Smoluchowski, Versuch einer mathematischen Theorie der Koagulationskinetik kolloider Lösungen, *Zeitschrift für Phys. Chemie* **1918**, *92U*, 129–168.

[17]   E. N. Voloshina, Y. S. Dedkov, S. Torbruegge, A. Thissen, M. Fonin, Graphene on Rh(111): STM and AFM studies, *Appl. Phys. Lett.* **2012**, *100*, 241606.

[18]   S. Krick Calderón, M. Grabau, L. Óvári, B. Kress, H.-P. Steinrück, C. Papp, CO oxidation on Pt(111) at near ambient pressures, *J. Chem. Phys.* **2016**, *144*, 044706.

[19]   R. Streber, C. Papp, M. P. A. Lorenz, A. Bayer, R. Denecke, H.-P. Steinrück, Sulfur Oxidation on Pt(355): It Is the Steps!, *Angew. Chemie Int. Ed.* **2009**, *48*, 9743–9746.

[20]   A. T. N'Diaye, T. Gerber, C. Busse, J. Myslivecek, J. Coraux, T. Michely, A versatile fabrication method for cluster superlattices, *New J. Phys.* **2009**, *11*, 103045.

[21]   K. Gotterbarm, C. Steiner, C. Bronnbauer, U. Bauer, H.-P. Steinrück, S. Maier, C. Papp, Graphene-Templated Growth of Pd Nanoclusters, *J. Phys. Chem. C* **2014**, *118*, 15934–15939.

[22]   K. Gotterbarm, C. Bronnbauer, U. Bauer, C. Papp, H.-P. Steinrück, Graphene-Supported Pd Nanoclusters Probed by Carbon Monoxide Adsorption, *J. Phys. Chem. C* **2014**, *118*, 25097–25103.

[23]   K. Gotterbarm, F. Späth, U. Bauer, C. Bronnbauer, H.-P. Steinrück, C. Papp, Reactivity of Graphene-Supported Pt Nanocluster Arrays, *ACS Catal.* **2015**, *5*, 2397–2403.

[24]   K. Gotterbarm, F. Späth, U. Bauer, H.-P. Steinrück, C. Papp, Adsorption and Reaction of SO2 on Graphene-Supported Pt Nanoclusters, *Top. Catal.* **2015**, *58*, 573–579.

[25]   A. J. Martínez-Galera, U. A. Schröder, C. Herbig, M. A. Arman, J. Knudsen, T. Michely, Preventing sintering of nanoclusters on graphene by radical adsorption, *Nanoscale* **2017**, *9*, 13618–13629.

[26]   A. K. Geim, I. V. Grigorieva, Van der Waals heterostructures, *Nature* **2013**, *499*, 419–425.

[27]   K. S. Novoselov, A. Mishchenko, A. Carvalho, A. H. Castro Neto, 2D materials and van der Waals heterostructures, *Science* **2016**, *353*, aac9439.

[28]   Y. Yao, Q. Fu, Y. Y. Zhang, X. Weng, H. Li, M. Chen, L. Jin, A. Dong, R. Mu, P. Jiang, et al., Graphene cover-promoted metal-catalyzed reactions, *Proc. Natl. Acad. Sci.* **2014**, *111*, 17023–17028.

[29]   D. Iwanenko, I. Pomeranchuk, On the maximal energy attainable in a betatron, *Phys. Rev.* **1944**, *65*, 343.

[30]   U. Englisch, "P04 Undulator Parameters," can be found under http://photon-science.desy.de/sites/site_photonscience/content/e58/e176720/e177229/e177918/e177943/e177944/P04_Apple2_Undulator_eng.jpg, **n.d.**

[31]   H. Hertz, Ueber einen Einfluss des ultravioletten Lichtes auf die electrische Entladung, *Ann. der Phys. und Chemie* **1887**, *267*, 983–1000.

[32]   A. Einstein, Über einen die Erzeugung und Verwandlung des Lichtes betreffenden heuristischen Gesichtspunkt, *Ann. Phys.* **1905**, *322*, 132–148.

[33]   P. A. M. Dirac, The Quantum Theory of the Emission and Absorption of Radiation, *Proc. R. Soc. A Math. Phys. Eng. Sci.* **1927**, *114*, 243–265.

[34]   C. S. Fadley, Angle-resolved x-ray photoelectron spectroscopy, *Prog. Surf. Sci.* **1984**, *16*, 275–388.

[35]   M. P. Seah, W. A. Dench, Quantitative Electron Spectroscopy of Surfaces: A Standard Data Base for Electron Inelastic Mean Free Paths in Solids, *Surf. Interface Anal.* **1979**, *1*, 2–11.

[36]   M. Kinne, Kinetische Untersuchungen von Oberflächenreaktionen Mittels Hochaufgelöster Röntgen-Photoelectronenspektroskopie - Oxidation von CO Auf Pt(111) Und Zugehörige Elementarschritte, Friedrich-Alexander-Universität Erlangen-Nürnberg, **2004**.

[37]   S. Doniach, M. Sunjic, Many-electron singularity in X-ray photoemission and X-ray line spectra from metals, *J. Phys. C Solid State Phys.* **2001**, *3*, 285–291.

[38]   W. Heisenberg, Über den anschaulichen Inhalt der quantentheoretischen Kinematik und Mechanik, *Zeitschrift für Phys.* **1927**, *43*, 172–198.

[39]   D. A. Shirley, High-Resolution X-Ray Photoemission Spectrum of the Valence Bands of Gold, *Phys. Rev. B* **1972**, *5*, 4709–4714.

[40]   S. Tougaard, Quantitative analysis of the inelastic background in surface electron spectroscopy, *Surf. Interface Anal.* **1988**, *11*, 453–472.

[41]   P. A. Thiel, E. D. Williams, J. T. Yates, W. H. Weinberg, The chemisorption of CO on Rh(111), *Surf. Sci.* **1979**, *84*, 54–64.

[42]   F. Maca, M. Scheffler, W. Berndt, The adsorption of sulphur on Pd(111) I. A LEED analysis of the adsorbate structure, *Surf. Sci.* **1985**, *160*, 467–474.

[43]   R. J. Koestner, M. Salmeron, E. B. Kollin, J. L. Gland, Adsorption and surface reactions of H2S on clean and S-covered Pt(111), *Surf. Sci.* **1986**, *172*, 668–690.

[44]   T. Wideman, L. G. Sneddon, Convenient Procedures for the Laboratory Preparation of Borazine, *Inorg. Chem.* **1995**, *34*, 1002–1003.

[45]   M. T. Paffett, R. J. Simonson, P. Papin, R. T. Paine, Borazine adsorption and decomposition at Pt(111) and Ru(001) surfaces, *Surf. Sci.* **1990**, *232*, 286–296.

[46]   W. Zhao, J. Gebhardt, F. Späth, K. Gotterbarm, C. Gleichweit, H.-P. Steinrück, A. Görling, C. Papp, Reversible Hydrogenation of Graphene on Ni(111)-Synthesis of "Graphone," *Chem. - A Eur. J.* **2015**, *21*, 3347–3358.

[47]   F. Späth, J. Gebhardt, F. Düll, U. Bauer, P. Bachmann, C. Gleichweit, A. Görling, H.-P. Steinrück, C. Papp, Hydrogenation and hydrogen intercalation of hexagonal boron nitride on Ni(1 1 1): reactivity and electronic structure, *2D Mater.* **2017**, *4*, 035026.

[48]   A. Hirsch, J. M. Englert, F. Hauke, Wet Chemical Functionalization of Graphene, *Acc. Chem. Res.* **2013**, *46*, 87–96.

[49]   R. Laskowski, P. Blaha, Ab initio study of h-BN nanomeshes on Ru(001), Rh(111), and Pt(111), *Phys. Rev. B* **2010**, *81*, 075418.

[50]   L. Gao, J. R. Guest, N. P. Guisinger, Epitaxial Graphene on Cu(111), *Nano Lett.* **2010**, *10*, 3512–3516.

[51]   A. T. N'Diaye, S. Bleikamp, P. J. Feibelman, T. Michely, Two-Dimensional Ir Cluster Lattice on a Graphene Moiré on Ir(111), *Phys. Rev. Lett.* **2006**, *97*, 215501.

[52]   J. Wintterlin, M. L. Bocquet, Graphene on metal surfaces, *Surf. Sci.* **2009**, *603*, 1841–1852.

[53]   A. B. Preobrajenski, M. L. Ng, A. S. Vinogradov, N. Mårtensson, Controlling graphene corrugation on lattice-mismatched substrates, *Phys. Rev. B - Condens. Matter Mater. Phys.* **2008**, *78*, 2–5.

[54]   K. Gotterbarm, W. Zhao, O. Höfert, C. Gleichweit, C. Papp, H.-P. Steinrück, Growth and oxidation of graphene on Rh(111), *Phys. Chem. Chem. Phys.* **2013**, *15*, 19625–19631.

[55]   F. Orlando, P. Lacovig, L. Omiciuolo, N. G. Apostol, R. Larciprete, A. Baraldi, S. Lizzit, Epitaxial Growth of a Single-Domain Hexagonal Boron Nitride Monolayer, *ACS Nano* **2014**, *8*, 12063–12070.

[56]   F. H. Farwick Zum Hagen, D. M. Zimmermann, C. C. Silva, C. Schlueter, N. Atodiresei, W. Jolie, A. J. Martínez-Galera, D. Dombrowski, U. A. Schröder, M. Will, et al., Structure and Growth of Hexagonal Boron Nitride on Ir(111), *ACS Nano* **2016**, *10*, 11012–11026.

[57]   M. Corso, W. Auwärter, M. Muntwiler, A. Tamai, T. Greber, J. Osterwalder, Boron nitride nanomesh., *Science* **2004**, *303*, 217–20.

[58]   F. Orlando, R. Larciprete, P. Lacovig, I. Boscarato, A. Baraldi, S. Lizzit, Epitaxial growth of hexagonal boron nitride on Ir(111), *J. Phys. Chem. C* **2012**, *116*, 157–164.

[59]   A. B. Preobrajenski, A. S. Vinogradov, M. L. Ng, E. Ćavar, R. Westerström, A. Mikkelsen, E. Lundgren, N. Mårtensson, Influence of chemical interaction at the lattice-mismatched h-BN/Rh(111) and h-BN/Pt(111) interfaces on the overlayer morphology, *Phys. Rev. B* **2007**, *75*, 245412.

[60]   A. B. Preobrajenski, A. S. Vinogradov, N. Mårtensson, Monolayer of h-BN chemisorbed on Cu(111) and Ni(111): The role of the transition metal 3d states, *Surf. Sci.* **2005**, *582*, 21–30.

[61]   K. K. Kim, A. Hsu, X. Jia, S. M. Kim, Y. Shi, M. Hofmann, D. Nezich, J. F. Rodriguez-Nieva, M. Dresselhaus, T. Palacios, et al., Synthesis of monolayer hexagonal boron nitride on Cu foil using chemical vapor deposition, *Nano Lett.* **2012**, *12*, 161–166.

[62]   M. Schwarz, A. Riss, M. Garnica, J. Ducke, P. S. Deimel, D. A. Duncan, P. K. Thakur, T. L. Lee, A. P. Seitsonen, J. V. Barth, et al., Corrugation in the Weakly Interacting Hexagonal-BN/Cu(111) System: Structure Determination by Combining Noncontact Atomic Force Microscopy and X-ray Standing Waves, *ACS Nano* **2017**, *11*, 9151–9161.

[63]   C. R. Henry, 2D-Arrays of Nanoparticles as Model Catalysts, *Catal. Letters* **2015**, *145*, 731–749.

[64]   D. Franz, N. Blanc, J. Coraux, G. Renaud, S. Runte, T. Gerber, C. Busse, T. Michely, P. J. Feibelman, U. Hejral, et al., Atomic structure of Pt nanoclusters supported by

graphene/Ir(111) and reversible transformation under CO exposure, *Phys. Rev. B* **2016**, *93*, 1–8.

[65] M. Sicot, S. Bouvron, O. Zander, U. Rüdiger, Y. S. Dedkov, M. Fonin, Nucleation and growth of nickel nanoclusters on graphene Moiré on Rh(111), *Appl. Phys. Lett.* **2010**, *96*, 093115.

[66] D. Franz, S. Runte, C. Busse, S. Schumacher, T. Gerber, T. Michely, M. Mantilla, V. Kilic, J. Zegenhagen, A. Stierle, Atomic structure and crystalline order of graphene-supported Ir nanoparticle lattices, *Phys. Rev. Lett.* **2013**, *110*, 1–5.

[67] X. Liu, Y. Han, J. W. Evans, A. K. Engstfeld, R. J. Behm, M. C. Tringides, M. Hupalo, H. Q. Lin, L. Huang, K. M. Ho, et al., Growth morphology and properties of metals on graphene, *Prog. Surf. Sci.* **2015**, *90*, 397–443.

[68] W. C. McKee, M. C. Patterson, J. R. Frick, P. T. Sprunger, Y. Xu, Adsorption of transition metal adatoms on h-BN/Rh(111): Implications for nanocluster self-assembly, *Catal. Today* **2017**, *280*, 220–231.

[69] M. Will, N. Atodiresei, V. Caciuc, P. L. T. Valerius, C. Herbig, T. Michely, A Monolayer of Hexagonal Boron Nitride on Ir(111) as a Template for Cluster Superlattices, *ACS Nano* **2018**, *12*, 6871–6880.

[70] M. L. Ng, A. B. Preobrajenski, A. S. Vinogradov, N. Mårtensson, Formation and temperature evolution of Au nanoparticles supported on the h-BN nanomesh, *Surf. Sci.* **2008**, *602*, 1250–1255.

[71] T. Gerber, J. Knudsen, P. J. Feibelman, E. Grånäs, P. Stratmann, K. Schulte, J. N. Andersen, T. Michely, E. Graìšnäs, P. Stratmann, et al., CO-Induced Smoluchowski Ripening of Pt Cluster Arrays on the Graphene/Ir(111) Moiré, *ACS Nano* **2013**, *7*, 2020–2031.

[72] M. C. Patterson, B. F. Habenicht, R. L. Kurtz, L. Liu, Y. Xu, P. T. Sprunger, Formation and stability of dense arrays of Au nanoclusters on hexagonal boron nitride/Rh(111), *Phys. Rev. B - Condens. Matter Mater. Phys.* **2014**, *89*, 1–10.

[73] F. Düll, U. Bauer, F. Späth, P. Bachmann, J. Steinhauer, H.-P. Steinrück, C. Papp, Bimetallic Pd–Pt alloy nanocluster arrays on graphene/Rh(111): formation, stability, and dynamics, *Phys. Chem. Chem. Phys.* **2018**, *20*, 21294–21301.

[74] O. Bunk, M. Corso, D. Martoccia, R. Herger, P. R. Willmott, B. D. Patterson, J. Osterwalder, J. F. van der Veen, T. Greber, Surface X-ray diffraction study of boron-nitride nanomesh in air, *Surf. Sci.* **2007**, *601*, L7–L10.

[75] F. Düll, F. Späth, P. Bachmann, U. Bauer, H.-P. H.-P. Steinrück, C. Papp, Reactivity of CO on Sulfur-Passivated Graphene-Supported Palladium Nanocluster Arrays, *J. Phys. Chem. C* **2017**, *121*, 1734–1741.

[76] F. Düll, F. Späth, U. Bauer, P. Bachmann, J. Steinhauer, H.-P. H.-P. Steinrück, C. Papp, Reactivity of CO on Sulfur-Passivated Graphene-Supported Platinum Nanocluster Arrays, *J. Phys. Chem. C* **2018**, *122*, 16008–16015.

[77] F. Düll, V. Schwaab, F. Späth, U. Bauer, P. Bachmann, J. Steinhauer, H.-P. Steinrück, C. Papp, Sulfur oxidation on graphene-supported platinum nanocluster arrays, *Chem. Phys. Lett.* **2018**, *708*, 165–169.

[78] J. Y. Luo, D. Kisinger, A. Abedi, W. S. Epling, Sulfur release from a model Pt/Al2O3 diesel oxidation catalyst: Temperature-programmed and step-response techniques characterization, *Appl. Catal. A Gen.* **2010**, *383*, 182–191.

[79] S. Surnev, M. Sock, M. G. Ramsey, F. P. Netzer, M. Wiklund, M. Borg, J. N. Andersen, CO adsorption on Pd(111): a high-resolution core level photoemission and electron energy loss spectroscopy study, *Surf. Sci.* **2000**, *470*, 171–185.

[80] J. Andersen, M. Qvarford, R. Nyholm, S. Sorensen, C. Wigren, Surface core-level shifts as a probe of the local overlayer structure: CO on Pd(100), *Phys. Rev. Lett.* **1991**, *67*, 2822–2825.

[81] M. E. Grillo, C. Stampfl, W. Berndt, Low-energy electron-diffraction analysis of the ($\sqrt{7} \times \sqrt{7}$)R19.1°-S adsorbate structure on the Pd(111) surface, *Surf. Sci.* **1994**, *317*, 84–98.

[82] S. Speller, T. Rauch, J. Bömermann, P. Borrmann, W. Heiland, Surface structures of S on Pd(111), *Surf. Sci.* **1999**, *441*, 107–116.

[83] T. Yamada, Z. Runsheng, Y. Iwasawa, K. Tamaru, Adsorption-desorption kinetics of carbon monoxide on a palladium (100) single crystal surface modified with sulfur, *Surf. Sci.* **1988**, *205*, 82–99.

[84] R. Streber, C. Papp, M. P. A. Lorenz, A. Bayer, S. Wickert, M. Schöppke, R. Denecke, H.-P. Steinrück, Site blocking and CO/sulfur site exchange processes on stepped Pt surfaces, *J. Phys. Condens. Matter* **2009**, *21*, 134018.

[85] M. Kinne, T. Fuhrmann, C. M. Whelan, J. F. Zhu, J. Pantförder, M. Probst, G. Held, R. Denecke, H. P. Steinrück, Kinetic parameters of CO adsorbed on Pt(111) studied by in situ high resolution x-ray photoelectron spectroscopy, *J. Chem. Phys.* **2002**, *117*, 10852–10859.

[86] B. Tränkenschuh, N. Fritsche, T. Fuhrmann, C. Papp, J. F. Zhu, R. Denecke, H.-P. Steinrück, A site-selective in situ study of CO adsorption and desorption on Pt(355)., *J. Chem. Phys.* **2006**, *124*, 74712.

[87] R. Streber, C. Papp, M. P. A. Lorenz, A. Bayer, R. Denecke, H.-P. Steinrück, Kinetic passivation of steps with sulfur and CO/S site exchange processes on stepped Pt surfaces, *Chem. Phys. Lett.* **2008**, *452*, 94–98.

[88] M. Kiskinova, A. Szabó, J. T. Yates, CO adsorption on Pt(111) modified with sulfur, *J. Chem. Phys.* **1988**, *89*, 7599.

[89] B. J. McIntyre, M. Salmeron, G. A. Somorjai, An in situ STM determination of a kinetic pathway for the coadsorbate-induced compression of sulfur by CO on Pt(111), *Surf. Sci.* **1995**, *323*, 189–197.

[90] E. L. Garfunkel, M. H. Farias, G. A. Somorjai, The modification of benzene and carbon monoxide adsorption on platinum(111) by the coadsorption of potassium or sulfur, *J. Am.*

Chem. Soc. **1985**, *107*, 349–353.

[91] B. Tränkenschuh, C. Papp, T. Fuhrmann, R. Denecke, H. P. Steinrück, The dissimilar twins - a comparative, site-selective in situ study of CO adsorption and desorption on Pt(322) and Pt(355), *Surf. Sci.* **2007**, *601*, 1108–1117.

[92] H. Steininger, S. Lehwald, H. Ibach, Adsorption of oxygen on Pt(111), *Surf. Sci.* **1982**, *123*, 1–17.

[93] D. R. Monroe, R. P. Merrill, Adsorption of oxygen on Pt(111) and its reactivity to hydrogen and carbon monoxide, *J. Catal.* **1980**, *65*, 461–469.

[94] R. Streber, C. Papp, M. P. A. Lorenz, O. Höfert, E. Darlatt, A. Bayer, R. Denecke, H.-P. Steinrück, SO2 adsorption and thermal evolution on clean and oxygen precovered Pt(111), *Chem. Phys. Lett.* **2010**, *494*, 188–192.

[95] K. Wilson, C. Hardacre, C. J. Baddeley, J. Lüdecke, D. P. Woodruff, R. M. Lambert, A spectroscopic study of the chemistry and reactivity of SO2 on Pt{111}: reactions with O2, CO and C3H6, *Surf. Sci.* **1997**, *372*, 279–288.

[96] I. P. Beletskaya, A. V. Cheprakov, The Heck Reaction as a Sharpening Stone of Palladium Catalysis, *Chem. Rev.* **2000**, *100*, 3009–3066.

[97] A. Fürstner, Gold and platinum catalysis—a convenient tool for generating molecular complexity, *Chem. Soc. Rev.* **2009**, *38*, 3208.

[98] N. M. Marković, T. J. Schmidt, V. Stamenković, P. N. Ross, Oxygen Reduction Reaction on Pt and Pt Bimetallic Surfaces: A Selective Review, *Fuel Cells* **2001**, *1*, 105–116.

[99] J. Greeley, I. E. L. Stephens, A. S. Bondarenko, T. P. Johansson, H. A. Hansen, T. F. Jaramillo, J. Rossmeisl, I. Chorkendorff, J. K. Nørskov, Alloys of platinum and early transition metals as oxygen reduction electrocatalysts, *Nat. Chem.* **2009**, *1*, 552–556.

[100] N. Iwasa, N. Takezawa, New Supported Pd and Pt Alloy Catalysts for Steam Reforming and Dehydrogenation of Methanol, *Top. Catal.* **2003**, *22*, 215–224.

[101] N. V. Long, T. D. Hien, T. Asaka, M. Ohtaki, M. Nogami, Synthesis and characterization of Pt-Pd alloy and core-shell bimetallic nanoparticles for direct methanol fuel cells (DMFCs): Enhanced electrocatalytic properties of well-shaped core-shell morphologies and nanostructures, *Int. J. Hydrogen Energy* **2011**, *36*, 8478–8491.

[102] A. De Clercq, O. Margeat, G. Sitja, C. R. Henry, S. Giorgio, Core–shell Pd–Pt nanocubes for the CO oxidation, *J. Catal.* **2016**, *336*, 33–40.

[103] F. de Boer; R. Boom; W. Mattens; A. Miedema; A. Niessen, *Cohesion in Metals:Transition Metal Alloys*, North-Holland, **1989**.

[104] S. Xiong, W. Qi, B. Huang, M. Wang, Size-, shape- and composition-dependent alloying ability of bimetallic nanoparticles, *ChemPhysChem* **2011**, *12*, 1317–1324.

[105] K. Tang, T. Wang, W. Qi, Y. Li, Debye temperature for binary alloys and its relationship

with cohesive energy, *Phys. B Condens. Matter* **2018**, *531*, 95–101.

[106] L. Castaldi, K. Giannakopoulos, A. Travlos, D. Niarchos, Coevaporation of CoPt nanoparticles, *Appl. Phys. Lett.* **2004**, *85*, 2854–2856.

[107] L. Castaldi, K. Giannakopoulos, A. Travlos, N. Boukos, D. Niarchos, S. Boukari, E. Beaurepaire, Engineering of FePt nanoparticles by e-beam co-evaporation, *Nanotechnology* **2008**, *19*, 135702.

[108] J. S. McEwen, S. H. Payne, H. J. Kreuzer, M. Kinne, R. Denecke, H. P. Steinrück, Adsorption and desorption of CO on Pt(1 1 1): A comprehensive analysis, *Surf. Sci.* **2003**, *545*, 47–69.

[109] U. Bauer, F. Späth, F. Düll, P. Bachmann, J. Steinhauer, H.-P. Steinrück, C. Papp, Reactivity of CO and C2H4 on Bimetallic PtxAg1-x/Pt(111) Surface Alloys Investigated by High-Resolution X-ray Photoelectron Spectroscopy, *ChemPhysChem* **2018**, *19*, 1432–1440.

[110] Y. Fukamori, M. König, B. Yoon, B. Wang, F. Esch, U. Heiz, U. Landman, Fundamental Insight into the Substrate-Dependent Ripening of Monodisperse Clusters, *ChemCatChem* **2013**, *5*, 3330–3341.

[111] B. A. J. Lechner, F. Knoller, A. Bourgund, U. Heiz, F. Esch, A Microscopy Approach to Investigating the Energetics of Small Supported Metal Clusters, *J. Phys. Chem. C* **2018**, *122*, 22569–22576.

[112] F. D. Natterer, F. Patthey, H. Brune, Ring State for Single Transition Metal Atoms on Boron Nitride on Rh(111), *Phys. Rev. Lett.* **2012**, *109*, 066101.

[113] J. R. Rostrup-Nielsen, Industrial relevance of coking, *Catal. Today* **1997**, *37*, 225–232.

[114] J. Lu, B. Fu, M. C. Kung, G. Xiao, J. W. Elam, H. H. Kung, P. C. Stair, Coking- and Sintering-Resistant Palladium Catalysts Achieved Through Atomic Layer Deposition, *Science* **2012**, *335*, 1205–1208.

[115] E. HERACLEOUS, A. LEMONIDOU, Ni–Nb–O mixed oxides as highly active and selective catalysts for ethene production via ethane oxidative dehydrogenation. Part II: Mechanistic aspects and kinetic modeling, *J. Catal.* **2006**, *237*, 175–189.

[116] A. Qiao, V. N. Kalevaru, J. Radnik, A. Martin, Oxidative dehydrogenation of ethane to ethylene over Ni–Nb–M–O catalysts: Effect of promoter metal and CO2 -admixture on the performance, *Catal. Today* **2016**, *264*, 144–151.

[117] J. Heveling, C. P. Nicolaides, M. S. Scurrell, Catalysts and conditions for the highly efficient, selective and stable heterogeneous oligomerisation of ethylene, *Appl. Catal. A Gen.* **1998**, *173*, 1–9.

[118] D. L. Trimm, Catalysts for the control of coking during steam reforming, *Catal. Today* **1999**, *49*, 3–10.

[119] S. Gomez Sanz, L. McMillan, J. McGregor, J. A. Zeitler, N. Al-Yassir, S. Al-Khattaf, L. F. Gladden, The enhancement of the catalytic performance of CrOx/Al2O3 catalysts for ethylbenzene dehydrogenation through tailored coke deposition, *Catal. Sci. Technol.* **2016**,

6, 1120–1133.

[120] A. Cassuto, J. Kiss, J. M. White, On the orientation of low temperature π-bonded ethylene on Pt(111), *Surf. Sci.* **1991**, *255*, 289–294.

[121] J. Kua, W. A. Goddard, Chemisorption of Organics on Platinum. 2. Chemisorption of C 2 H x and CH x on Pt(111) , *J. Phys. Chem. B* **2002**, *102*, 9492–9500.

[122] Y. Y. Yeo, A. Stuck, C. E. Wartnaby, R. Kose, D. A. King, Microcalorimetric study of ethylene adsorption at 300 K on Pt{100}-hex and Pt{100}-(1×1), *J. Mol. Catal. A Chem.* **1998**, *131*, 31–38.

[123] W. A. Brown, R. Kose, D. A. King, Calorimetric measurements of the adsorption heat for ethene on Pt{211} and Pt{311}, *Surf. Sci.* **1999**, *440*, 271–278.

[124] H.-P. Steinrück, T. Fuhrmann, C. Papp, B. Tränkenschuh, R. Denecke, A detailed analysis of vibrational excitations in x-ray photoelectron spectra of adsorbed small hydrocarbons, *J. Chem. Phys.* **2006**, *125*, 204706.

[125] N. Freyer, G. Pirug, H. P. Bonzel, Absolute coverage of C2H2 and C2H4 on Pt(111), *Surf. Sci.* **1983**, *125*, 327–334.

[126] G. H. Hatzikos, R. I. Masel, Structure sensitivity of ethylene adsorption on Pt(100): Evidence for vinylidene formation on (1×1) Pt(100), *Surf. Sci.* **1987**, *185*, 479–494.

[127] Y. Chen, D. G. Vlachos, Hydrogenation of Ethylene and Dehydrogenation and Hydrogenolysis of Ethane on Pt(111) and Pt(211): A Density Functional Theory Study, **2010**, 4973–4982.

[128] A. Narita, X.-Y. Wang, X. Feng, K. Müllen, New advances in nanographene chemistry, *Chem. Soc. Rev.* **2015**, *44*, 6616–6643.

[129] T. Enoki, K. Takai, V. Osipov, M. Baidakova, A. Vul', Nanographene and Nanodiamond; New Members in the Nanocarbon Family, *Chem. - An Asian J.* **2009**, *4*, 796–804.

[130] S. Rajasekaran, S. Kaya, T. Anniyev, H. Ogasawara, A. Nilsson, Probing substrate effects in the carbon-projected band structure of graphene on Pt(111) through resonant inelastic x-ray scattering, *Phys. Rev. B* **2012**, *85*, 045419.

[131] L. Camilli, J. H. Jørgensen, J. Tersoff, A. C. Stoot, R. Balog, A. Cassidy, J. T. Sadowski, P. Bøggild, L. Hornekær, Self-assembly of ordered graphene nanodot arrays, *Nat. Commun.* **2017**, *8*, 47.

[132] P. A. Brühwiler, A. J. Maxwell, C. Puglia, A. Nilsson, S. Andersson, N. Mårtensson, π* and σ* Excitons in C 1s Absorption of Graphite, *Phys. Rev. Lett.* **1995**, *74*, 614–617.

[133] G. Ertl, M. Neumann, K. M. Streit, Chemisorption of CO on the Pt(111) surface, *Surf. Sci.* **1977**, *64*, 393–410.

Appendix [P1] – [P7]

[P1] **Reactivity of CO on Sulfur-Passivated Graphene-Supported Palladium Nanocluster Arrays**

Fabian Düll, Florian Späth, Philipp Bachmann, Udo Bauer, Hans-Peter Steinrück, Christian Papp

The Journal of Physical Chemistry C **2017**, *121*, 1734–1741.

Author's contribution:

Measurement, analysis and interpretation of all shown data, authorship.

[P2] **Reactivity of CO on Sulfur-Passivated Graphene-Supported Platinum Nanocluster Arrays**

Fabian Düll, Florian Späth, Udo Bauer, Philipp Bachmann, Johann Steinhauer, Hans-Peter Steinrück, Christian Papp

The Journal of Physical Chemistry C **2018**, *122*, 16008-16015.

Author's contribution:

Measurement, analysis and interpretation of all shown data, authorship.

[P3] **Sulfur oxidation on graphene-supported platinum nanocluster arrays**

Fabian Düll, Valentin Schwaab, Florian Späth, Udo Bauer, Philipp Bachmann, Johann Steinhauer, Hans-Peter Steinrück, Christian Papp

Chemical Physics Letters **2018**, *708*, 165–169.

Author's contribution:

Measurement, analysis and interpretation of all shown data, authorship.

[P4] **Bimetallic Pd–Pt alloy nanocluster arrays on graphene/Rh(111): formation, stability, and dynamics**

Fabian Düll, Udo Bauer, Florian Späth, Philipp Bachmann, Johann Steinhauer, Hans-Peter Steinrück, Christian Papp

Physical Chemistry Chemical Physics **2018**, *20*, 21294–21301.

Author's contribution:

Measurement, analysis and interpretation of all shown data, authorship.

[P5]   **Growth and Stability of Pt nanoclusters from 1 to 50 atoms on *h*-BN/Rh(111)**
<u>Fabian Düll</u>, Manuel Meusel, Florian Späth, Simon Schötz, Udo Bauer, Philipp Bachmann, Johann Steinhauer, Hans-Peter Steinrück, Andreas Bayer, Christian Papp
Physical Chemistry Chemical Physics **2019**, *21*, 21287-21295.

Author's contribution:
Measurement, analysis and interpretation of XPS data, authorship.

[P6]   **Ethylene: Its adsorption, reaction, and coking on Pt/*h*-BN/Rh(111) nanocluster arrays**
<u>Fabian Düll</u>, Florian Späth, Udo Bauer, Philipp Bachmann, Johann Steinhauer, Hans-Peter Steinrück, Sandra Wickert, Reinhard Denecke, Christian Papp
to be submitted

Author's contribution:
Measurement of the data on nanoclusters, analysis and interpretation of all shown data, authorship.

[P7]   **Pt Nanoclusters Sandwiched between Hexagonal Boron Nitride and Nanographene as van der Waals Heterostructures for Optoelectronics**
<u>Fabian Düll</u>, Eva Marie Freiberger, Philipp Bachmann, Johann Steinhauer, Christian Papp
ACS Applied Nano Materials **2019**, *2*, 7019-7024.

Author's contribution:
Measurement, analysis and interpretation of all shown data, authorship.